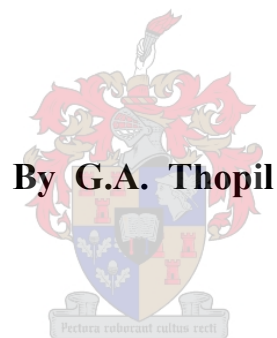# An Attitude and Orbit Determination and Control System for a small Geostationary Satellite

By G.A. Thopil

Thesis presented in partial fulfilment of the requirements for the degree of
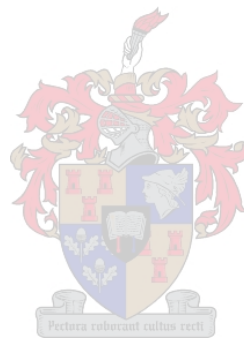Master of Science in Electronic Engineering at the University of Stellenbosch

December 2006

Supervisor: Prof. W.H. Steyn

Declaration:

I, the undersigned, hereby declare that the work contained in this thesis is my own original work and has not previously in its entirety or in part, been submitted at any university for a degree.

Signature:……………….   Date:……..…..

Abstract

An analysis of the attitude determination and control system required for a small geostationary satellite is performed in this thesis. A three axis quaternion feedback reaction wheel control system is the primary control system used to meet the stringent accuracy requirements. A momentum bias controller is also evaluated to provide redundancy and to extend actuator life.

Momentum dumping is preformed by magnetic torque rods using a cross-product controller. Performance of three axis thruster control is also evaluated. A full state Extended Kalman filter is used to determine attitude and body angular rates during normal operation whereas a Multiplicative Extended Kalman Filter is used during attitude manoeuvres.

An analytical orbit control study is also performed to calculate the propellant required to perform station-keeping, for a specific sub-satellite location over a ten year period. Finally an investigation on the effects caused by thruster misalignment, on satellite attitude is also performed.
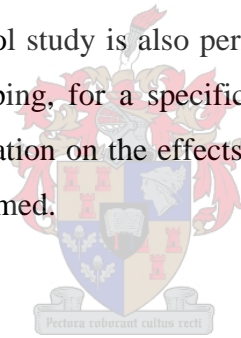
Opsomming

Die analise van 'n oriëntasie bepalings en beheerstelsel vir gebruik op 'n geostasionêre satelliet word in hierdie tesis behandel. 'n Drie-as "Quaternion" terugvoer reaksiewiel is die primêre behereerstelsel wat gebruik word om die vereiste hoë akkuraathede te verkry. 'n Momentum werkspunt beheerder word ook geëvalueer om oortolligheid te bewerkstellig en om die aktueerder leeftyd te verleng.

Momentum storting word deur magnetiese draaimomentstange uitgevoer met behulp van 'n kruisproduk beheerder. Werkverrigting van drie-as stuwer beheerder word ook geëvalueer. 'n Volle toestand uitgebreide Kalman filter word gebruik om die oriëntasie en liggaamhoektempos gedurende normale werking te bepaal, terwyl 'n vermenigvuldigende uitgebreide Kalman filter gedurende oriëntasiebewegings gebruik word.

'n Analitiese studie van wentelbaan beheer word ook uitgevoer om die hoeveelheid brandstof te bepaal wat oor 'n tien jaar periode benodig word om die satelliet se posisie ten opsigte van die aarde te handhaaf. Laastens word die invloed van stuwer wanbelyning op die satelliet se oriëntasie ook ondersoek.
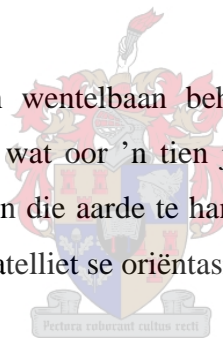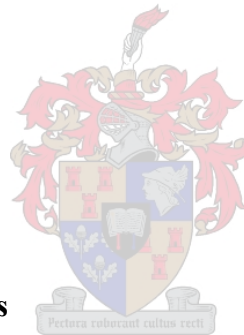
Acknowledgements

This thesis would be incomplete without mentioning the support and contributions of the following people and groups, to whom I would like to express my sincere gratitude:

Contents

Appendix E

Appendix F

List of Figures

List of Tables

List of Acronyms

AKM	Apogee Kick Motor
ADCS	Attitude Determination and Control System
AODCS	Attitude and Orbit Determination and Control System
BOL	Beginning Of Life
CMG	Control Moment Gyro
DCM	Direction Cosine Matrix
EKF	Extended Kalman Filter
ES	Earth Sensor
ESL	Electronic Systems Laboratory
EWSK	East West Station Keeping
FSS	Fine Sun Sensor
FOG	Fibre Optic Gyro
FOV	Field Of View
GEO	GEOstationary
GTO	Geostationary Transfer Orbit
HPT	High Power Thruster
IAGA	International Association of Geomagnetism and Aeronomy
IGRF	International Geomagnetic Reference Field
LEO	Low Earth Orbit
LPT	Low Power Thruster
MiDES-G	Mini Dual Earth Sensor-Geostationary
MEKF	Multiplicative Extended Kalman Filter
NORAD	NORth American aerospace Defense command
NSSK	North South Station Keeping
PD	Proportional Differential
PKM	Perigee Kick Motor
RAAN	Right Ascension of Ascending Node
RL	Root Locus
RPY	Roll Pitch Yaw
SDP4	Simplified Deep space Perturbations
STS	Space Transportation System
TLE	Two Line Element

List of Symbols

Mathematical Operators:

∇	Vector gradient
$\otimes$	Quaternion multiplication
Θ	Quaternion division

Satellite and orbital parameters:

ϕ, θ, ψ	Roll, pitch and yaw angle respectively
$\mathbf{q}$	Attitude quaternion vector in orbit coordinates
q_1, q_2, q_3, q_4	Quaternion vector components in orbit coordinates
$\mathbf{q_c}$	Commanded quaternion in orbit coordinates
$\mathbf{q_e}$	Error quaternion
$\mathbf{q_{vec}}$	Vector part of error quaternion
Φ	Euler rotation angle
e_x, e_y, e_z	Euler rotation axis components in orbit coordinates
$\boldsymbol{\omega}_B^I$	Body angular rate vector in inertial coordinates
ω_{ix}, ω_{iy}, ω_{iz}	Body angular rate vector components in inertial coordinates
$\boldsymbol{\omega}_B^O$	Body angular vector in orbit coordinates
ω_{ox}, ω_{oy}, ω_{oz}	Body angular rate vector components in orbit coordinates
ω_o	Mean orbit angular rate
ω_{nut}	Satellite nutation frequency
$\mathbf{h_{sat}}$	Angular momentum of satellite
LAT, LON	Latitude and longitude of satellite
SLAT, SLON	Latitude and longitude of sun
$\overline{\text{pos}}$	Unit position vector of satellite in inertial coordinates
$\overline{\text{vel}}$	Unit velocity vector of satellite in inertial coordinates
$\mathbf{Sat_{EARTH}^I}$	Position vector of satellite in inertial coordinates

Control and Disturbance Torques:

$\mathbf{T_T}$ Thruster torque vector

$\mathbf{T_M}$ Magnetic torque vector

T_{MX}, T_{MY}, T_{MZ} Magnetic torque vector components

$\mathbf{T_C}$ Control torque vector

T_{CX}, T_{CY}, T_{CZ} Control torque vector components

$\mathbf{T_{aero}}$ Aerodynamic disturbance torque vector

T_{aero} Scalar aerodynamic disturbance

$\mathbf{T_{gg}}$ Gravity gradient disturbance torque

T_{gg} Scalar gravity gradient disturbance

$\mathbf{T_{solar}}$ Solar radiation disturbance torque

T_{solar} Scalar solar radiation disturbance

$\mathbf{T_D}$ Total disturbance torque vector

T_{DX}, T_{DY}, T_{DZ} Total disturbance torque vector components in orbit coordinates

$\mathbf{T_{mis}}$ Thruster misalignment torque

$\mathbf{T_{comp}}$ Compensation torque
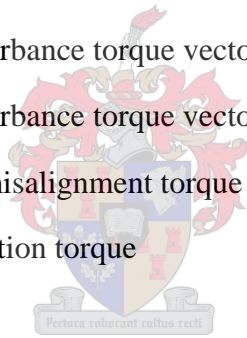
Inertia and transformation matrices:

$\mathbf{I}$ Identity matrix

$\mathbf{I_I}$ Moment of inertia tensor

I_{XX}, I_{YY}, I_{ZZ} Principle body axis inertia of satellite

$\mathbf{A}$ Attitude transformation matrix (DCM)

$\mathbf{D}$ Transformation matrix from body to FSS frame (coordinates)

$\mathbf{T}$ Transformation matrix from inertial to orbit coordiates

Reaction wheel parameters:

$\mathbf{h_w}$ Reaction wheel angular momentum vector

h_{wx}, h_{wy}, h_{wz} Reaction wheel angular momentum components

$\mathbf{h_{wN}}$ Desired wheel momentum vector

$\dot{\mathbf{h}}_w$, $\mathbf{T}_w$	Reaction wheel torque vector
$\dot{h}_{wx}$, $\dot{h}_{wy}$, $\dot{h}_{wz}$	Reaction wheel torque components
I_w	Inertia of wheel
ω_w	Angular rate of reaction wheel

IGRF and magnetic torque rod notations:

$\mathbf{B}_{VEC}^{I}$	Geomagnetic field vector in inertial coordinates
$\mathbf{B}_{VEC}^{O}$	Geomagnetic field vector in orbit coordinates
B_{ox} , B_{oy} , B_{oz}	Geomagnetic field vector components in orbit coordinates
$\mathbf{B}$, $\mathbf{B}_{VEC}^{B}$	Geomagnetic field vector in body coordinates
B_Z , B_Y , B_Z	Geomagnetic field vector components in body coordinates
$\mathbf{M}$	Magnetic moment vector
M_X , M_Y , M_Z	Magnetic moment vector components in body coordinates

Nadir vector and Earth sensor notations:

$\mathbf{E}_{VEC}^{I}$	Nadir vector in inertial coordinates
$\mathbf{E}_{VEC}^{O}$	Nadir vector in orbit coordinates
E_x^o , E_y^o , E_z^o	Components of nadir vector in orbit coordinates
$\mathbf{E}_{VEC}^{B}$	Nadir vector in body coordinates
E_x^b , E_y^b , E_z^b	Components of nadir vector in body coordinates
$\mathbf{E}_{VEC,k}^{B}$	Nadir vector in body coordinates at sample k
E_{xk}^b , E_{yk}^b , E_{zk}^b	Components of nadir vector in body coordinates at sample k
$\mathbf{E}_{VEC,k}^{O}$	Nadir vector in orbit coordinates at sample k
Roll, Pitch	Output angles of Earth sensor

Sun vector and Fine Sun Sensor notations:

| $\mathbf{S}_{EARTH}^{I}$ | Sun vector from earth in inertial coordinates |
| $\mathbf{S}_{SAT}^{I}$ | Sun vector from satellite in inertial coordinates |

$\mathbf{S_{VEC}^I}$	Unit sun vector from satellite in inertial coordinates
$\mathbf{S_{VEC}^O}$	Unit sun vector in orbit coordinates
$\mathbf{S_{VEC}^B}$	Unit sun vector in body coordinates
$S_x^b,\ S_y^b,\ S_z^b$	Components of unit sun vector in body coordinates
$\mathbf{S_{VEC}^S}$	Unit sun vector in sensor coordinates
$S_x^s,\ S_y^s,\ S_z^s$	Components of unit sun vector in sensor coordinates
$\mathbf{S_{VEC,}}_k^S$	Unit sun vector in sensor coordinates at sample k
$S_{xk}^s,\ S_{yk}^s,\ S_{zk}^s$	Component of unit sun vector in sensor coordinates at sample k
$\mathbf{S_{VEC,}}_k^B$	Unit sun vector in body coordinates at sample k
$\mathbf{S_{VEC,}}_k^O$	Unit sun vector in orbit coordinates at sample k
Azi, Ele	Output angles of Fine Sun Sensor

Fibre optic gyro parameters:

$\boldsymbol{\omega}_{fog}^I$	FOG angular rate vector in inertial coordinates
$\omega_{fogx,k},\ \omega_{fogy,k},\ \omega_{fogz,k}$	FOG angular rate components in inertial coordinates
$\mathbf{b}$	FOG bias vector
$\boldsymbol{\eta}_1$	FOG measurement noise vector
$\boldsymbol{\eta}_2$	FOG bias noise vector

Control system parameters:

t_s	Settling time
M_P	Peak overshoot
ζ	Damping factor
s_{CL}	Closed loop pole
ω_n	Natural frequency
ω_d	Damped frequency
K_P	Euler error control gain
K_D	Euler angular error control gain

$\mathbf{K_P}$	Quaternion error control gain matrix
$\mathbf{K_D}$	Angular rate control gain matrix
ϕ_{SS}	X axis steady state error
ψ_{SS}	Z axis steady state error

Thruster parameters:

F	Thrust level of LPT during attitude control
L	Torque arm
T	Torque output
τ	Time constant
K	Time constant network gain
V_{ON}	Trigger on level
V_{OFF}	Trigger off level
t_{ON}	Attitude control LPT on time
t_{OFF}	Attitude control LPT off time

Determination system parameters:

T_s	Sampling interval
$\mathbf{x}$	Continuous state vector
$\mathbf{x}_k$	Discrete state vector at sample k
$\hat{\mathbf{x}}_k$	Estimated state vector at sample k
$\boldsymbol{\delta}\mathbf{x}(t)$	Perturbation state vector at sample k
$\hat{\mathbf{q}}$	Estimated quaternion
$\boldsymbol{\delta}\mathbf{q}$	Perturbation quaternion vector
$\mathbf{A}(\hat{\mathbf{q}})$	Estimated DCM matrix
$\hat{\mathbf{b}}$	Estimated FOG bias vector
$\hat{b}_{x,k}$, $\hat{b}_{y,k}$, $\hat{b}_{z,k}$	Estimated FOG bias components
$\Delta\mathbf{b}$	Perturbation bias vector
$\mathbf{s}$	System noise vector
$\mathbf{m}$	Measurement noise vector

$\mathbf{f}\{\mathbf{x}(t),t\}$	Non-linear continuous system model
$\mathbf{F}\{\hat{\mathbf{x}}(t_k),t_k\}$	Linearised perturbation state matrix
$\mathbf{\Phi}_k$	Discrete system matrix at sample k
$\mathbf{y}_k$	Discrete output vector at sample k
$\mathbf{h}_k\{\mathbf{x}(t_k),t_k\}$	Non-linear discrete output model at sample k
$\mathbf{H}_k$	Linearised output matrix at sample k
$\mathbf{e}_k$	Linearised innovation model at sample k
$\mathbf{K}_k$	Kalman filter gain matrix at sample k
$\mathbf{P}_k$	Discrete state covariance matrix at sample k
$\mathbf{Q}$	System noise covariance matrix
$\mathbf{R}$	Measurement noise covariance matrix
$\mathbf{v}_{meas,k}$	Sensor measurement vector in body coordinates at sample k
$\mathbf{v}_{body,k}$	Modelled measurement vector in body coordinates at sample k
$\mathbf{v}_{orb,k}$	Modelled measurement vector in orbit coordinates at sample k
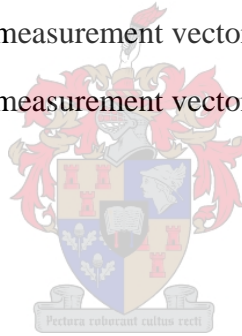
Chapter 1

Introduction

1.1 Concept

A *Geostationary* orbit (GEO) falls under the more general classification of *Geosynchronous* orbits. A *Geosynchronous* satellite is a satellite whose orbital track on the Earth repeats regularly over a point on the Earth over a sidereal day, the period at which the Earth rotates a full 360 degrees (approximately 23 hours 56 minutes 4 seconds). If such a satellite's orbit lies over the equator, it is called a GEO satellite. The inclination and eccentricity of a GEO satellite is close to zero.

A more detailed description will be helpful in understanding the mechanism of *Geosynchronous* satellite orbits. According to Kepler's Third law, the orbital period of a satellite in a circular orbit increases with increasing altitude. Space stations and remote sensing satellites in a low Earth orbit (LEO), typically of 400 to 650 km above the Earth's surface, completes between 15 to 16 revolutions per day. The Moon in comparison takes 28 days to complete one revolution. Between these two extremes lies an altitude of 35786 km at which the satellite's orbital period matches the period at which the Earth rotates. This is what is called a *Geosynchronous* satellite orbit.

If a *Geosynchronous* satellite's orbit is not aligned with the equator, which means that the orbit is inclined, it will appear to oscillate daily around a fixed point in the sky. This oscillation will have the shape of a figure of eight and the size of the figure will be determined by the inclination value. As the angle between the orbit and the equator decreases, the magnitude of this oscillation decreases. When the orbit lies entirely over the equator, the satellite remains stationary, relative to the Earth's surface and hence gets called *geostationary*.

(A) Location - 70E   , Inclination - 10 degrees; geosynchronous
(B) Location - 120W, Inclination - 30 degrees; geosynchronous
(C) Location - 0E   , Inclination - 0 degrees; geostationary
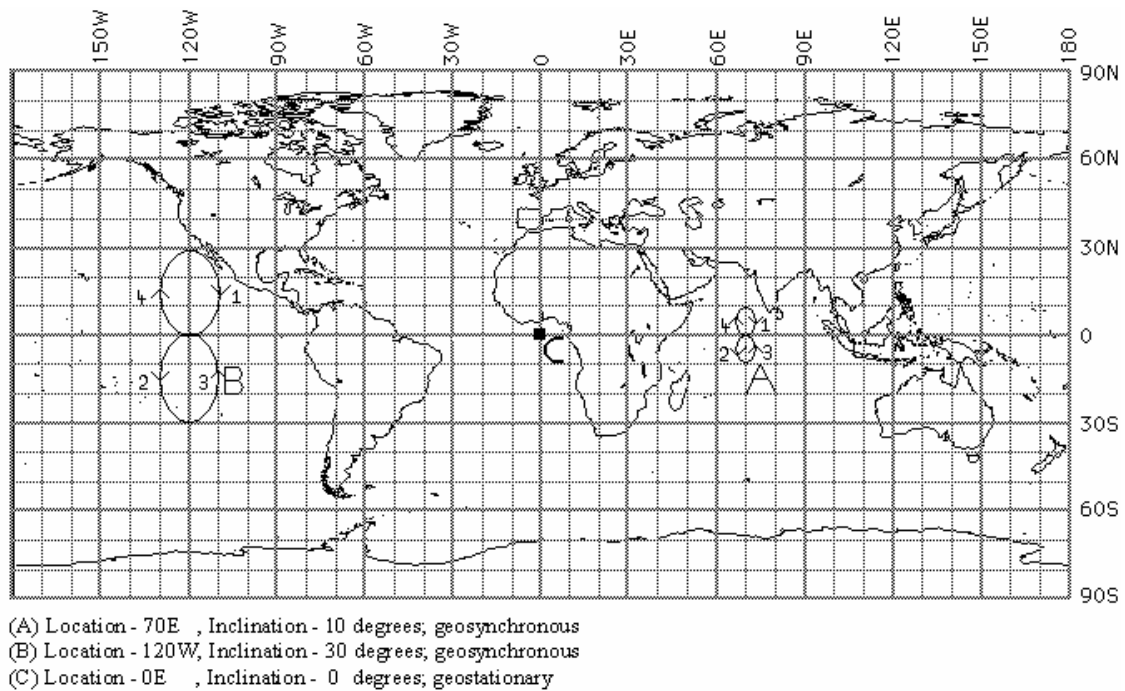
Figure 1.1 Ground tracks of Geosynchronous Satellites with Different Inclinations

Figure 1.1 shows that the larger the inclination of a *geosynchronous* satellite the bigger the oscillation. Since satellite 'C' has a non-oscillatory ground track we can conclude that it is a *geostationary* satellite. Therefore all *geostationary* satellites are *geosynchronous* but not all *geosynchronous* satellites are *geostationary*.

This doesn't mean that a geostationary satellite always has zero inclination. Inclination tends to build up due to gravitational effects of the Sun and the Moon. Hence the aim would be to minimise the inclination as much as possible. A detailed discussion on why inclination builds up and how it is minimised can be found in Chapter 7.

The inclination is also dependent on the mission requirement. For example, weather satellites tend to have a non-zero inclination so that they can monitor larger areas over a day's period and also because the weather changes slowly, but communication satellites tend to have inclinations as small as possible, since continuous communication is required by all regions in the foot print at all times.

1.2 Application

Since GEO satellites appear to be fixed over one spot above the equator, receiving and transmitting antennae on the Earth do not have to track the satellite. These antennae can be fixed in place and are much cheaper to install than tracking antennae. The GEO satellites find their application in global communications, television broadcasting and weather forecasting, and have significant military and defense applications.

One disadvantage of GEO satellites is a result of their altitude. Radio signals take approximately 0.25 seconds to reach and return from a satellite, resulting in a small but significant signal delay, especially in live-audio interaction. This delay can be ignored in non-interactive systems such as television broadcasts. Another disadvantage is the loss of signal strength or the requirement for higher signal strength for regions above 60 degrees latitude in each hemisphere (south and north). For example, satellite dishes in the southern hemisphere would need to be pointed almost directly to the north, thereby causing the signals to pass through the largest amount of the atmosphere which will cause a significant amount of attenuation. This is not a major problem in the southern hemisphere as compared to the northern hemisphere as there isn't much land above 60 degree latitude in the southern hemisphere.

Furthermore, since geostationary satellites are always positioned above the equator, it is impossible to cover the north and the south poles. A GEO satellite coverage is limited to a 70 degree latitude in either hemisphere. The Molniya or Tundra satellites provide coverage for regions in the pole region.

1.3 History

The idea of geosynchronous orbits was first proposed by Sir Arthur Charles Clarke in 1945. He conceived this idea in a paper titled *"Extra-Terrestrial Relays - Can Rocket Stations give Worldwide Radio Coverage ?"*, published in *Wireless World* in October 1945.

The first geosynchronous satellite was *Syncom 2*, launched on a Delta rocket B booster from Cape Canaveral on 26 July, 1963. It was used a few months later for the world's first satellite relayed telephone call between U.S President John.F.Kennedy and Nigerian Prime minister Abubakar Tafawa Balewa.

The first GEO communication satellite was *Syncom 3*, launched on a Delta D launch vehicle on 19 August, 1964. This satellite was placed near the *International Date Line* (180 degree longitude) and was used to telecast the 1964 Summer Olympics in Tokyo to the United States. There are currently approximately 300 operational geosynchronous satellites.

Note: *Syncom* 1 was launched on February 14, 1963 with the Delta B launch vehicle from Cape Canaveral, but was lost on the way to geosynchronous orbit due to an electronics failure. Later telescopic observations verified that the satellite was in an orbit with a period of almost 24 hours at an inclination of 33°.

1.4 Launching and Positioning

A GEO satellite can be launched into a GEO orbit in two different ways. One option would be to have a *space shuttle* (STS) take the satellite into a near Earth orbit of approximately 200 km altitude. Once in this altitude the satellite is ejected from the shuttle. In order to get the satellite into GTO (geostationary transfer orbit) a motor called the PKM (perigee kick motor) is fired. This firing will give the satellite enough velocity to place itself into a GTO. Once at the apogee of the GTO which has the same altitude as the GEO orbit, another motor called the AKM (apogee kick motor) is fired. This firing circularises the orbit of the satellite thereby achieving the final GEO orbit. The sequence of firing is shown in Figure 1.2.

The other option would be to have the satellite placed in an expendable launch vehicle. This vehicle after launch, ejects the satellite at an altitude of around 300km. The velocity of the launch vehicle is such that the satellite upon ejection from the vehicle finds itself in the GTO. Once at the apogee of the GTO the AKM is fired and the final GEO is attained.

The advantage of the second method is that the PKM firing is completely eliminated thereby reducing the amount of fuel the satellite has to carry. This is because of the fact that an attempt to change the velocity of the satellite near Earth will require a lot more fuel due to the higher influence of the geogravitational effects.
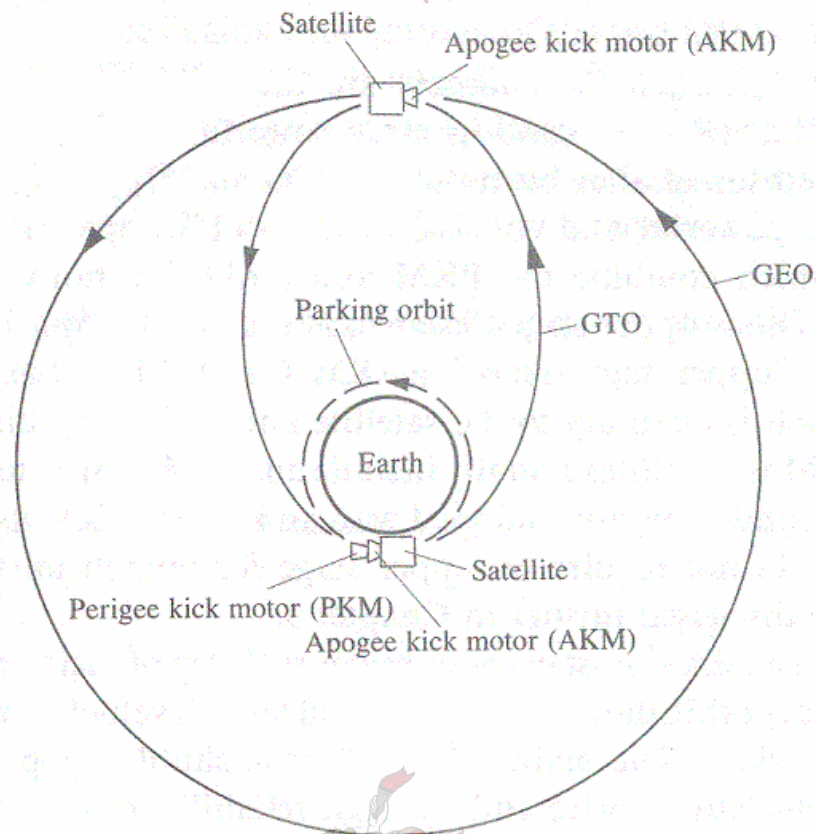
Figure 1.2 Orbital injection sequence using a *Space Transportation System*
(From Berlin, 1988, p. 17)

Figure 2.1 (in Chapter 2) shows the placement of the satellite directly into the GTO. It is important to mention that the 3rd stage burn in Figure 2.1 is performed by the launch vehicle and not the satellite. Examples of launch vehicles are *Ariane* 5 and *Delta* IV, to name a few.

1.5 Thesis Overview

The aim of this thesis is to perform a simulation study on the AODCS of a small GEO satellite in mission mode. A chapter by chapter introduction of the thesis is as follows:

Chapter 2 provides a detailed overview about the aim and background of this thesis. It also provides a simplified background on GEO satellites in general.

Chapter 3 will deal with the different types of models used in the simulation. A description of each model will be given, depending on the importance and complexity.

Chapter 4 looks at the actuators and sensors used for the AODCS in this specific case. Placement of sensors will also be evaluated. A brief general actuator analysis for GEO satellites will also be done.

Chapter 5 investigates various types of attitude control methods possible. Emphasis will be given on the different types of combinations (of actuators) possible with final accuracy in mind.

Chapter 6 covers the attitude estimation techniques performed. EKFs are used to estimate attitude, angular rates and angular rate bias. A thorough mathematical analysis will be performed.

Chapter 7 evaluates different orbit control techniques and calculations from a purely theoretical point of view. Also an analysis of the attitude control problem during orbit control manoeuvres is performed.

Chapter 8 provides a summary of the main chapters and recommendations on how the presented work can be advanced.
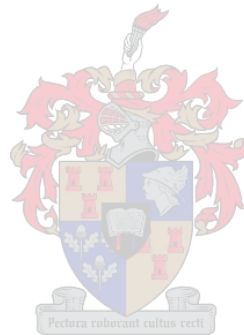
Chapter 2

Overview

2.1 Aim

The aim of this thesis as mentioned earlier is to perform a simulation study on the AODCS of a small GEO satellite, in mission mode. The error in attitude of the satellite in mission mode is expected be less than 0.1 degrees in mission mode. The satellite is assumed to have a mass of 500kg after launch and positioning. This is also called beginning of life (BOL) mass. To understand what mission mode really is, the following explanation will be helpful.

The control of a GEO satellite after separation from the launch vehicle can be divided into three modes. They are the following:

- *De-spin mode* – De-spinning the satellite after ejection from the launch vehicle so that the satellite can acquire references like the Sun, Earth or some other reference like a star.

- *Acquisition mode* – Acquiring the Sun (Sun acquisition) in order to deploy the solar panels. Earth acquisition so that the communication antenna can be deployed and also to provide the satellite with a reference about its orientation in space.

- *Mission mode* – Once the above mentioned steps have been performed the satellite is ready to be commissioned and be operational. The satellite stays in this mode so that uninterrupted communication is maintained during the entire mission period.
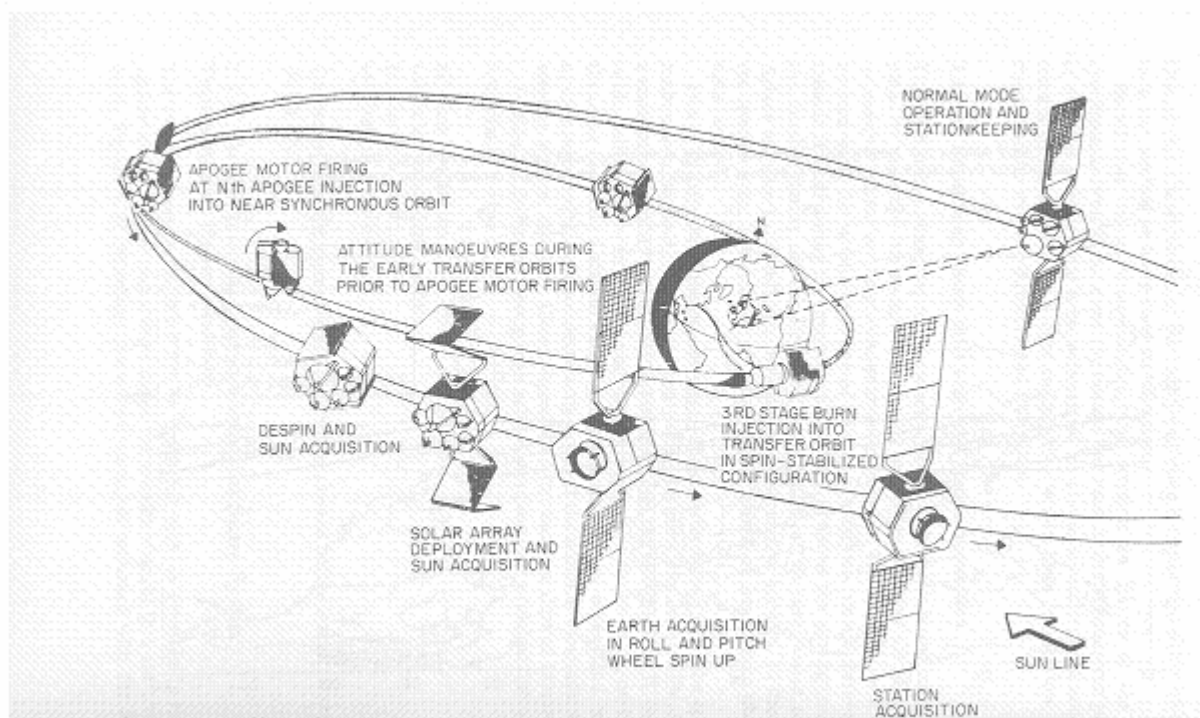
Figure 2.1 Satellite stages from launch vehicle separation to normal mission mode (From Maral and Basquet, 1986, p 310)

Figure 2.1 shows us the different modes of the satellite from ejection from the launch vehicle to the final operational phase. After the apogee motor is fired, the satellite enters geosynchronous orbit. The satellite will be tumbling at some rate and the satellite must be de-spun. The control mode used during this stage is called the *de-spin mode*. Next the acquisitions of the Sun and Earth are initiated and the solar panels are deployed. The satellite now has the ability to power itself. Also, the batteries get charged in order to deliver power during eclipse. The satellite is now oriented so as to give coverage over the intended geographical area. These processes constitute the *acquisition mode*. Minor orbit corrections are performed if necessary. Once these corrections are done the satellite is ready to perform normal operations. The satellite is now able to perform its mission and its mode of operation from this point onwards is called *mission mode*.

2.2 Attitude Coordinates

The attitude or orientation of the satellite is defined with respect to certain coordinates. Any object or body in flight needs to have a frame of reference so that one can uniquely define its attitude in a 3-dimensional coordinate system. For a body in space an additional frame of reference is required in order to define the orbit in space.

The main reference coordinates are namely, the *inertial coordinates*, the *orbit coordinates* and the *body coordinates*.

2.2.1 Inertial coordinates

The inertial coordinates used here are also called Geocentric Inertial Coordinates. It has its X_I-axis pointing towards the *vernal equinox*, the Z_I-axis pointing towards the Earth's geometric North Pole and the Y_I-axis completing the orthogonal set.
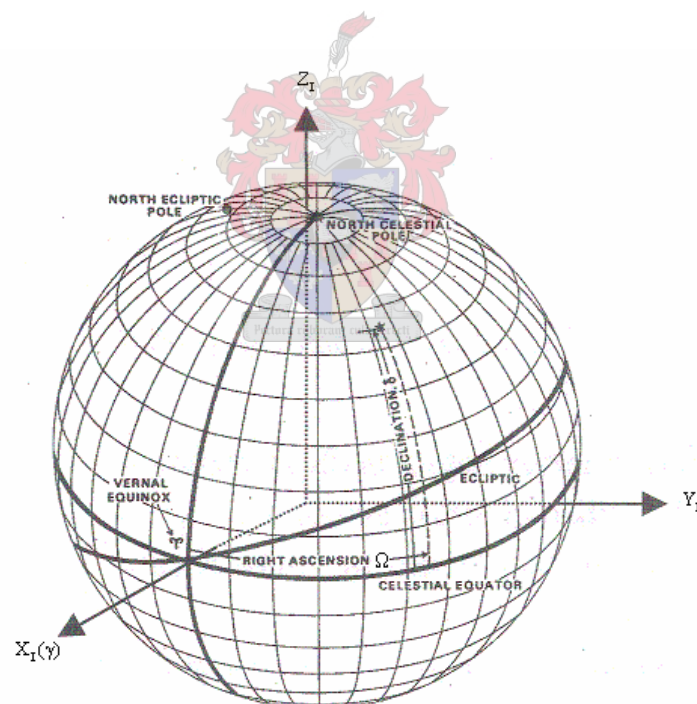
Figure 2.2 Inertial coordinates (Geocentric Inertial coordinates)

In Figure 2.2 we can see the vernal equinox is the point where the ecliptic (plane of the Earth's orbit around the Sun) crosses the equator from south to north.

2.2.2 Orbit coordinates

The orbit coordinates has its origin at the spacecraft's centre and maintains its position relative to the Earth as the spacecraft moves in orbit. The Z_O-axis is in the nadir direction, the Y_O-axis is in the orbit anti-normal direction and the X_O-axis completes the orthogonal set. The X_O-axis will be in the orbit velocity direction for a circular orbit (which is true for a GEO).
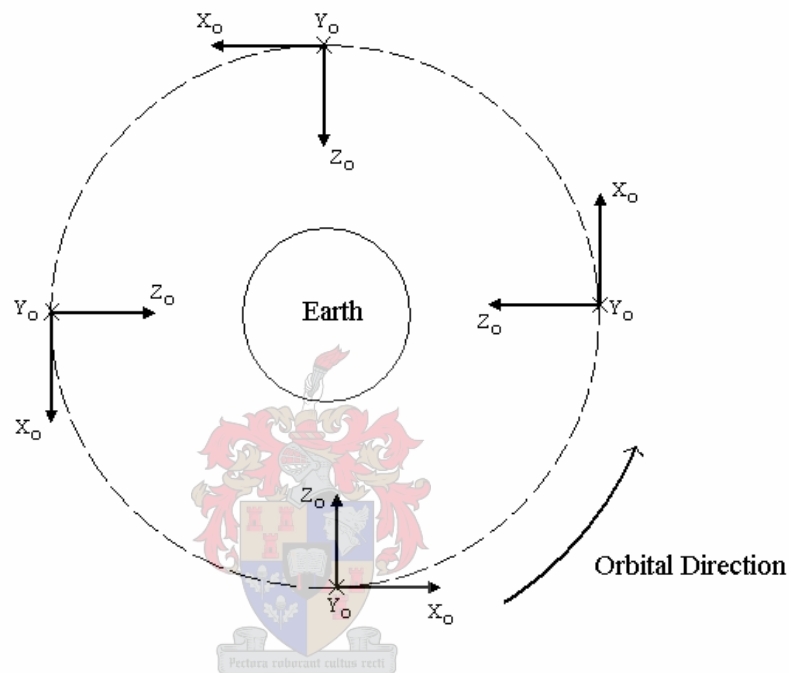
Figure 2.3 Orbit coordinates

The orbit coordinates helps in defining the orbit of the satellite with respect to Earth. It acts as a connecting link between the inertial coordinates and the body coordinates. The relation between the inertial coordinates and the orbit coordinates is shown in Figure 2.4. The $\overline{pos}$ and $\overline{vel}$ vectors are the position and velocity vectors of the satellite. In a case where a vector in the inertial coordinates has to be transformed to the orbit coordinates, a transformation matrix is used. This matrix is based on the position and velocity vectors. The transformation matrix is calculated in Section A.1 (Appendix A).
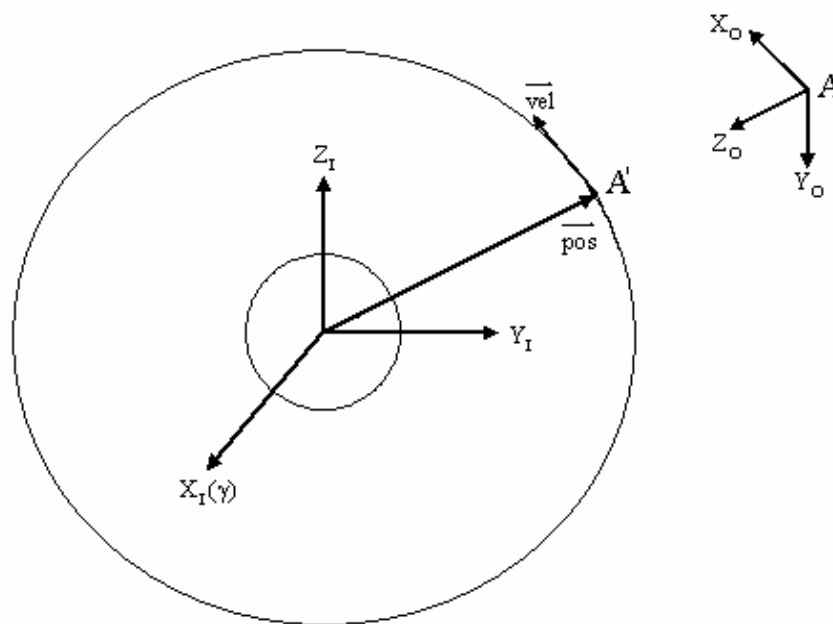
Figure 2.4   Inertial and Orbit coordinates

Note: Actually the origin of the orbit coordinates A will coincide with point A'. The above illustration is to avoid overlap of the X_O axis and Z_O axis with the $\overrightarrow{vel}$ and $\overrightarrow{pos}$ vectors respectively.
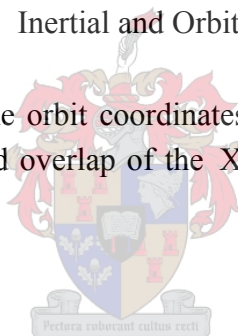
2.2.3 Body coordinates

The body coordinates are also called spacecraft fixed coordinates. This frame is used to define the orientation of the satellite body with respect to the reference frame. The mentioned coordinates has its origin at the centre of mass (CoM) of the satellite and is fixed with respect to the satellite, as the name suggests. The Z_B-axis is along the boresight of the communication antenna. The Y_B-axis is parallel to the solar panels and X_B-axis completes an orthogonal set. Figure 2.5 shows the body coordinates.

The relation between the orbit coordinates and the body coordinates is shown in Figure 2.6. The satellite in the nominal position will have its body frame aligned with the orbit frame. Figure 2.6 shows an offset of the satellite from the nominal position. A vector in the orbit coordinates is transformed to the body coordinates using the DCM. The DCM is an orthonormal matrix. Similarly a vector in the body coordinates can be transformed to the orbit coordinates using an inverse DCM.
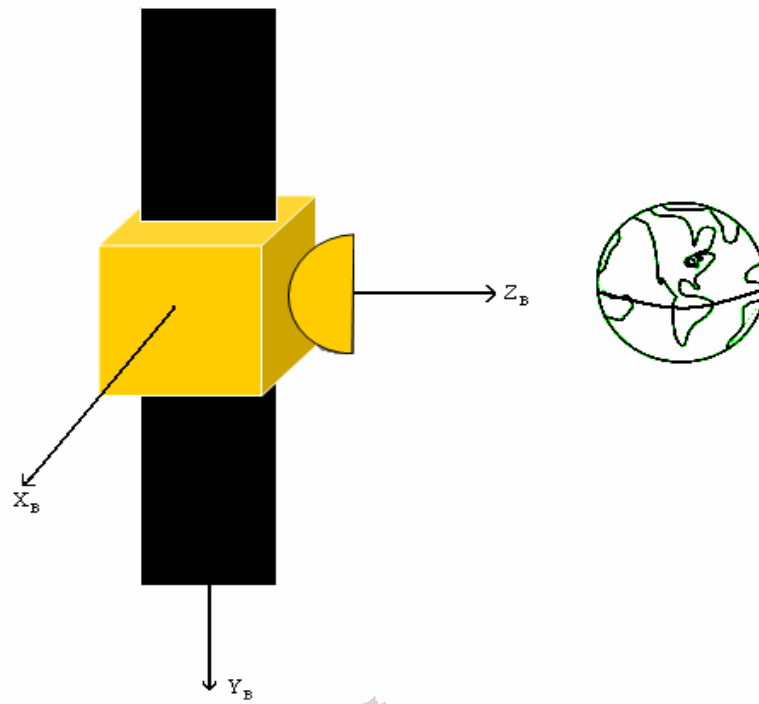
Figure 2.5 Body coordinates (normal position)
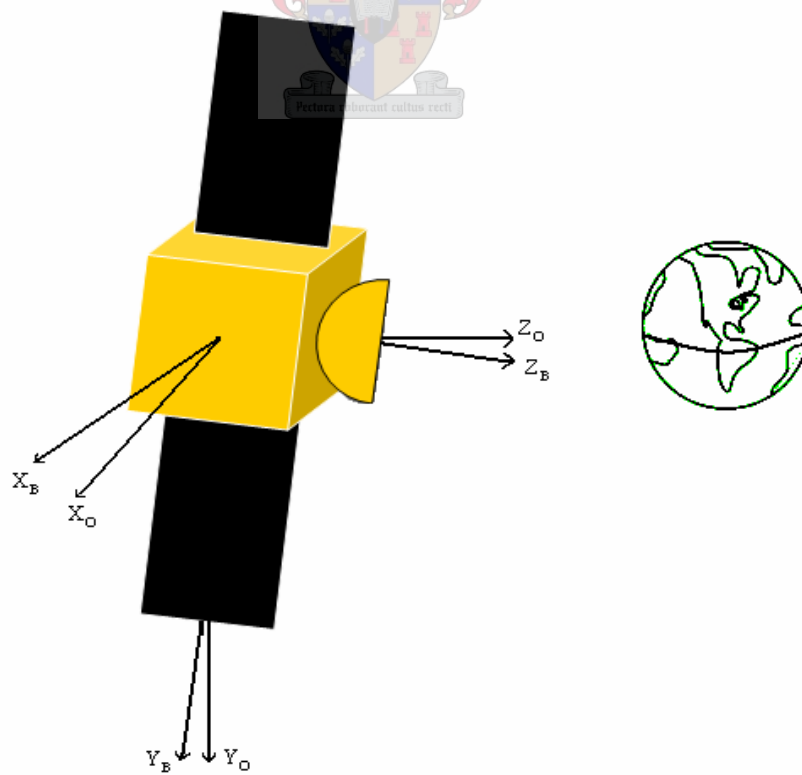
Figure 2.6 Orbit and Body coordinates

2.3 Attitude Definitions

The attitude of the satellite can be defined by Euler angles. An Euler angle rotation is defined as successive angular rotations about the three orthonormal frame axes. These angles are obtained from an ordered series of right hand rotations from the orbit coordinates ($X_O Y_O Z_O$) to the body coordinates ($X_B Y_B Z_B$).

An Euler 2-1-3 sequence of rotations is used in this thesis. The first manoeuvre is a rotation along the Pitch axis (defined by θ), followed by a Roll rotation (defined by ϕ) and finally a Yaw rotation (defined by ψ). Figure 2.7 shows the rotation sequence.
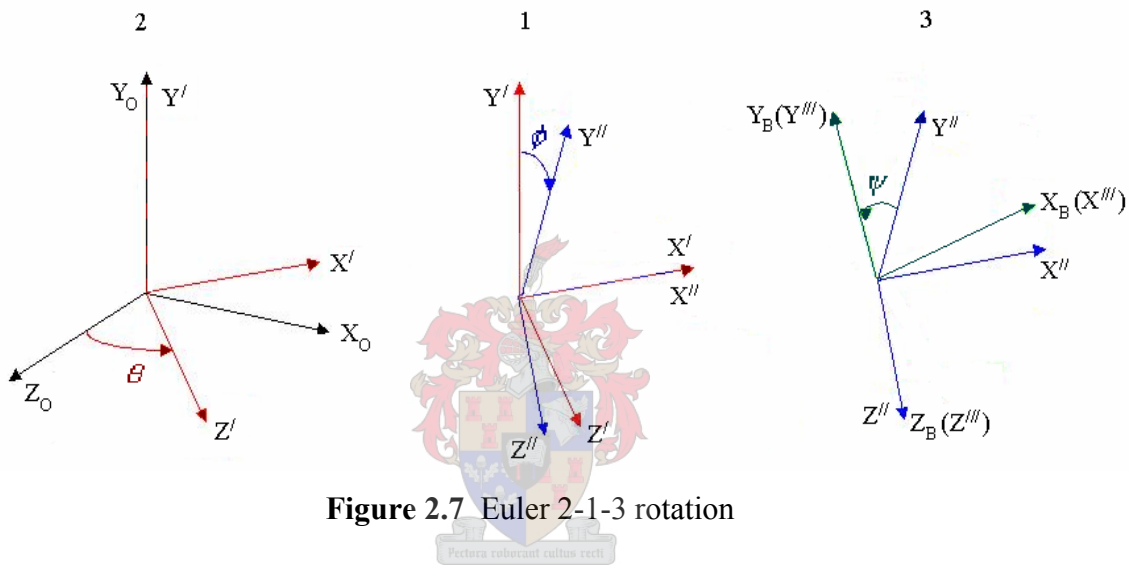
Figure 2.7 Euler 2-1-3 rotation

The attitude transformation matrix from the orbit coordinates to the body coordinates is given as,

$$[A_{213}] = [A_{\theta\phi\psi}] = \begin{bmatrix} c\psi\, c\theta + s\psi\, s\phi\, s\theta & s\psi\, c\phi & -c\psi\, s\theta + s\psi\, s\phi\, c\theta \\ -s\psi\, c\theta + c\psi\, s\phi\, s\theta & c\psi\, c\phi & s\psi\, s\theta + c\psi\, s\phi\, c\theta \\ c\phi\, s\theta & -s\phi & c\phi\, c\theta \end{bmatrix} \quad (2.1)$$

The Euler angle representation is the most easily understood attitude representation, because of its clear physical interpretation in angles. The drawback though is that it suffers from singularities. The problem of singularity in the above mentioned Euler representation is discussed in Appendix B. Another representation of attitude is using the Euler axis vector and the rotation angle of the Euler axis. This representation also encounters problems because of the presence of trigonometric functions which is also discussed in Appendix B. In order to overcome all these

issues we fortunately have a representation which makes use of the Euler symmetric parameters or *quaternions*. The main drawback of this representation is that it lacks physical interpretation. The quaternions are represented as,

$$q_1 = e_x \sin \frac{\Phi}{2}$$

$$q_2 = e_y \sin \frac{\Phi}{2}$$

$$q_3 = e_z \sin \frac{\Phi}{2}$$ \hfill (2.2)

$$q_4 = \cos \frac{\Phi}{2}$$

where,

$$e_x, e_y, e_z = \text{components of unit Euler axis vector in orbit coordinates}$$

$$\Phi = \text{rotation angle around Euler axis}$$

We can see that the quaternion elements will satisfy the constraint of,

$$q_1^2 + q_2^2 + q_3^2 + q_4^2 = 1 \hfill (2.3)$$

The attitude transformation matrix in Equation (2.1) can be rewritten in terms of the quaternions as;

$$[\mathbf{A(q)}] = \begin{bmatrix} q_1^2 - q_2^2 - q_3^2 + q_4^2 & 2(q_1 q_2 + q_3 q_4) & 2(q_1 q_3 - q_2 q_4) \\ 2(q_1 q_2 - q_3 q_4) & -q_1^2 + q_2^2 - q_3^2 + q_4^2 & 2(q_2 q_3 + q_1 q_4) \\ 2(q_1 q_3 + q_2 q_4) & 2(q_2 q_3 - q_1 q_4) & -q_1^2 - q_2^2 + q_3^2 + q_4^2 \end{bmatrix} \quad (2.4)$$

If the transformation matrix is in terms of the Euler angles then the quaternion elements can be calculated from a comparison of Equation (2.1) and Equation (2.4) as shown;

$$q_4 = 0.5[1 + a_{11} + a_{22} + a_{33}]^{0.5},$$

$$\hfill (2.5)$$

$$q_1 = \frac{0.25}{q_4}[a_{23} - a_{32}], \quad q_2 = \frac{0.25}{q_4}[a_{31} - a_{13}], \quad q_3 = \frac{0.25}{q_4}[a_{12} - a_{21}]$$

The quaternion element q_4 is called the pivot. Cases where q_4 is a very small number, numerical inaccuracies occur while calculating the remaining elements. Other possible combinations of calculating the quaternion elements are discussed in Appendix B.

It is also essential to extract the Euler angles from the transformation matrix to enable physical interpretation of the attitude. The Euler angles can be calculated from Equation (2.4) with the aid of Equation (2.1).

$$(\text{Roll})\phi = \operatorname{asin}(-a_{32}), \ (\text{Pitch})\theta = \operatorname{atan2}(a_{31}/a_{33}), \ (\text{Yaw})\psi = \operatorname{atan2}(a_{12}/a_{22}) \quad (2.6)$$

Note: The above representation is valid only for Euler 2-1-3 rotation and 'atan2' is a four quadrant function.

2.4 Equations of Motion

The equations of motion of a satellite is categorised into the dynamic and the kinematic equations of motion.

2.4.1 Euler Dynamic Equations of Motion

The dynamic equations of motion of a spacecraft find its origin from the Coriolis theorem. The equations give the relation between the internal torques and external torques acting on the spacecraft.

Coriolis theorem gives us the relation between the acceleration of a vector **C**, in an inertial coordinate system (*I*) and a frame (*R*) rotating with an angular velocity ω as,

$$\left(\frac{d\mathbf{C}}{dt}\right)_I = \left(\frac{d\mathbf{C}}{dt}\right)_R + \omega \times \mathbf{C} \quad (2.7)$$

The differential equations which describe the motion of a spacecraft are given as,

$$\mathbf{I_I}\dot{\boldsymbol{\omega}}_B^I = \mathbf{T}_M + \mathbf{T}_T + \mathbf{T}_D - \boldsymbol{\omega}_B^I \times (\mathbf{I}\boldsymbol{\omega}_B^I + \mathbf{h_w}) - \dot{\mathbf{h}}_w \quad (2.8)$$

A comparison of Equation (2.7) and Equation (2.8) shows that the vector in consideration is $\mathbf{C} = (\mathbf{I_I}\boldsymbol{\omega}_B^I + \mathbf{h_w})$, which is the total internal angular momentum of the spacecraft.

The terms involved in Equation (2.8) are as follows;

$$\mathbf{I_I} = \begin{bmatrix} I_{xx} & I_{xy} & I_{xz} \\ I_{yx} & I_{yy} & I_{yz} \\ I_{zx} & I_{zy} & I_{zz} \end{bmatrix} = \text{moment of inertia tensor in body coordinates}$$

$$\boldsymbol{\omega}_B^I = \begin{bmatrix} \omega_{ix} \\ \omega_{iy} \\ \omega_{iz} \end{bmatrix} \qquad = \text{body angular rate vector in inertial coordinates}$$

$$\mathbf{h_w} = \begin{bmatrix} h_{wx} \\ h_{wy} \\ h_{wz} \end{bmatrix} \qquad = \text{angular momentum of reaction wheels in body coordinates}$$

$\mathbf{T_M} \qquad\qquad = \text{magnetic torque vector in body coordinates}$

$\mathbf{T_T} \qquad\qquad = \text{thruster torque vector in body coordinates}$

$\mathbf{T_D} \qquad\qquad = \text{external disturbance torques in body coordinates}$

where,

$$\mathbf{T_D} = \mathbf{T_{aero}} + \mathbf{T_{gg}} + \mathbf{T_{solar}}$$

and,

$\mathbf{T_{aero}} \qquad\qquad = \text{aerodynamic disturbance torque}$

$\mathbf{T_{gg}} \qquad\qquad = \text{gravity gradient disturbance torque}$

$\mathbf{T_{solar}} \qquad\qquad = \text{solar radiation disturbance torque}$

2.4.2 Quaternion Kinematics

The kinematics equations describe the motion of a spacecraft irrespective of the forces which cause the motion. It is described by the relation between quaternions and their rates using the orbit referenced angular rates. The differential equation describing the kinematics is given as, (source of equation is discussed in Appendix B)

$$\dot{\mathbf{q}} = \frac{1}{2}\Omega\mathbf{q} \tag{2.9}$$

where,

$$\Omega = \begin{bmatrix} 0 & \omega_{oz} & -\omega_{oy} & \omega_{ox} \\ -\omega_{oz} & 0 & \omega_{ox} & \omega_{oy} \\ \omega_{oy} & -\omega_{ox} & 0 & \omega_{oz} \\ -\omega_{ox} & -\omega_{oy} & -\omega_{oz} & 0 \end{bmatrix} \tag{2.10}$$

and,

$$\boldsymbol{\omega}_B^O = \begin{bmatrix} \omega_{ox} \\ \omega_{oy} \\ \omega_{oz} \end{bmatrix} = \text{body angular rate vector in orbit coordinates}$$

The body angular rate vector in orbit coordinates are related to the angular rate vector in inertial coordinates by,

$$\boldsymbol{\omega}_B^O = \boldsymbol{\omega}_B^I - \mathbf{A} \begin{bmatrix} 0 \\ -\tilde{\omega}_o(t) \\ 0 \end{bmatrix} \qquad (2.11)$$

where,

$$\tilde{\omega}_o(t) \approx \omega_o \{1 + 2e \cos(\omega_o t + M_o)\} \text{ for small values of orbit eccentricity } e \qquad (2.12)$$

and,

$\tilde{\omega}_o(t)$ = true orbit angular rate

ω_o = orbit mean motion

M_o = orbit mean anomaly at epoch

2.5 Task overview

The AODCS requires a combination of different actuators and sensors. The block diagram of the entire system is shown below. As seen, the estimated parameters are used in the control algorithms and care must be taken to minimise the effects of sensor noise in the control torques. All disturbance torque models are discussed in Chapter 3 along with various reference vectors for the sensors. The different sensor models are discussed in Chapter 4.
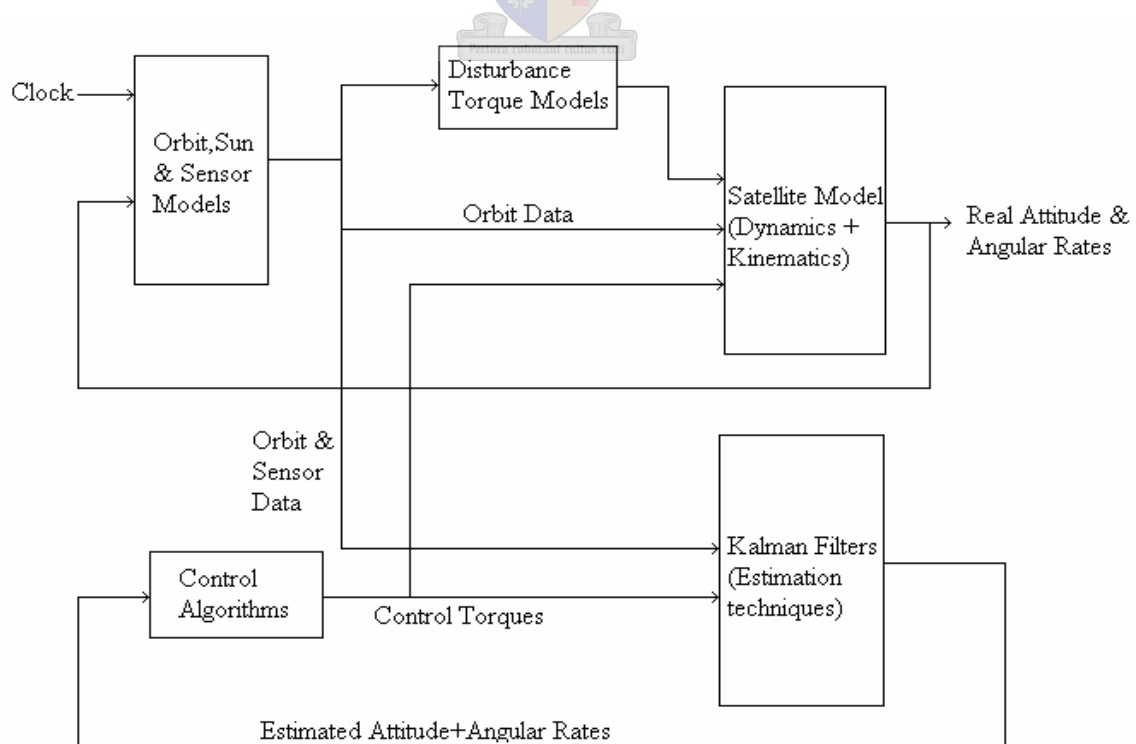
Figure 2.8 System Block Diagram

Different control algorithms have been evaluated and the performance of each algorithm has been evaluated in Chapter 5 and Chapter 7. Most control algorithms are feedback algorithms. The attitude and angular rates are fed-back to the controllers. It so happens that the attitude has to be estimated from sensor data. Angular rate measurements are available from fibre optic gyroscopes (FOG), but these are used very sparingly as they need to last the entire mission period. So, when FOGs are not used, the angular rates need to be estimated. Estimation techniques are discussed in Chapter 6. An analysis of the satellite dimension and the tools used in the study will be discussed in the following sub-sections.

2.5.1 Satellite model

The model of the satellite used in the study is shown in Figure 2.9. Dimensions of the satellite in all three axes are also shown. The main body dimensions are, 1 x 1.5 x 1.2 metre. The solar panels have dimensions of, 2 x 1 meter and the antenna a radius of 0.4 metre. The dimensions of the satellite are vital in modelling the solar radiation torque accurately. Solar radiation torque is calculated in Section 3.6.1. The mass of the satellite and the appendage orientation, determines the moment of inertias along each axis, which is one factor influencing the size of the actuators.
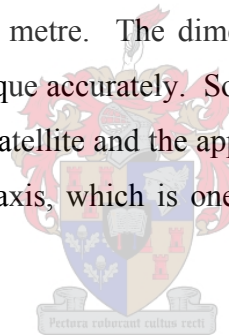
2.5.2 Fictional Hardware

Though no physical hardware is used in this thesis because of it being a simulation study, all sensors and actuators that might be used for the AODCS have been modelled in software. Sensors that have been modelled include a magnetometer, fine Sun sensor (FSS), Earth sensor (ES) and FOGs.

Reference vectors are modelled to provide a reference for the spacecraft. Reference models include an IGRF model (reference for magnetometer measurements), Sun vector model and Nadir vector model (reference for Sun and Earth sensor measurements). These reference models are discussed in Chapter 3. The vectors measured by the sensors are related to the respective reference vectors by the DCM.
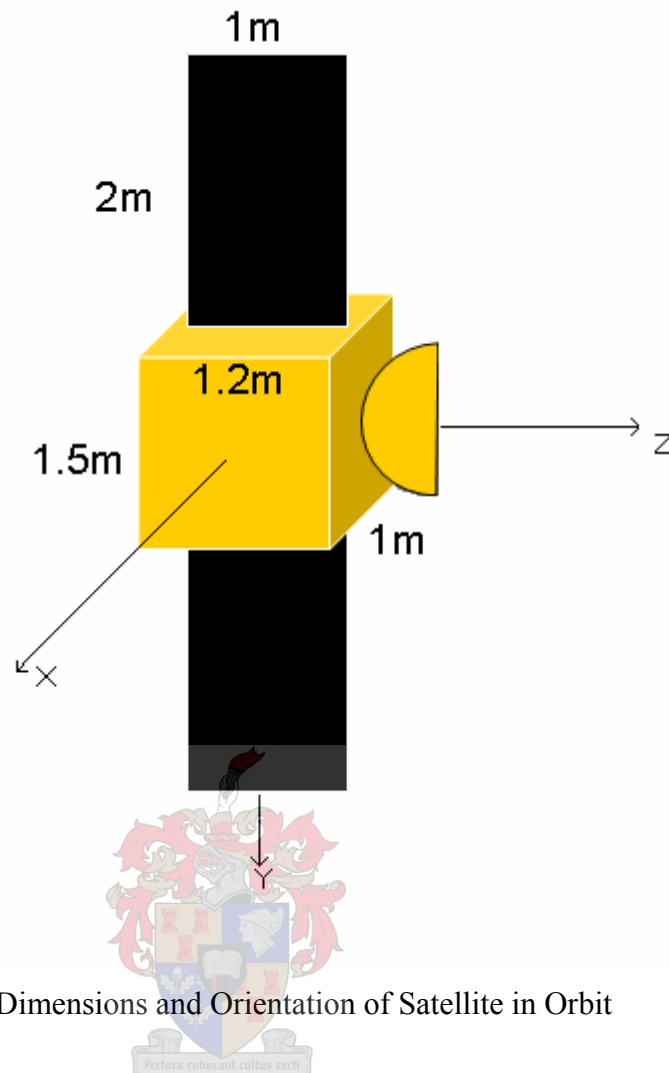
Figure 2.9 Dimensions and Orientation of Satellite in Orbit

2.3.3 Software

The tools used for the simulation purposes are Matlab® and Simulink®. All associated software (models and control algorithm) was written in ANSI C and compiled in Matlab® using the '*mex*' command which is a tool used to compile low and medium level languages in Matlab®.

Chapter 3

Simulation Models

Models are an integral part of any type of simulation study. In this study we require models of the satellite's orbit, Earth's magnetic field, model of the Sun and Earth. Also the disturbance torques acting on the satellite has to be modelled. An analysis of the different models used, will be performed in this chapter.

3.1 SDP4 Orbit Propagator

The SDP4 orbit propagator is an orbit propagator used to propagate the orbit of deep space objects. Any object with an orbital period of more than 225 minutes is categorised as a deep space object. The propagator uses a TLE (two line element) set generated by NORAD as its input. The interpretation of the TLE can be found in Appendix D.

The propagator gets initial values of the satellite's inclination, eccentricity, mean motion, mean anomaly, epoch of orbit (time instant at which TLE was generated), drag term, etc. from the TLE. The input variable to the propagator is the time since epoch. The most important outputs include the altitude, latitude, longitude, geodetic latitude and true anomaly of the satellite.

The propagator takes into account the gravitational effects of the Sun and the Moon on the orbit of the satellite. It also considers the sectoral and tesseral harmonics of the Earth which determines the longitudinal drift on a body due to the oblateness of the Earth. The orbit of the satellite can be propagated for any amount of time.

The TLE used in the simulation study is of the satellite named Astra 1B. Astra 1B was launched on 2nd March, 1991 from Kourou, French Guiana. The satellite has a nominal position of 19.5° East. The graph (Figure 3.1) on the following page shows the longitude and latitude of Astra 1B over a 30 day period. A slight drift in the longitude of the satellite can be observed. This is the reason why station-keeping manoeuvres are required. These techniques are discussed in Chapter 7.
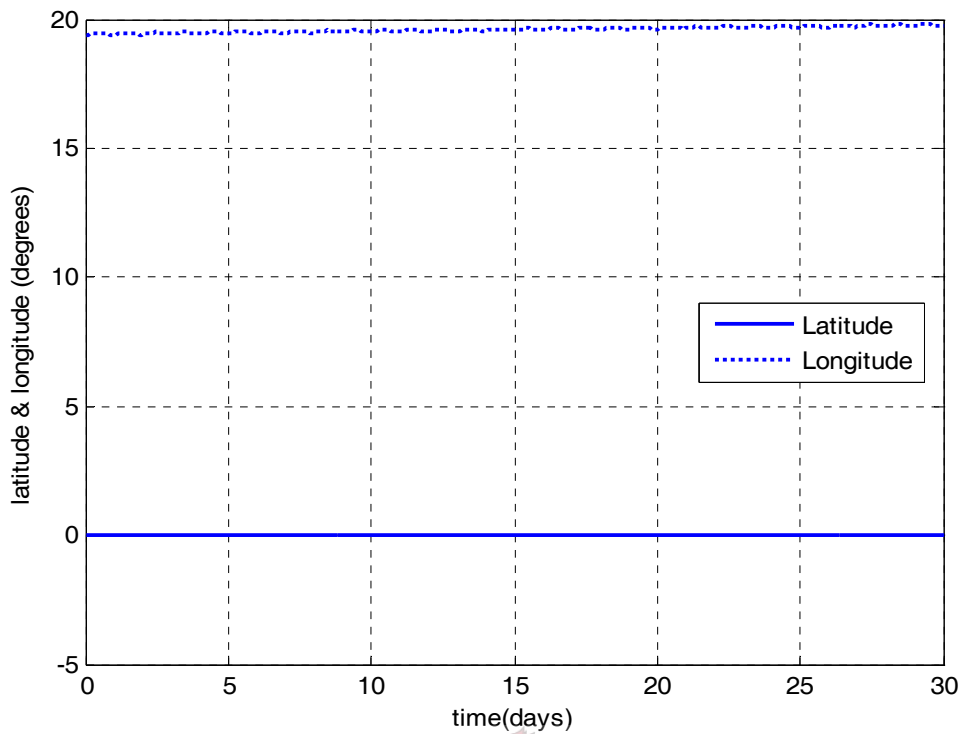
Figure 3.1 Latitude and Longitude of Astra 1B

3.2 IGRF model

The IGRF model is a series of mathematical models of the Earth's magnetic field and its yearly secular variation, which is updated every 5 years by the IAGA. The latest available model is a 13th order model which provides accuracies up to 0.1nTesla. The model used in this study is a 10th order IGRF model which has an accuracy of 1nTesla. The coefficients have been updated for the year 2005. The mathematical modelling is discussed in Appendix C.

The inputs for the IGRF model are obtained from the SDP4 propagator. The generated vector of the IGRF model is transformed from the inertial coordinates to the orbit coordinates. The transformation matrix from the inertial to the orbit frame is discussed in Appendix A. The magnetic field in the orbit coordinates is related to the body coordinates through the DCM. The measurements of the magnetometer will be in body coordinates if the magnetometer is aligned along the body axis. If not, the magnetometer measurements have to be transformed from the sensor coordinates back to body coordinates.

3.3 Sun model

A model of the Sun's orbit is used to determine the altitude and position of the Sun. The distance of the Sun is measured in the *Geocentric* inertial coordinates. This distance vector is then converted to the position in terms of a sub-Sun latitude and longitude point on the Earth's surface. The altitude of the Sun is also calculated. The latitude used here is the geodetic latitude which takes into account the flattening of the Earth at the poles (Wertz, 1978). The idea behind using a model of the Sun, is to have a position vector of the Sun with respect to the satellite as a reference to the FSS and also for modelling the solar radiation torque.

The calculation of the Sun position vector with respect to the satellite is summarised below,

1) Sun vector from satellite in inertial coordinates = Sun vector from Earth in inertial coordinates − Satellite vector from Earth in inertial coordinates

$$\mathbf{S_{SAT}^I = S_{EARTH}^I - Sat_{EARTH}^I}$$

2) Normalise $\mathbf{S_{SAT}^I}$ to obtain the unit vector

$$\mathbf{S_{VEC}^I = \frac{S_{SAT}^I}{\left\| S_{SAT}^I \right\|}}$$

3) Transform $\mathbf{S_{VEC}^I}$ unit vector from inertial to orbit coordinates

$$\mathbf{S_{VEC}^O = [T]S_{VEC}^I}$$

The transformation matrix **[T]** is derived in Appendix A.

3.4 Eclipse model

Modelling the eclipse is very essential in the simulation analysis of a spacecraft. The eclipse duration for a GEO satellite can vary from approximately 70 minutes during the equinoxes, to no eclipse during periods greater than 21 days before and after the equinoxes. A graphical representation (Figure 3.2) is shown next:
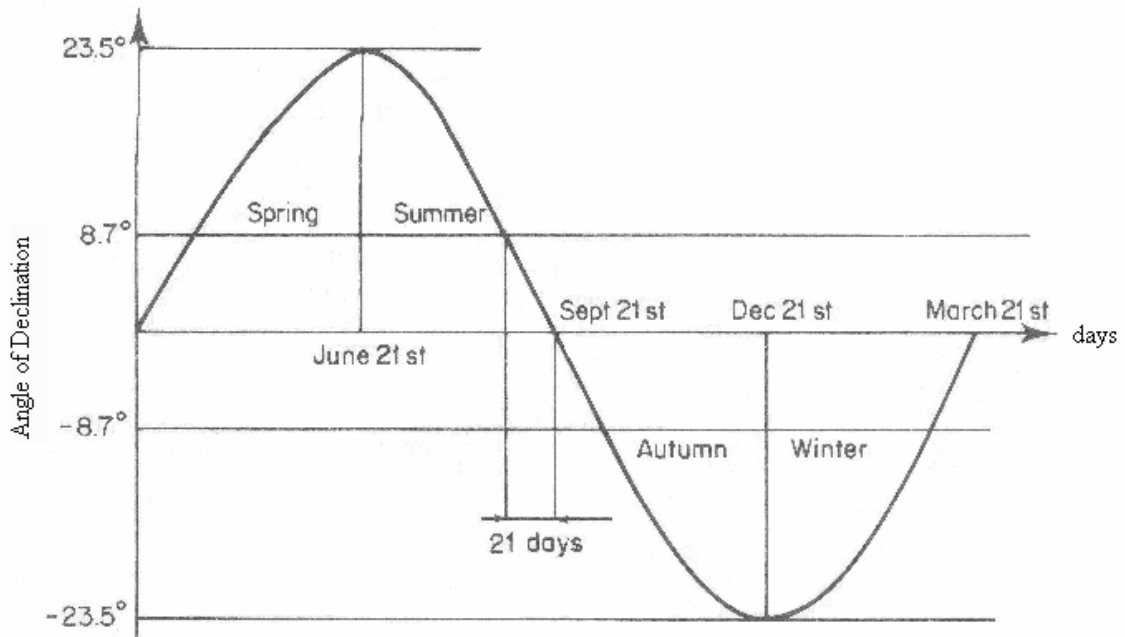
Figure 3.2 Declination of Sun over an entire year

(From Maral and Bossquet, 1986, p 178)

The figure above shows the angle of declination of the Sun with respect to the equator. The declination becomes 23.5 degrees (angle between ecliptic and equatorial plane) during the solstices. As expected the declination becomes zero during the equinoxes. The duration of the eclipse is the maximum at the equinoxes and gradually decreases or increases, after or before the equinox, respectively. Eclipse is absent between declination angles of 23.5 degrees and 8.7 degrees (angular radius of the Earth).

Occurrence of the eclipse in an orbit depends on the angular distance between the Sun and the satellite. Figure 3.3 shows that eclipse occurs when the angular distance between the Sun and the satellite (α) is greater than ($90° + \beta$),

where,

$\beta = \mathrm{acos}(\mathrm{R_E}/\mathrm{R_O})$

$\mathrm{R_E}$ = Equatorial radius of the Earth

$\mathrm{R_O}$ = Radius of Satellite Orbit from the centre of Earth
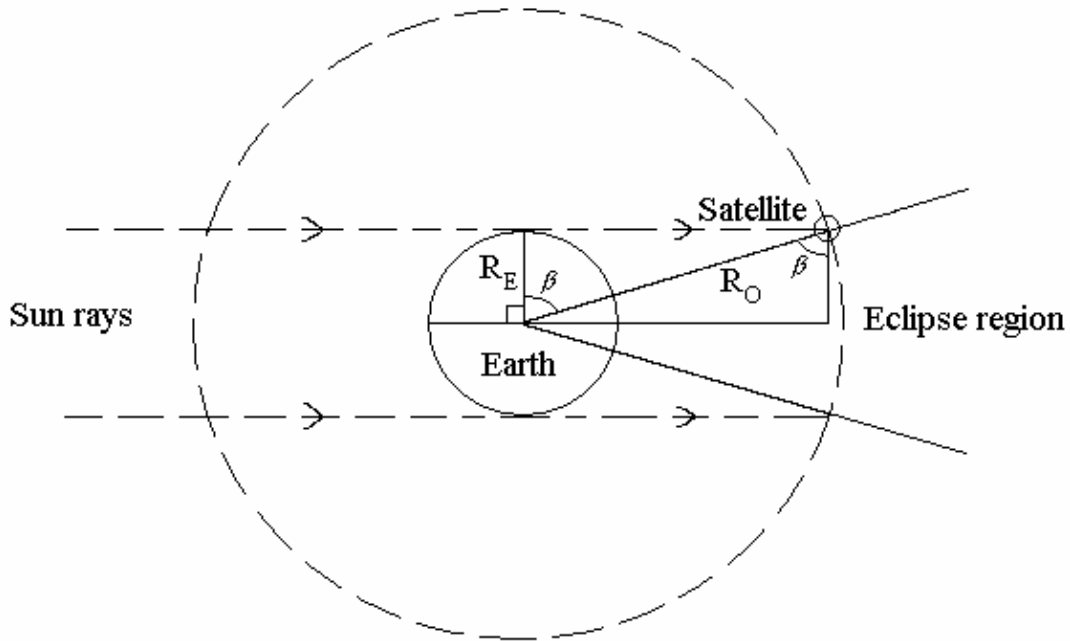
Figure 3.3 Eclipse Geometry

α can be calculated from the Sub-satellite and Sub-Sun points as shown:

$\alpha = $ acos[$\cos(LAT) \cos(SLAT) \cos(LON\text{-}SLON) + \sin(LON) \sin(SLON)$]

LAT, LON = Latitude and longitude of satellite on Earth's surface

SLAT, SLON = Latitude and longitude of Sun on Earth's surface
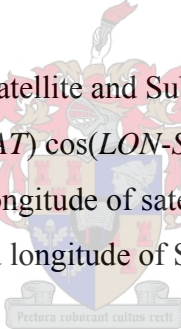
3.5 Nadir vector

The nadir vector is a reference vector which provides the position of the Earth. It constantly points towards the centre of the Earth from the orbit of the satellite. Intuitively from Figure 2.4, one can see that the nadir vector should be in the opposite direction as compared to the position unit vector. The negative unit position vector is then transformed to the orbit coordinates using the transformation matrix.

The nadir (nadia) vector calculation can be summarised as follows,

1) Obtain Nadir unit vector in inertial coordinates.

$$\mathbf{E}^{\mathbf{I}}_{\mathbf{VEC}} = -\overline{\text{pos}}$$

2) Transform Nadir unit vector from inertial to orbit coordinates

$$\mathbf{E}^{\mathbf{O}}_{\mathbf{VEC}} = [\mathbf{T}]\mathbf{E}^{\mathbf{I}}_{\mathbf{VEC}}$$

The transformation matrix **[T]** is the same as in Section 3.3.

3.6 Disturbance torques

The main causes of disturbance torques on any Earth orbiting satellite (near or far) are the following:

1) Aerodynamic Drag
2) Gravity-gradient
3) Solar radiation

We will now calculate each disturbance torque and see which one is significant enough to a level where it requires modelling.

3.6.1 Aerodynamic drag torque

The aerodynamic drag depends on the altitude of the orbit (which influences the velocity of the satellite), spacecraft geometry and location of centre of mass. A simplified scalar approximation is given as,

$$T_{aero} = F(c_{ps} - cm) \qquad (3.1)$$

where,

$$F = 0.5[\rho \, C_d \, A \, V^2]$$
$$\rho = atmospheric \, density \, (\approx 0)$$
$$C_d = drag \, coefficient$$
$$A = projected \, area$$
$$V = spacecraft \, velocity$$
$$c_{PA} = centre \, of \, aerodynamic \, pressure$$
$$cm = centre \, of \, mass$$

The aerodynamic drag can be completely ignored because of the fact that there is no atmosphere above 800km. Since atmospheric density becomes zero, T_{aero} is chosen to be zero as well.

3.6.2 Gravity-gradient torque (GG)

The factors influencing the GG torque are spacecraft inertias and orbit altitude. The GG torque tends to keep the satellite nadir pointing, if there happens to be a misalignment in Roll or Pitch and can be *positively* used for low accuracy attitude stabilisation.

Newton's law and experience tells us that the influence of gravity is less at geostationary altitude as compared to low Earth altitudes. And also the misalignment in Roll and Pitch should be minimal because the satellite has to be nadir pointing always so as to provide continuous coverage. It would still be analytically helpful to have some calculated value for GG torque at geostationary altitude. A simplified expression for GG torque is as given below,

$$T_{gg} = \frac{3\mu}{2R^3}|I_{XX} - I_{ZZ}|sin(2\theta)$$ (3.2)

where,

$$\mu = Earth's\ gravity\ constant(3.986\mathrm{x}10^{14}\ m^3/s^2)$$
$$R = Radius\ of\ orbit$$
$$I_{XX} = Moment\ of\ inertia\ along\ X\ axis(or\ Y\ axis, if\ larger)$$
$$I_{ZZ} = Moment\ of\ inertia\ along\ Z\ axis$$
$$\theta = Deviation\ from\ Z\ axis$$

From the above expression we can calculate the GG torque. Moment of inertia values are calculated in Appendix E. Maximum deviation from Z axis is assumed to be 0.1 degrees. With these values, the GG torque is calculated to be approximately $5.355\mathrm{x}10^{-9}$ Nm. For a more precise and accurate calculation refer Steyn (1995) or Wertz (1978).
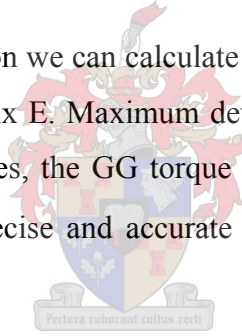
3.6.3 Solar Radiation torque

The solar radiation torque is dependent on the type of surface being projected, the area of the projected surface and the distance between the centre of mass and centre of solar pressure. Solar radiation torque is completely independent of the altitude of the orbit. A simplified expression is,

$$T_{solar} = F(c_{PS} - cm)$$ (3.3)

where,

$$F = \frac{F_S}{c}A_S(1+q)\cos i$$

$$F_S = Solar\ constant(1367W/m^2)$$
$$c = Speed\ of\ light(3\mathrm{x}10^8 m/s)$$
$$A_S = Projected\ Surface\ Area$$
$$q = Reflectance\ factor(say\ 0.6 - usually\ between\ 0\ and\ 1)$$

$$i = Angle\,of\,incidence\,of\,Sun$$
$$c_{PS} = centre\,of\,solar\,pressure$$
$$cm = centre\,of\,mass$$

The term $T_{solar} = F(c_{PS} - cm)$ in true sense is a vector product of the form $\mathbf{T = r\,x\,F}$. For the time being we do the scalar calculation to analyse the magnitude and not the direction.

The solar panel areas are not considered because the two panels will cancel each other out because of opposite vector distances. Therefore projected area calculations need to take into account only the main satellite body and the antenna. The maximum projected area for solar torque calculations would be [(1.5m x 1.2m) + (0.8m x 0.4m)]. The centre of mass will be offset towards the +Z body axis due to the presence of the communications antenna. If the distance between the centre of solar pressure and centre of mass is assumed to be 0.4m and the angle of incidence of the Sun to be 0 degrees (worst case scenario) then,

$$F = 1.5462x10^{-5}\,N$$

and

$$T_{solar} = 6.1824x10^{-6}\,Nm$$

Thus from the calculated values of individual disturbance torques one can conclude that the solar radiation torque is the most significant disturbance torque. The GG torque is lesser than the solar torque by an order of three. Taking this into consideration the GG torque was also ignored. A more accurate and complex model was used to analyse the solar radiation in the simulations.

Chapter 4

Actuators & Sensors

The actuators and sensors are an integral part of any control system. Placement of sensors is also significant so as to optimise the sensing capability.

4.1 Actuators

Actuators are devices used to deliver the control motions (linear or rotational) to the spacecraft according to the measurements from the sensors. The actuators used in the study will be *reaction (momentum) wheels*, *magnetic torque rods* and *reaction thrusters*. Other possible actuators that can be used on GEO satellites are CMGs (Control Moment Gyros) and solar flaps. The CMG is generally used on spacecrafts that are huge and heavy (generally >1000kg) and is complex. Since the mass of the spacecraft in consideration is 500kg the CMG is avoided as the other actuators are capable of providing the required amount of actuation. Solar flaps are external appendages which make use of the solar pressure to perform slow manoeuvres and to damp nutation. It is generally not used on small GEO satellites.

4.1.1 Reaction (Momentum) Wheels

Reaction (momentum) wheels are momentum exchange devices that are used to transfer momentum to the satellite to control its attitude to some commanded reference value. The reaction wheel is a flywheel, which is controlled by an electric motor. Physically the reaction wheel and the momentum wheel is the same. When the reaction wheel is operated at some momentum bias it is called a momentum wheel. From here on, the flywheel will be called a reaction wheel and not a momentum wheel except for cases where a momentum bias is required, for which the latter convention will be used.

The reaction wheel has its own advantages and disadvantages. It is faster compared to the torque rods but slower compared to thrusters. A major advantage of the reaction wheel is that it is a linear actuating device unlike thrusters. The significant disadvantage of a reaction wheel is that it suffers mechanical wear-out

when operated continuously over years. Another disadvantage is that it can generate only torques and not forces.

4.1.2 Magnetic Torque Rods

Magnetic torque rods are actuators which generate a torque using the magnetic field of the Earth and the magnetic moment. The torque rods consist of a magnetic core and a coil. A magnetic moment is produced when the coil is energised by passing current through it. The direction of the torque can be controlled by changing the direction of the current through the coil. Magnetic torque rods do not suffer mechanical wear-out because of the absence of moving parts, thereby lasting throughout the entire mission. Also it doesn't require any fuel which reduces the mass though the rods have their own mass. The torque generated is highly dependent on the magnitude of the magnetic field.
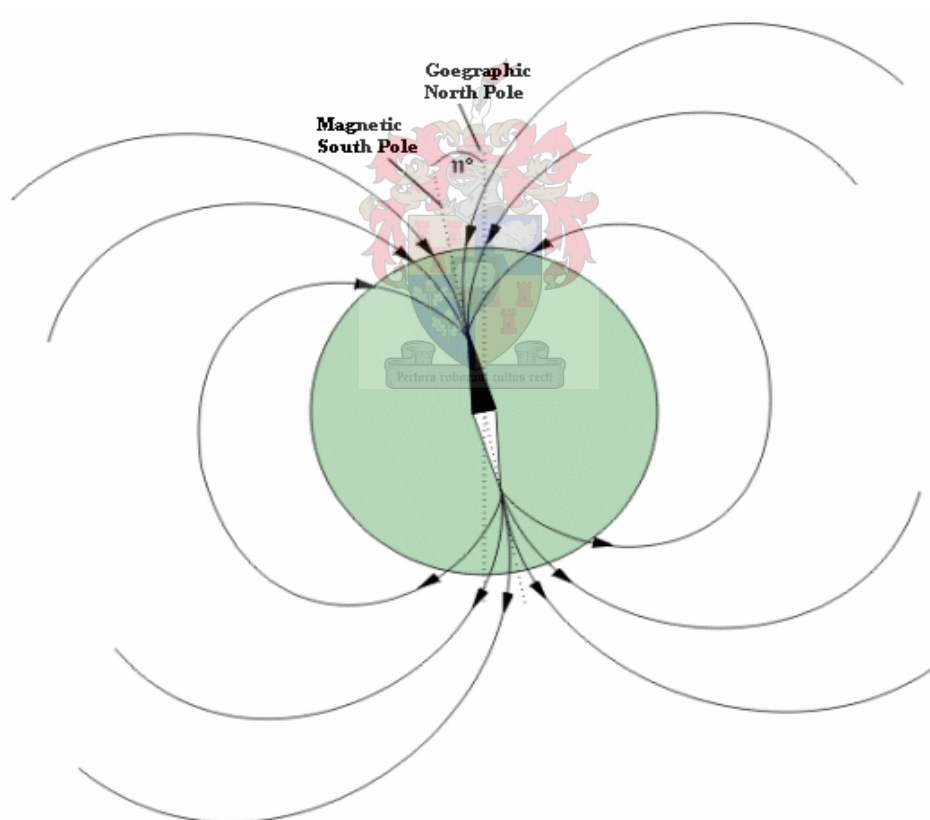
Figure 4.1 Earth's Magnetic field

As shown in Figure 4.1 the magnetic North-South axis is inclined to the geographic North-South axis by approximately 11°. The magnetic field experienced by the satellite depends on the altitude and orientation of the satellite orbit. For a

GEO satellite the magnetic field will always be constant since the satellite is fixed with respect to a point on the Earth. Also the torque producing capability along the Y-axis is limited because the magnetic field is mainly along the same axis. Placing a torque rod along the Y-axis will provide no improvement in performance but just an additional weight burden. Therefore magnetic torque rods are placed only along the X and Z body axis and not along the Y-axis.

A GEO satellite will experience a magnetic field of approximately 100 nTesla. So, if torque rods with a magnetic dipole moment of $75 Am^2$ are used then a torque of 7.5×10^{-3} Nm can be generated. The main disadvantages of the torque rods are that the torques generated are completely dependent on the Earth's field direction and they are slow actuation devices.

4.1.3 Reaction Thrusters

Reaction thrusters are used for various attitude control and orbit control operations. Attitude control is performed using low power thrusters (LPTs) where as orbit control uses high power thrusters (HPTs). The attitude control operations using thrusters will be discussed in Chapter 5 and orbit control operations in Chapter 7. Propulsion systems can be classified according to the propellant used as shown below.
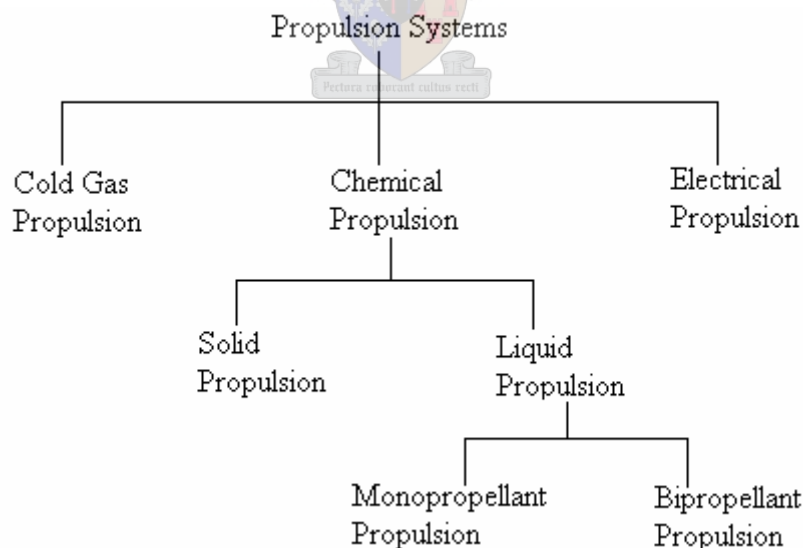
Figure 4.2 Propulsion system classifications

As the classification suggests, the chemical propulsion system offers more options and variations. Complexity and efficiency of the propulsion systems increases

from left to right in Figure 4.2. Chemical propulsion offers a very good trade off in terms of complexity and efficiency.

Solid propulsion is mainly used for stages from lift-off to the placement of the satellite in the orbit whereas liquid propulsion is used for in-orbit operations. The propulsion system used in the analysis of thruster dependent operations will be the monopropellant propulsion system. It offers a slightly better advantage over the bipropellant system in terms of the efficiency to mass ratio of the overall propulsion system. Also monopropellant systems would be a better choice for small GEO satellites. As the name suggests the monopropellant system uses a single propellant and the most popular fuel is hydrazine (N_2H_4) which is also called rocket fuel. Hydrazine can be extremely hazardous if not handled properly. Other fuel options include hydrogen peroxide (H_2O_2).

Thruster arrangement is highly important in all types of mission in order to optimise the performance of the sub-system.
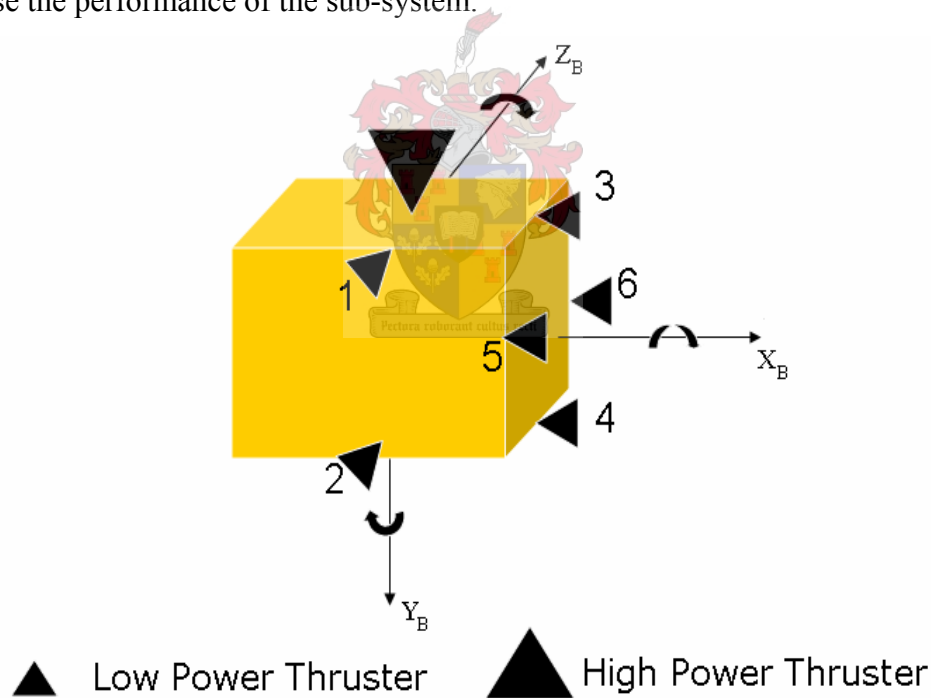
Figure 4.3 Thruster arrangement for a GEO Satellite placed 19.5° East

Thruster arrangement is highly dependent on the type and mission of the orbit. Figure 4.3 shows a single thruster system. Thrusters are arranged such that they can provide control torques (both positive and negative) along each body axis. All satellites will have an additional system to provide redundancy in case of failure. Each thruster has its own application with some of them performing multiple applications.

Table 4.1 Thruster application

Thruster	Manoeuvre
HPT	North-South Station-keeping
LPT (5 and 6) / (3 and 4)	East-West Station-keeping
LPT 2 or LPT 1	Positive Roll or Negative Roll
LPT 5 or LPT 6	Positive Pitch or Negative Pitch
LPT 4 or LPT 3	Positive Yaw or Negative Yaw

It is important to note that there exists no specific thruster arrangement configuration and the arrangement varies from mission to mission. Placement of East-West and North-South station-keeping thrusters requires more explanation and can be found in Chapter 7.

4.2 Sensors

Sensors that are used in ADCS include a magnetometer, FSS, ES and FOGs. All sensors are modelled such that they are mounted along the body axis except for the FSS. The sensor measurements are obtained by transforming the respective reference vectors using the estimated DCM. All physical sensors in reality need to be calibrated. This is avoided in this case because this is a simulation study. Sensor noise is modelled as a random noise signal and then correlated with individual peak sensor noise values.

4.2.1 Magnetometer

The IGRF model (Appendix C) output in orbit coordinates is transformed to body coordinates using the estimated DCM from the EKF. The peak magnetometer noise value is assumed to be 1 nTesla. The magnetometer measurements are used in the EKF and also in the magnetic controllers for the magnetic torque rods. Figure 4.4 shows the magnetic field experienced by the satellite under normal attitude conditions. As expected the highest magnetic field component is along the Y body axis. Also the magnitude of the total field is approximately 101nTesla. This data can be verified by any geomagnetic website (mentioned in bibliography).
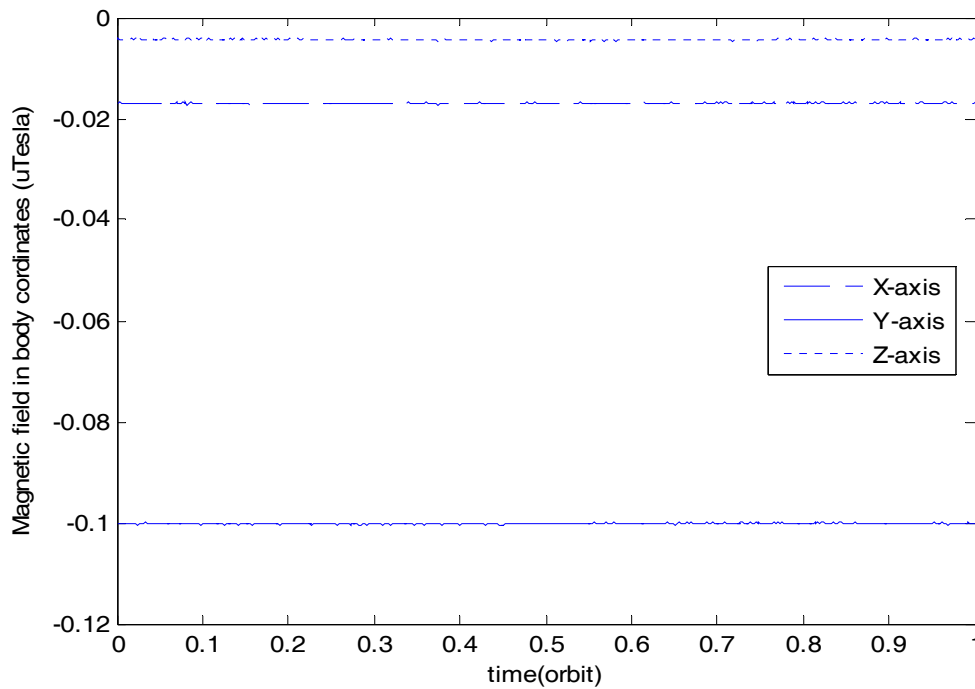
Figure 4.4 Modelled magnetometer output

4.2.2 Earth Sensor

The Earth Sensor (ES) model used is a simplified model of MiDES-G Earth sensor (Appendix F). MiDES-G provides horizon position information along the Roll and Pitch axis. The sensor placement is such that the optical head (boresight) of the sensor points towards the centre of Earth. In other words, it is aligned along the satellite $+Z$ body axis. The sensor has a circular field of view (FOV) of $33.6°$. The optical assembly of MIDES-G makes use of a multi pixel detector array in each of the two (Roll and Pitch) hybrid detector assemblies. Each detector has a high resolution area as well as a low resolution area thereby making it hybrid.

The high resolution area of each detector is modelled to be $26.4°$ (Figure 4.5). The rest of the detector being $7.2°$, is the low resolution part at either end of the detector. The low resolution pixels were modelled to have noise levels three times larger than the high resolution pixel area. So, if the Earth disk were to move about the X or the Y axis by more than $4.5°$ then the output of the sensor will have measurements with larger noise levels. Any change in attitude (along the Roll and Pitch axis) will be directly translated into sensor output which is displayed directly in angles. If the satellite makes a motion of $8.1°$ in Roll or Pitch then the boundary of the Earth disk goes out of the ES's FOV.
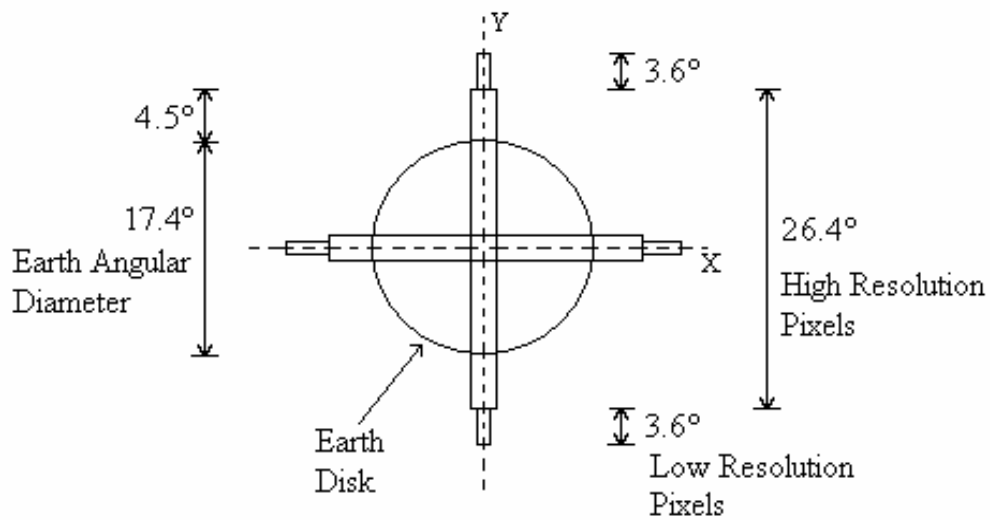
Figure 4.5 Nominal position of Earth Disk on Orthogonal Detectors

The disadvantage of the ES is that it provides no Yaw data which means that any rotation of the spacecraft along the Yaw ($+Z$) axis will not be sensed by the ES. The ES output for step inputs (Roll = 2° and Pitch = 3°) is shown in Figure 4.6
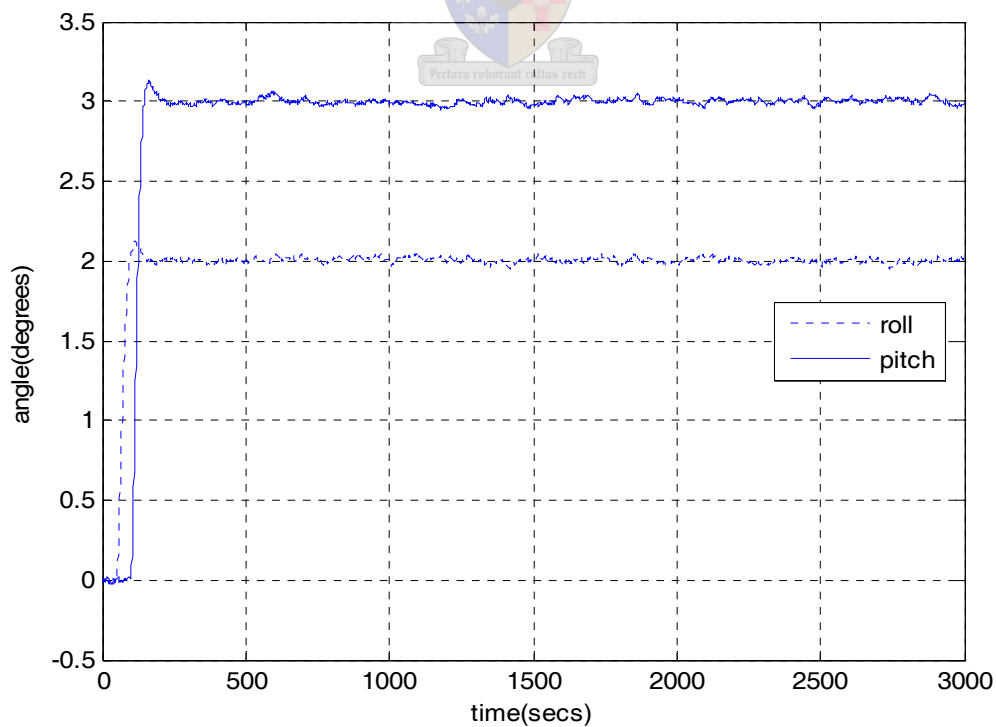
Figure 4.6 Earth sensor output

4.2.3 Fine Sun Sensor

The model of the fine Sun sensor (FSS) is based on the DSS2 (Appendix F). The main feature of the FSS is that it has a very wide rectangular FOV of +/-60 degrees. The FSS has to be optimally placed in order to view the Sun in the best possible manner. The FSS needs a frame of its own (sensor frame) with respect to the satellite. This is because of the fact that if the sensor was to be placed in the body frame the boresight of the sensor would be oriented towards Earth (nadir vector). With a Pitch or Roll rotation of 180° the FSS boresight can be oriented in the opposite direction which helps in negating the influence of eclipse on the sensor. It is important to note that eclipse will still occur on the satellite but just that the FSS would not experience it because the Earth will no longer come in between the FSS and the Sun.

Figure 4.7 shows the geometrical representation of the above mentioned arrangements. It can be intuitively seen that Case b) is a better arrangement as compared to Case a).
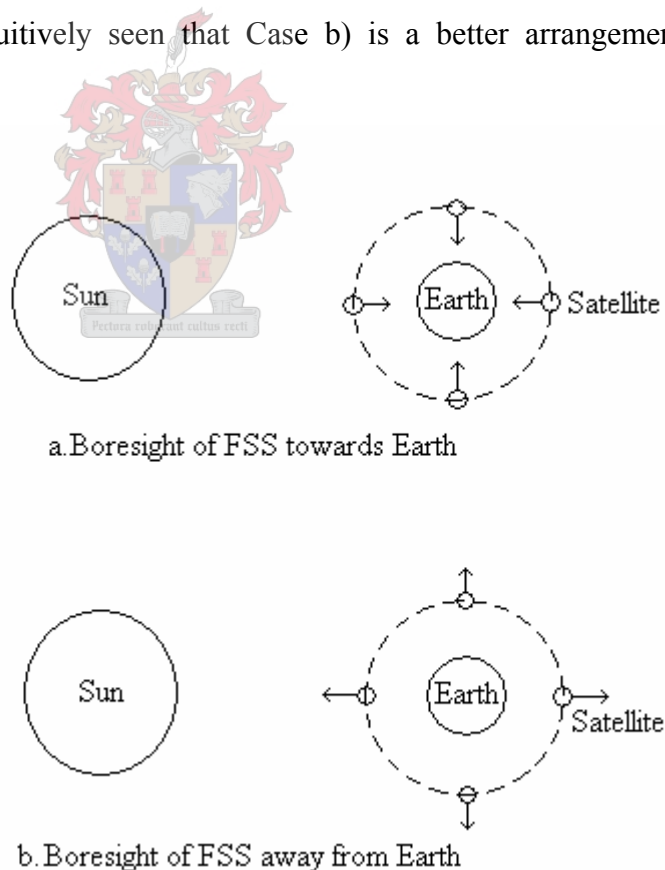
Figure 4.7 Single body mounted FSS arrangements

The other possible arrangement would be to mount the FSS on to the solar panels so that the Sun is always in the FOV of the sensor. The solar panels rotate a

rate of $360°/$day in order to keep the angle between Sun and the panels to be $90°$. This helps in achieving complete coverage of the Sun over an entire orbit period.

Another possibility is to use three FSSs, placed back to back to provide complete orbit coverage of $360°$. This arrangement also provides redundancy. The disadvantage of using three FSSs, is that it makes the overall AODCS hardware very expensive. This arrangement is not widely used. The output of the FSS is in terms of the azimuth and elevation angle of the Sun, with respect to the satellite.

Figure 4.8 shows the output of the FSS in terms of the azimuth and the elevation angle when a single sensor is used while Figure 4.9 gives the FSS angles when three sensors are placed back to back as mentioned in the previous paragraph. The reason for the zero readings (between 0.8 and 0.9 orbit) in Figure 4.9 is due to eclipse. The elevation angle is close to zero in both figures because the TLE used had an epoch close to the equinox.
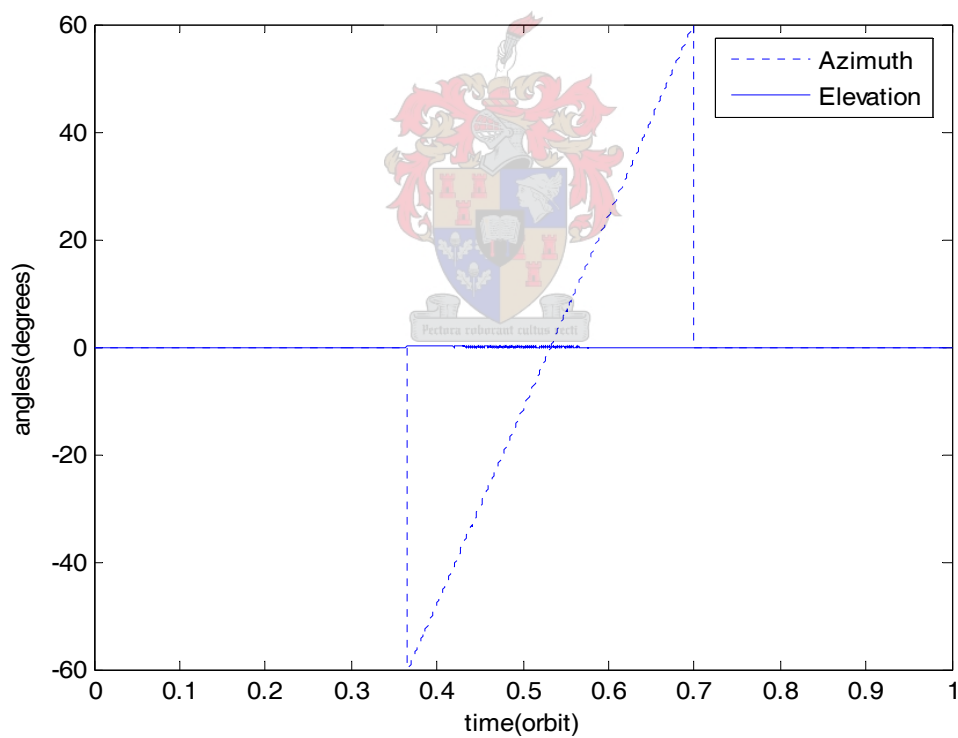
Figure 4.8 Single FSS output
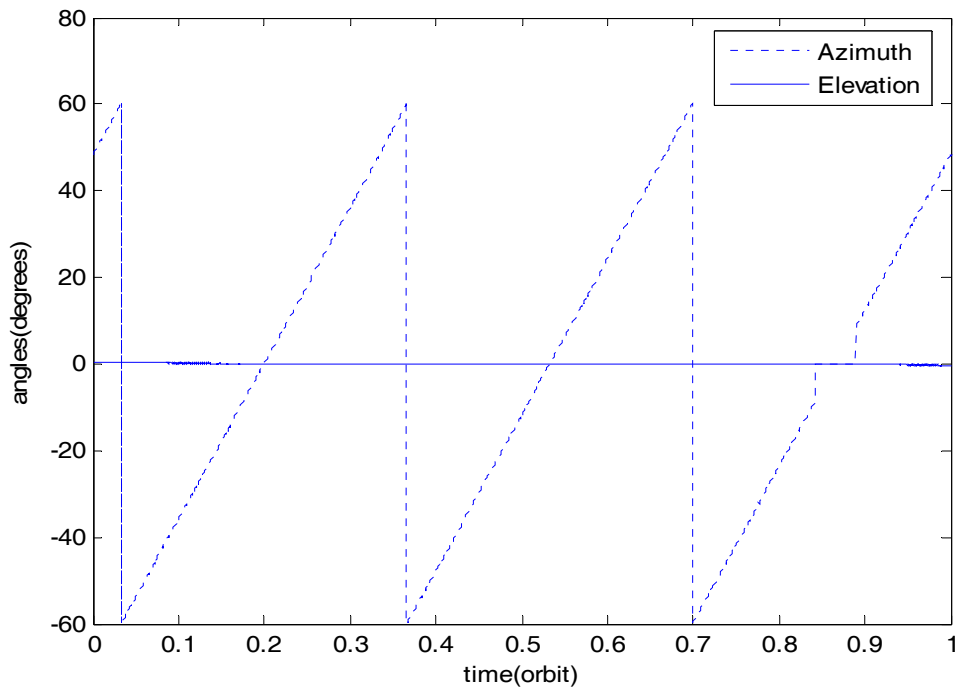
Figure 4.9 Output of three FSSs when placed back to back

4.2.4 Fibre Optic Gyro

FOGs are used to measure the inertial angular velocity of the spacecraft along each axis. In a FOG, light is fed simultaneously into both ends of a long fibre optic coil.
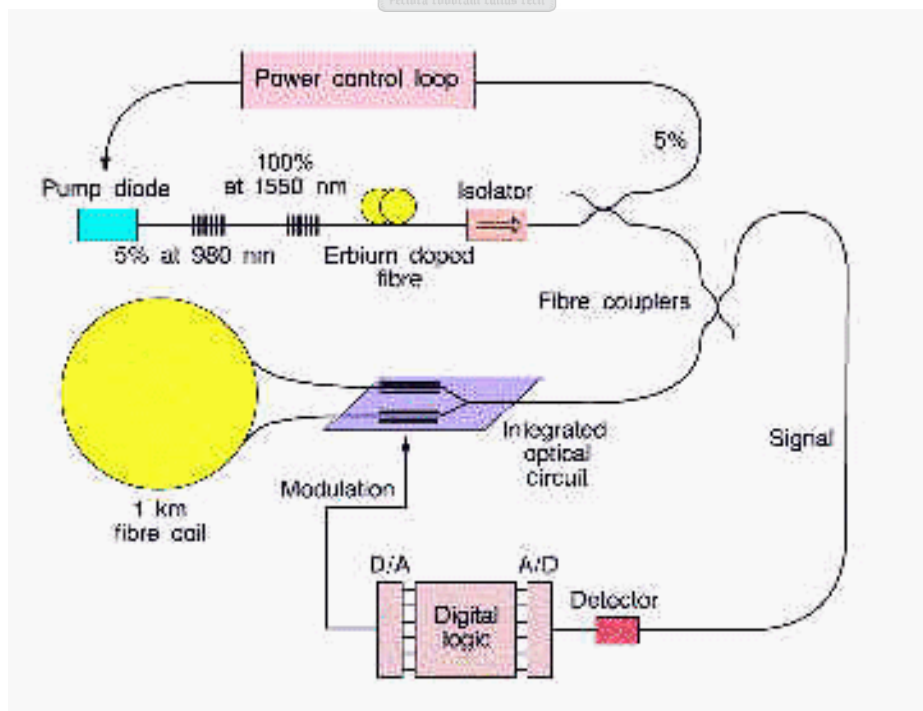
Figure 4.10 FOG internal diagram

When the coil rotates around the centre point, the counter-rotating beams travel slightly different distances before they reach the detector and their phases differ in direct proportion to the input rotation rate. This resulting interference which is measured as a variation in power output, gives the input angular rate. The longer the coil inside the FOG the better the resolution will be. This is the reason why FOGs tend to be very expensive.

Therefore FOGs are used very sparingly. FOGs are used mainly while performing Station-keeping manoeuvres. When FOGs are switched off, the angular rates are estimated (Section 6.1) and used in the feedback controllers. The FOGs had to be modelled for simulation and was done as follows:

$$\boldsymbol{\omega}_{fog}^{I} = \boldsymbol{\omega}_{B}^{I} + \mathbf{b} + \boldsymbol{\eta}_{1} \tag{4.1}$$

where,

$\boldsymbol{\omega}_{fog}^{I}$ = FOG angular rate vector in inertial coordinates

$\boldsymbol{\omega}_{B}^{I}$ = body angular rate vector in inertial coordinates

$\mathbf{b}$ = FOG bias vector

$\boldsymbol{\eta}_{1}$ = FOG measurement noise vector

The FOG bias vector (**b**) degrades the angular rate measurements and has to be estimated. This estimation technique is discussed in Section 6.2.

Chapter 5

Attitude Control

Before discussing control algorithms it is important to determine the actuating capability of the main attitude actuators which are the reaction wheels. This process is also called sizing of wheels. The reaction wheels were considered to have a maximum torque capability of 0.2 Nm (Newton metre). The maximum wheel speed is 6000rpm which provides a wheel angular momentum of 4 Nms (Newton metre second). The torque levels depend on the capability of the DC motor and also on the size of the wheel rotor. The torque equation is given as,

$$\dot{h}_{\mathrm{w}} = T_{\mathrm{w}} = I_{\mathrm{w}}\dot{\omega}_{w} \qquad (5.1)$$

where,

I_{w} = Inertia of the wheel

$\dot{\omega}_{w}$ = Angular acceleration of the wheel

Equation (5.1) tells us that an increase in wheel size (I_{w}) helps us to increase the torque capability, but it is important to note that a larger DC motor will be required to drive a bigger wheel. Therefore increasing the size of the wheel is not the solution to obtain a larger torque, as it would require larger driving requirements. The wheels work on the principle of conservation of angular momentum which means that any angular momentum present on the wheel is transferred to the satellite but with an opposite polarity. This can be represented as,

$$\mathbf{h_{w}} = -\mathbf{h_{sat}} \qquad (5.2)$$

$$\therefore \mathbf{T_{w}} = -\mathbf{T_{C}} \qquad (5.3)$$

Comparing Equation (5.1) and (5.3) we get,

$$\dot{\mathbf{h}}_{\mathbf{w}} = -\mathbf{T_{C}} \qquad (5.4)$$

This principle can be used in momentum biased control which will be discussed in Section 5.3. Momentum bias control also makes use of magnetic control for the remaining axes. It is also essential to design magnetic controllers to perform momentum dumping to prevent angular momentum saturation on the wheels.

5.1 Three axis Reaction Wheel Controllers

In a three axis reaction wheel controller each axis is controlled independently using a reaction wheel. The controllers use attitude and angular rates as inputs. First, a wheel controller using Euler angles as attitude is discussed. But this can give us discontinuity problems thereby giving us reason to use quaternions as an attitude vector for the wheel controllers.

5.1.1 Euler angle Reaction wheel control

The reaction wheel controllers were designed to provide a 5% settling time (t_s) of 150 seconds and to provide a peak overshoot (M_P) of less than 5%. In other words, a damping factor (ζ) of 0.707 for the above mentioned settling time specifications. This leads to closed loop poles of,

$$s_{CL} = -\sigma \pm j\omega_d \tag{5.5}$$

where,

$$t_s = 3/\sigma \text{ with, } \sigma = \zeta\omega_n \text{ \& } \omega_d = \omega_n\sqrt{1-\zeta^2}$$

$$\therefore \ s_{CL} = -0.02 \pm j0.02 \tag{5.6}$$

Control torque delivered by the reaction wheels along each axis can be described as follows,

$$T_{CX}/I_{XX} = K_P(\phi_e) + K_D(\dot{\phi})$$
$$T_{CY}/I_{YY} = K_P(\theta_e) + K_D(\dot{\theta}) \tag{5.7}$$
$$T_{CZ}/I_{ZZ} = K_P(\psi_e) + K_D(\dot{\psi})$$

where ϕ_e, θ_e, ψ_e are the errors between the measured angles and the commanded angles along each axis. $\dot{\phi}$, $\dot{\theta}$, $\dot{\psi}$ are the angular rates along the respective axis. I_{XX}, I_{YY}, I_{ZZ} is calculated in Equation (E.9).

The X-axis control torque can be represented in the s-plane as,

$$T_{CX}(s)/I_{XX} = K_P\phi(s) + K_D s\phi(s) = \phi(s)[K_P + K_D s] \tag{5.8}$$

This can be rewritten as,

$$T_{CX}(s)/I_{XX} = \phi(s)K_D\left[s + \frac{K_P}{K_D}\right]$$

The above equation can be solved using the RL (Root Locus) method. $-K_P/K_D$ is the pole location in the controller and was chosen to be -0.02. K_D is obtained from the RL to satisfy the condition in Equation (5.6). The same method applies to the Y and Z axes as well. The value of K_D from the RL was determined to be 0.04 and K_P thus becomes 0.0008. The obtained gains are then substituted into Equation (5.8).

5.1.2 Quaternion Reaction wheel control

The quaternion feedback controller compensates for the drawbacks of the Euler angle controller in terms of avoiding discontinuities. The attitude is represented in terms of quaternions which is called the current quaternion. The commanded attitude is converted from RPY angles to quaternions. Equations (2.1) and (2.4) are used to obtain the commanded quaternion. Equation (2.4) is used only when q_4 is the largest. If not, the quaternion calculations could lead to numerical inaccuracies. The alternative calculations can be found in Appendix B. Now that both the commanded and measured attitudes are in terms of quaternions, the error quaternion can be calculated. The error quaternion is calculated as,

$$
\begin{bmatrix} q_{1e} \\ q_{2e} \\ q_{3e} \\ q_{4e} \end{bmatrix} = \begin{bmatrix} q_{4c} & q_{3c} & -q_{2c} & -q_{1c} \\ -q_{3c} & q_{4c} & q_{1c} & -q_{2c} \\ q_{2c} & -q_{1c} & q_{4c} & -q_{3c} \\ q_{1c} & q_{2c} & q_{3c} & q_{4c} \end{bmatrix} \begin{bmatrix} q_1 \\ q_2 \\ q_3 \\ q_4 \end{bmatrix}
\tag{5.9}
$$

where,

$\mathbf{q_e} = \mathbf{q} \ominus \mathbf{q_c}$ = error quaternion

$\mathbf{q_c}$ = commanded quaternion

$\mathbf{q}$ = measured quaternion

The error quaternion is based on quaternion division rather than normal subtraction. Quaternion division is discussed in Appendix B. Equation (5.8) needs to be modified and can be re-written in general for all three axes as (Wie, 1998),

$$
\mathbf{T_C} = -\mathbf{I}[\mathbf{K_P}\mathbf{q_{vec}} + \mathbf{K_D}\boldsymbol{\omega}_B^O]
\tag{5.10}
$$

where,

$\mathbf{T_C} = [T_{CX} \; T_{CY} \; T_{CZ}]^T$, control torques along each axis

$\mathbf{I} = \text{diag}[I_{XX} \; I_{YY} \; I_{ZZ}]^T$, principle axis moment of inertia of the satellite

$$\mathbf{q_{vec}} = [q_{1e} \; q_{2e} \; q_{3e}]^T \qquad , \text{vector part of error quaternion}$$

$$\mathbf{K_P} = \text{diag}[k_1 \; k_2 \; k_3]^T \quad , \text{angular control gains along each axis}$$

$$\mathbf{K_D} = \text{diag}[d_1 \; d_2 \; d_3]^T \quad , \text{angular rate control gains along each axis}$$

It would be easier to analyse the control over a single axis and then generalise in order to have a clearer understanding. Consider a small roll rotation of Φ degrees along the X-axis. The closed loop dynamics along the X-axis becomes,

$$I_{XX} \dot{\omega}_{BX}^I + \dot{h}_X = T_{DX} \tag{5.11}$$

This equation is obtained from Equation (2.8) by ignoring the gyroscopic effects which will be negligible for small rotations. Equation (5.11) can be rewritten as,

$$I_{XX} \ddot{\phi} + d_1 I_{XX} \dot{\phi} + k_1 I_{XX} \sin\left(\frac{\phi}{2}\right) = T_{DX} \tag{5.12}$$

where,

$$\dot{\phi} = \omega_{ox} \approx \omega_{ix} \text{ and } \dot{h}_{wx} = -T_{CX} = I_{XX}\left[k_1 q_{1e} + d_1 \omega_{ox}\right]$$

T_{DX} = External disturbance torque along X-axis

and,

$$\mathbf{q_{vec}} = \left[\sin\left(\frac{\phi}{2}\right) \; 0 \; 0\right]$$
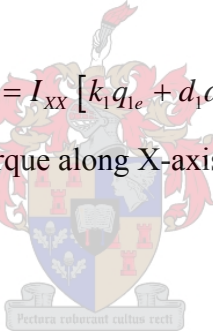
The Laplace transform of Equation (5.12) for small errors in roll angle (ϕ) is,

$$[s^2 + d_1 s + (k_1 / 2)]\phi(s) = T_{DX} / I_{XX} \tag{5.13}$$

Equation (5.13) is similar to a damped second order system where, $d_1 = 2\zeta\omega_n$ and $k_1 = 2\omega_n^2$. The control gains can be now calculated for the specifications mentioned in Section 5.1.1. The same analysis applies for the Y and Z axis as well. The control gains are calculated as: $\mathbf{K_P} = \text{diag}[0.0016 \; 0.0016 \; 0.0016]^T$

$$\mathbf{K_D} = \text{diag}[0.04 \; 0.04 \; 0.04]^T$$

It is important to note that even though the control gains are the same for all three axes, the control torques are also dependent on the moment of inertia along each axis. In other words the control torques for a similar step input along all three axes will be scaled due to the presence of the inertia term '**I**' in Equation (5.10).

Table 5.1 Settling time versus Actuating capability versus Control gains

Settling Time (seconds)	Maximum step input possible (degrees)			K_P	K_D
	X-axis	Y-axis	Z-axis		
120	25	90	30	0.025	0.05
150	40	180	45	0.0016	0.04
180	60	180	65	0.00111	0.033

Table 5.1 shows that as the settling time is made larger the control gains decrease which provides a larger actuating capability for a reaction wheel with a maximum torque level of 0.2 Nm. The settling time of 150 seconds provides a good trade off between the speed of the control system and the attainable step inputs. Large manoeuvres are not necessary for a GEO satellite as it has to be constantly Earth pointing. In spite of this, it is always essential to provide enough room for actuation during the early acquisition stages and for station change, though the latter is very rarely performed.

5.2 Momentum Dumping

Momentum dumping or momentum unloading is an integral part of all satellite control systems. Momentum build up is the increase or decrease in angular velocity of the wheel due to external disturbance torques. The main disturbance torque as discussed in Section 3.6 is the solar radiation torque. A profile of the radiation torque which takes into account the position of the Sun and the satellite dimensions in Figure 2.9 is shown in Figure 5.1. All torque components that are cyclic but non-symmetric will have a bias component which causes the momentum to build up on the wheels.

Momentum can be dumped using magnetic torque rods or reaction thrusters. Using magnetic rods is the more popular option, because they do not consume any propellant and can be smooth (linear) actuators. But, if the dumping needs to be achieved in a minimal amount of time, then thrusters are preferred. Also if the magnetic field is not strong enough, thrusters might be preferred.
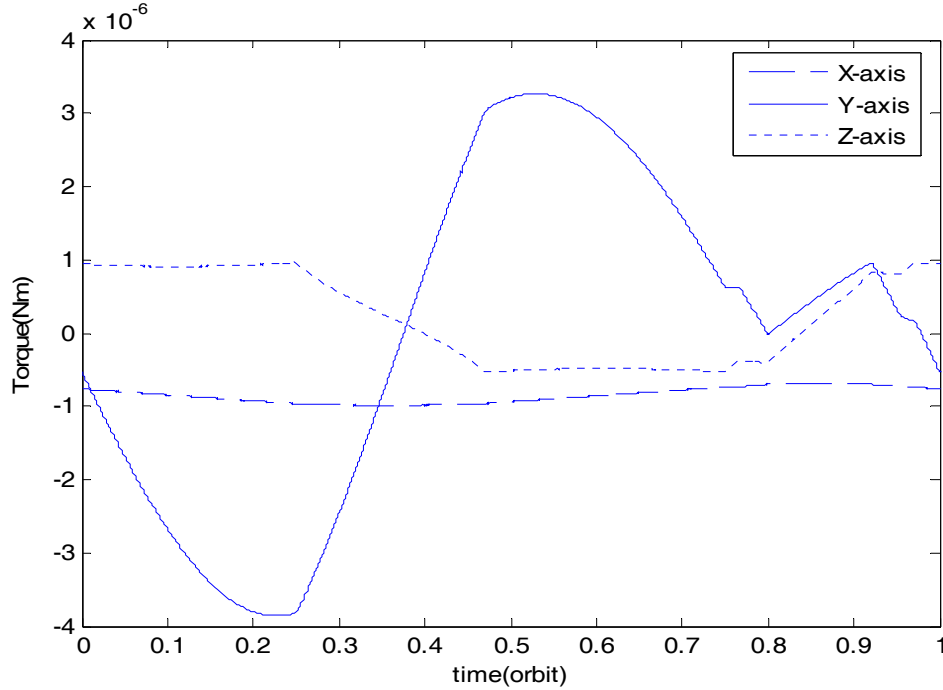
Figure 5.1 Solar Radiation Torque profile (for Nadir pointing satellite)

The initial control equation for momentum dumping (unloading) according to Sidi (1997) can be defined as,

$$\mathbf{T_M} = -k\Delta\mathbf{h} = -k(\mathbf{h_w} - \mathbf{h_{wN}})$$
(5.14)

where,

$\mathbf{T_M}$ = Control torque delivered by magnetic rods

k = dumping control gain

$\mathbf{h_w}$ = wheel momentum vector

$\mathbf{h_{wN}}$ = nominal (desired) wheel momentum vector

The torque generated by the magnetic rods can be defined in general as (Section 4.1.2),

$$\mathbf{T_M} = \mathbf{M} \times \mathbf{B}$$
(5.15)

where, $\mathbf{M}$ = magnetic moment vector of the magnetic rods

$\mathbf{B}$ = geomagnetic field vector in body coordinates (Equation C.14)

Equating the above two equations we get,

$$-k\Delta\mathbf{h} = \mathbf{M} \times \mathbf{B}$$
(5.16)

Equation (5.16) can be rewritten as,

$$
\begin{bmatrix} k_X \Delta h_X \\ k_Y \Delta h_Y \\ k_Z \Delta h_Z \end{bmatrix} = \begin{bmatrix} 0 & B_Z & -B_Y \\ -B_Z & 0 & B_X \\ B_Y & -B_X & 0 \end{bmatrix} \begin{bmatrix} M_X \\ M_Y \\ M_Z \end{bmatrix}
\tag{5.17}
$$

The aim is to determine **M**, which cannot be done from Equation (5.17) because the matrix in the equation is singular. In order to solve this problem we use the vector product of **B** on both sides of Equation (5.16).

$$
\mathbf{B} \times (-k\Delta\mathbf{h}) = \mathbf{B} \times (\mathbf{M} \times \mathbf{B})
$$
$$
= B^2\mathbf{M} - \mathbf{B}(\mathbf{M.B})
\tag{5.18}
$$

When the applied magnetic moment **M** is perpendicular to the Earth's magnetic field **B**, the term **M.B** in Equation (5.18) becomes zero. With this assumption **M** becomes,

$$
\mathbf{M} = -\frac{k}{B^2}(\mathbf{B} \times \Delta\mathbf{h})
\tag{5.19}
$$

Equation (5.19) can now be substituted in Equation (5.15) to obtain the magnetic torque delivered by the magnetic rods which is,

$$
\mathbf{T_M} = -\frac{k}{B^2}[B^2\Delta\mathbf{h} - \mathbf{B}(\mathbf{B.}\Delta\mathbf{h})]
\tag{5.20}
$$

The next step is to determine the dumping (unloading gain) '*k*'. The control torque $\mathbf{T_M}$ in general is time varying because the Earth's magnetic field varies with time. But for a GEO satellite the magnetic field is almost constant as discussed in Section 4.2.1. In spite of the almost constant **B** field the torque is not constant because of the varying excessive momentum $\Delta\mathbf{h}$, which is dependent on the solar radiation disturbance torque. This leads to a trial and error approach to determine *k*.

Ideally the easiest way to start is to choose *k* as *zero* which effectively means that momentum dumping is disabled. Momentum build-up on the wheels was observed for 10 orbit periods in the presence of the solar disturbance torque in Figure 5.1. The wheel momentum profile is shown in Figure 5.2. It can be seen that momentum builds up on the X and Z wheels where as the Y wheel momentum does not. This is because of the near symmetric nature of the disturbance torque component in the Y-axis. This simulation helps in deciding how often momentum

dumping needs to be done. Even though the momentum saturation level of the wheels was assumed to be 4 Nms, allowing the wheel momentum to build up beyond a certain level (say 1 Nms) would require large magnetic torques to dump the momentum. This can be achieved by increasing the size of the torque rods which is not always the solution, as it would lead to larger power consumption and weight.
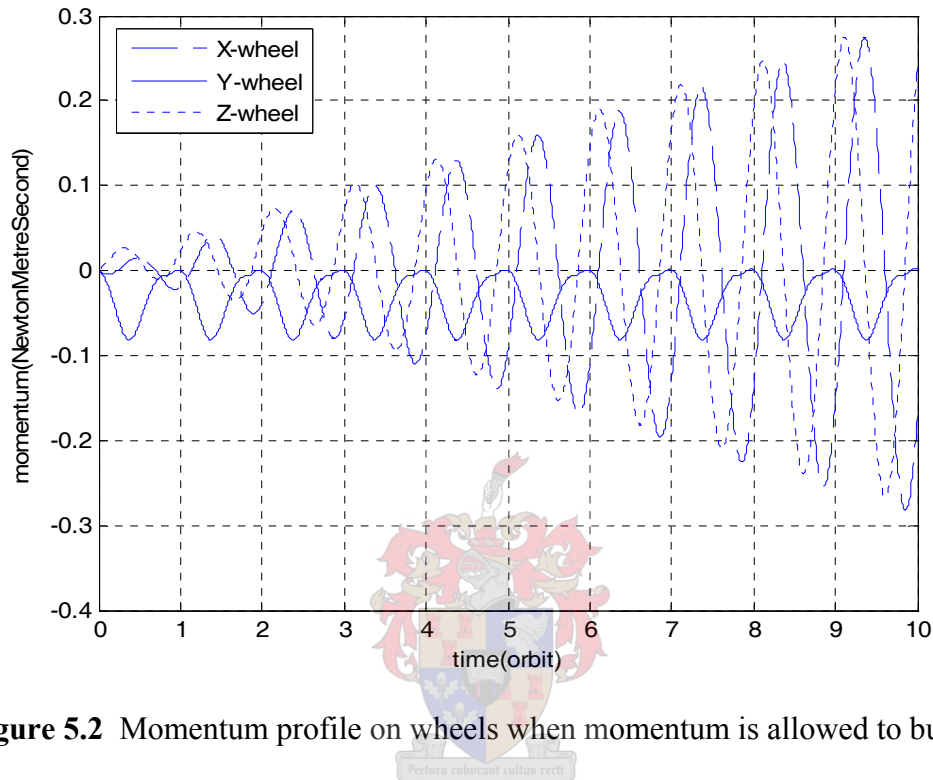
Figure 5.2 Momentum profile on wheels when momentum is allowed to build up

Therefore the rods need to be sized taking into consideration the above mentioned factors. The momentum can be allowed to build up to 0.4 Nms which by observing the above graph might be reached around 15 to 16 orbit periods. The momentum on the X and Z wheels were initialised with a momentum vector of 0.4 Nms. Different values (saturation levels-$150 \, \text{Am}^2$, $100 \, \text{Am}^2$, $75 \, \text{Am}^2$, $50 \, \text{Am}^2$) of magnetic rods were used in simulation. The saturation level of the rods was chosen so as to achieve an optimal trade-off between the weight of the rods, maximum producible torque and performance time (dumping time of excessive momentum). A comparison of the physical characteristics of different magnetic rods can be found in Sidi (1997, p.400). A $75 \, \text{Am}^2$ magnetic rod which weighs around 2.0 kg can provide a maximum magnetic torque of $7.5 \, \mu\text{Nm}$. This is seen as a good trade off between the different requirements. Magnetic rods are placed along the X and Z-axis and not

along the Y-axis for reasons mentioned in Section 4.1.2. The dumping time of the controller is determined by the value k.

Different simulations were performed for different values of k. The criterion of choice is dependent on the settling time of the wheel momentum and the magnetic moment profile of the magnetic rods. All simulations were performed with initial wheel momentum values of $\mathbf{h} = [0.4, -0.1, 0.4]$ Nms. These values were chosen under the assumption that momentum dumping is done once in every 15 to 16 days. Three sets of values were chosen for k:

1) $k = [25, 0, 25]$
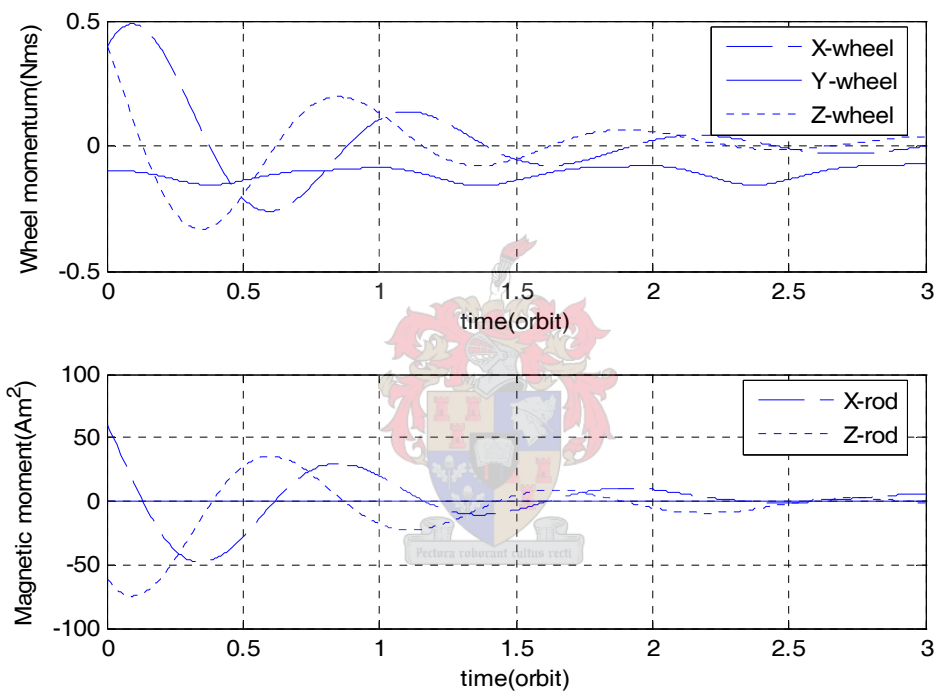
Figure 5.3(a) Wheel momentum versus Magnetic moment for case 1)

Simulations for other values of k are shown overleaf and so forth. Comparisons of the three graphs and Table 5.2 show that the system in case 2) performs optimally.

Table 5.2 Comparison of Momentum Dumping Controller with different values of k

Case no:	Dumping time requirement	Saturation of Magnetic Rods
1)	Largest (2.5 orbits)	Absent
2)	Less than 1) (1.5 orbits)	Present
3)	Less than 2) (1.2 orbits)	Larger than 2)

The table is almost self explanatory. As expected with lower values of k in case 1) the momentum on the wheels get dumped very slowly but helps in avoiding saturation of the magnetic rods. Increasing the gains help in making the dumping process faster, but at the expense of actuator saturation.

2) $k = [50, 0, 50]$
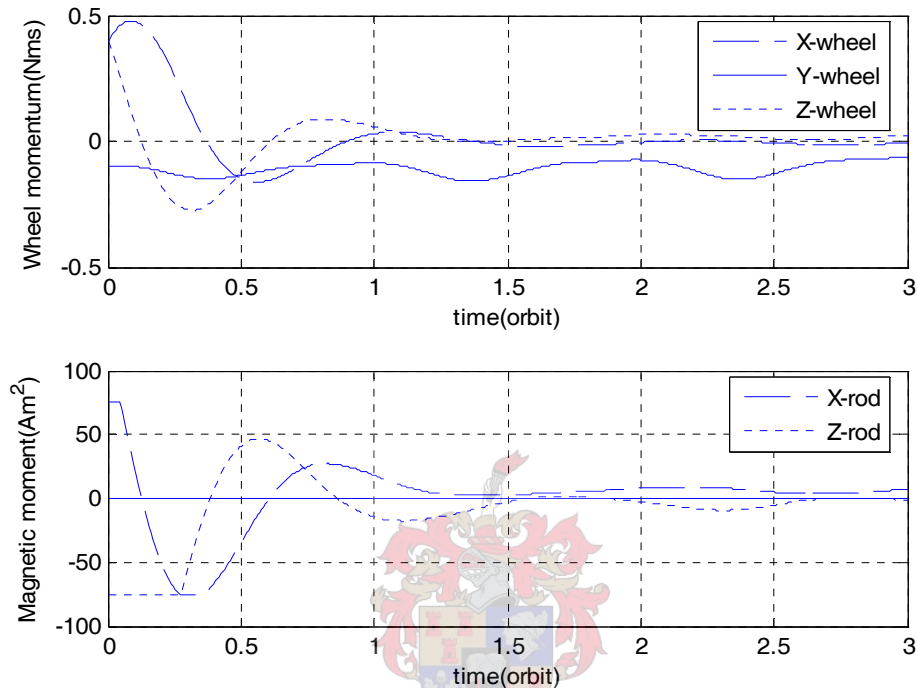
Figure 5.3(b) Wheel momentum versus Magnetic moment for case 2)

Saturation of the rods also degrades the performance of the controller since the adequate torques required to dump the momentum cannot be generated if the rods remain saturated. Comparison of case 2) and 3) shows a lesser rod saturation time without significant compromise on dumping time for case 2). The gains were further fine tuned to optimise overall performance. The final gain values are $k = [56, 0, 50]\,Am^2$. These gain values are then substituted in Equation (5.20).

It is also important to note that in spite of the absence of a magnetic rod along the Y-axis the momentum along this axis was reducible to acceptable levels. This is possible because of the very weak coupling torque produced by the X and Z magnetic rods.

3) $k = [75, 0, 75]$
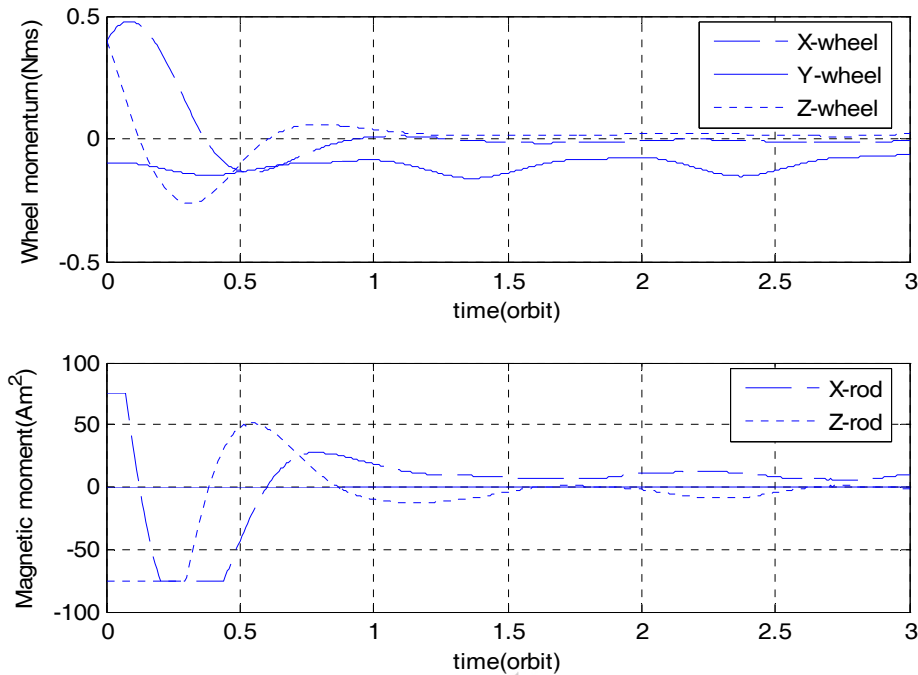
Figure 5.3(c) Wheel momentum versus Magnetic moment for case 3)

5.3 Momentum Bias Control

A momentum biased system has a constant angular momentum which is provided by a momentum wheel (Section 4.1.1). The momentum vector which is along the orbital plane provides the spacecraft inertial stability and this phenomenon is known as gyroscopic stiffness. The gyroscopic stiffness reduces the effect of external disturbance torques on the X and Z axis. This is demonstrated during the design of the control system. Momentum bias alone is not sufficient to provide three axis stability to the system. Some sort of active control has to be performed to keep the satellite within the stringent accuracy requirements.

The advantage of a momentum biased system is that if active control is disrupted along either the X or Z axis or both, due to actuator failure, the satellite does not go into a free attitude drift. A zero momentum system does not have this feature. The disadvantage of the momentum bias system is that larger control torques will be required to perform manoeuvres along the X and Z axis as compared to the zero momentum bias system. Control capability along the Y-axis is achieved by the momentum wheel. There are two possible ways of performing momentum biased control. The normal method is to have attitude knowledge from the FSS and ES and

use it in the control scheme. The other method is to have no knowledge about the yaw axis (only ES is used) and to determine the control torque for the Z-axis using data from the roll axis. Both control schemes will be discussed in detail.

The dynamic equations of motion for a momentum biased spacecraft in GEO orbit is as shown (derived in Section A.2.1),

$$
\begin{aligned}
T_{DX} + T_{CX} &= I_{XX}\ddot{\phi} - \omega_o h_{wy}\dot{\phi} - h_{wy}\dot{\psi} \\
T_{DZ} + T_{CZ} &= I_{ZZ}\ddot{\psi} - \omega_o h_{wy}\psi + h_{wy}\dot{\phi} \\
T_{DY} + T_{CY} &= I_{YY}\ddot{\theta} + \dot{h}_{wy}
\end{aligned}
\tag{5.21}
$$

where,

$T_{D(X/Y/Z)}$ = Disturbance torques along the respective axis

$T_{C(X/Y/Z)}$ = Control torques along the respective axis

$I_{(XX/YY/ZZ)}$ = Moment of inertia along respective principle axis

$\phi, \dot{\phi}, \ddot{\phi}$ = angular displacement, rate and acceleration along the X-axis

$\psi, \dot{\psi}, \ddot{\psi}$ = angular displacement, rate and acceleration along the Z-axis

$h_{wy}, \dot{h}_{wy}$ = Y-wheel momentum

ω_o = orbit angular rate or orbit frequency
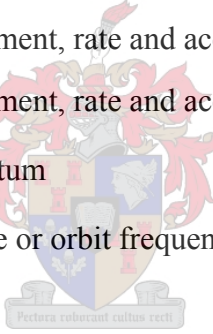
According to the discussion in Sidi (1997), the X and Z axis will be analysed together due to the coupling involved where as the Y-axis analysis is quite straight forward as it is being controlled by the momentum wheel. Equation (5.21) shows the coupling between X and Z axis and the independent nature of the Y-axis quite clearly. The X and Z axis components of Equation (5.21) can be Laplace transformed and written in the matrix from as,

$$
\begin{bmatrix}
s^2 - \dfrac{\omega_o h_{wy}}{I_{XX}} & -\dfrac{s h_{wy}}{I_{XX}} \\
\dfrac{s h_{wy}}{I_{ZZ}} & s^2 - \dfrac{\omega_o h_{wy}}{I_{ZZ}}
\end{bmatrix}
\begin{bmatrix}
\phi(s) \\
\psi(s)
\end{bmatrix}
=
\begin{bmatrix}
T_{DX}(s) \\
T_{DZ}(s)
\end{bmatrix}
\tag{5.22}
$$

The inverse of Equation (5.22) is,

$$\begin{bmatrix} \phi(s) \\ \psi(s) \end{bmatrix} = \frac{1}{\Delta(s)} \begin{bmatrix} s^2 - \dfrac{\omega_o h_{wy}}{I_{XX}} & -\dfrac{s h_{wy}}{I_{XX}} \\ \dfrac{s h_{wy}}{I_{ZZ}} & s^2 - \dfrac{\omega_o h_{wy}}{I_{ZZ}} \end{bmatrix} \tag{5.23}$$

where,

$$\Delta(s) = s^4 + \left[-\omega_o h_{wy} \left(\frac{1}{I_{XX}} + \frac{1}{I_{ZZ}} \right) + \frac{h_{wy}^2}{I_{XX} I_{ZZ}} \right] s^2 + \frac{\omega_o^2 h_{wy}^2}{I_{XX} I_{ZZ}}$$

since $h_{wy} >> \omega_o (I_{XX} + I_{ZZ})$,

$$\Delta(s) \approx (s^2 + \omega_o^2) \left(s^2 + \frac{h_{wy}^2}{I_{XX} I_{ZX}} \right) \tag{5.24}$$

Equation (5.24) contains two second order poles. The first one being at the orbit frequency and the second at the nutation frequency (ω_{nut}) with $\omega_{nut} = \dfrac{h_{wy}}{\sqrt{I_{XX} I_{ZZ}}}$

5.3.1 Normal Momentum bias control

The analysis continues from Equation (5.24). Since the two second order poles in the equation are undamped, the aim of the control algorithm is to damp these poles and to decrease the steady state errors. The control torques along the X and Z axis are,

$$\begin{aligned} T_{CX} &= -(k_{PX}\phi + k_{DX}\dot{\phi}) \\ T_{CZ} &= -(k_{PZ}\psi + k_{DZ}\dot{\psi}) \end{aligned} \tag{5.25}$$

Equation (5.25) is then substituted into Equation (5.21) giving us

$$\begin{aligned} T_{DX} &= I_{XX}\ddot{\phi} - \omega_o h_{wy}\phi - h_{wy}\dot{\psi} + (k_{PX}\phi + k_{DX}\dot{\phi}) \\ T_{CZ} &= I_{ZZ}\ddot{\psi} - \omega_o h_{wy}\psi + h_{wy}\dot{\phi} + (k_{PZ}\psi + k_{DZ}\dot{\psi}) \end{aligned} \tag{5.26}$$

Performing Laplace transforms on the above equation gives,

$$\begin{bmatrix} \dfrac{T_{DX}(s)}{I_{XX}} \\ \dfrac{T_{DZ}(s)}{I_{ZZ}} \end{bmatrix} = \begin{bmatrix} s^2 + \dfrac{1}{I_{XX}}(k_{PX} + s k_{DX} - \omega_o h_{wy}) & -\dfrac{s h_{wy}}{I_{XX}} \\ \dfrac{s h_{wy}}{I_{ZZ}} & s^2 + \dfrac{1}{I_{ZZ}}(k_{PZ} + k_{DZ}s - \omega_o h_{wy}) \end{bmatrix} \begin{bmatrix} \phi(s) \\ \psi(s) \end{bmatrix} \tag{5.27}$$

The inverse of the above Equation (5.27) being,

$$\begin{bmatrix} \phi(s) \\ \psi(s) \end{bmatrix} = \frac{1}{\Delta(s)} \begin{bmatrix} s^2 + \dfrac{1}{I_{ZZ}}(k_{PZ} + k_{DZ}s - \omega_o h_{wy}) & \dfrac{sh_{wy}}{I_{XX}} \\[2ex] -\dfrac{sh_{wy}}{I_{ZZ}} & s^2 + \dfrac{1}{I_{XX}}(k_{PX} + sk_{DX} - \omega_o h_{wy}) \end{bmatrix} \begin{bmatrix} \dfrac{T_{DX}(s)}{I_{XX}} \\[2ex] \dfrac{T_{DZ}(s)}{I_{ZZ}} \end{bmatrix} \quad (5.28)$$

where,

$$\begin{aligned} \Delta(s)I_{XX}I_{ZZ} = {} & s^4 I_{XX} I_{ZZ} + s^3 (k_{DX} I_{ZZ} + k_{DZ} I_{XX}) \\ & + s^2 [k_{DX} k_{DZ} + h_{wy}^2 + I_{ZZ}(k_{PX} - \omega_o h_{wy}) + I_{XX}(k_{PZ} - \omega_o h_{wy})] \\ & + s[k_{DZ}(k_{PX} - \omega_o h_{wy}) + k_{DX}(k_{PZ} - \omega_o h_{wy})] \\ & + [k_{PX} k_{PZ} + (\omega_o h_{wy})^2 - \omega_o h_{wy}(k_{PX} k_{PZ})] \end{aligned} \quad (5.29)$$

It is essential that all the coefficients of the term above must be positive in order to ensure stable roots. This can be done by substituting $h_{wy} = -h$ with, $h > 0$. Thus, Equation (5.29) becomes,

$$\begin{aligned} \Delta(s)I_{XX}I_{ZZ} = {} & s^4 I_{XX} I_{ZZ} + s^3 (k_{DX} I_{ZZ} + k_{DZ} I_{XX}) \\ & + s^2 [k_{DX} k_{DZ} + h^2 + I_{ZZ}(k_{PX} + \omega_o h) + I_{XX}(k_{PZ} + \omega_o h)] \\ & + s[k_{DZ}(k_{PX} + \omega_o h) + k_{DX}(k_{PZ} + \omega_o h)] \\ & + [k_{PX} k_{PZ} + (\omega_o h)^2 + \omega_o h(k_{PX} k_{PZ})] \end{aligned} \quad (5.30)$$

The proportional gains k_{PX} and k_{PZ} determine the final steady state errors. Therefore these gains can be calculated from the final value theorem. Using Equation (5.28) and Equation (5.30) the steady state equations (next page) are derived. The intermediate steps involved are derived in Section A.2.2.

$$\phi_{SS} = \frac{(k_{PZ} + \omega_o h)T_{DX}}{k_{PX} k_{PZ} + (\omega_o h)^2 + \omega_o h(k_{PX} k_{PZ})} \quad (5.31)$$

$$\psi_{SS} = \frac{(k_{PX} + \omega_o h)T_{DZ}}{k_{PX} k_{PZ} + (\omega_o h)^2 + \omega_o h(k_{PX} k_{PZ})} \quad (5.32)$$

Equations (5.31) and (5.32) are multiplied by terms $(k_{PX} + \omega_o h)$ and $(k_{PZ} + \omega_o h)$ respectively which leads us to the final steady state equations,

$$\phi_{SS} = \frac{T_{DX}}{(k_{PX} + \omega_o h)} \quad \text{and} \quad \psi_{SS} = \frac{T_{DZ}}{(k_{PZ} + \omega_o h)} \quad (5.33)$$

Equation (5.33) can be rearranged to obtain the proportional gain values.

$$k_{PX} = \frac{T_{DX} - \omega_o h \phi_{ss}}{\phi_{ss}} \quad \text{and} \quad k_{PZ} = \frac{T_{DZ} - \omega_o h \psi_{ss}}{\psi_{ss}} \qquad (5.34)$$

The remaining task is to determine the differential gains which are done by assuming that the determinant in Equation (5.30) is made up of two second order terms with damped poles. The determinant can also be written as,

$$\Delta(s) = (s^2 + 2\zeta_1 \omega_{n1} s + \omega_{n1}^2)(s^2 + 2\zeta_2 \omega_{n2} s + \omega_{n2}^2) \qquad (5.35)$$

The coefficients of the polynomials in Equations (5.30) and (5.35) are equated to determine the unknowns which are k_{DX}, k_{DZ}, ω_{n1} and ω_{n2}. Once k_{DX} and k_{DZ} are determined it is possible to substitute these gains along with the gains in Equation (5.34) back into Equation (5.26).

For the practical simulation, values of T_{DX} and T_{DZ} were chosen from Figure 5.1. The peak disturbance torque values are 1μNm for both T_{DX} and T_{DZ}. The steady state error requirements (ϕ_{ss} and ψ_{ss}) were chosen to be $0.05°$. It is important to convert the steady state error to radians before substitution into Equation (5.34). The value of 'h' was chosen to be 2 Nms. Thus both k_{PX} and k_{PZ} are calculated as 0.0010.

Both damping coefficients were chosen to be 0.707. These were then substituted in Equation (5.35). Now the coefficients in Equations (5.30) and (5.35) can be equated to determine the unknowns. The unknowns are calculated to be,

$k_{DX} = 3.14728$, $k_{DZ} = 0.334291$, $\omega_{n1} = 0.00067$ rad/sec and $\omega_{n2} = 0.00559$ rad/sec

The last two terms show the location of the closed loop poles. The calculated gain values are them substituted in Equation (5.25). The control torque for the Y-axis is calculated as shown in Section 5.1.2 and control gains for Y-axis are exactly the same as calculated in the second row of Table 5.1.

The actuators used for supplying the control torques along the X and Z-axis are normally magnetic torque rods or thrusters. However magnetic rods are used in this case.

Equation (5.15) can be also written as,

$$\begin{bmatrix} T_{MX} \\ T_{MY} \\ T_{MZ} \end{bmatrix} = \begin{bmatrix} 0 & B_Z & -B_Y \\ -B_Z & 0 & B_X \\ B_Y & -B_X & 0 \end{bmatrix} \begin{bmatrix} M_X \\ M_Y \\ M_Z \end{bmatrix} \tag{5.36}$$

$\mathbf{T_M}$ is replaced by $\mathbf{T_C}$. The term M_Y is replaced by $\dot{h}_{wy}$ (wheel torque along Y-axis), since we use only two magnetic rods (long the X and Z-axis) as mentioned in Section 5.2. The modified matrix is of the form,

$$\begin{bmatrix} T_{CX} \\ T_{CY} \\ T_{CZ} \end{bmatrix} = \begin{bmatrix} 0 & 0 & -B_Y \\ -B_Z & 1 & B_X \\ B_Y & 0 & 0 \end{bmatrix} \begin{bmatrix} M_X \\ \dot{h}_{wy} \\ M_Z \end{bmatrix} \tag{5.37}$$

The inverse of Equation (5.37) is,

$$\begin{bmatrix} M_X \\ \dot{h}_{wy} \\ M_Z \end{bmatrix} = \frac{1}{B_Y^2} \begin{bmatrix} 0 & 0 & B_Y \\ B_X B_Y & B_Y^2 & B_Y B_Z \\ -B_Y & 0 & 0 \end{bmatrix} \begin{bmatrix} T_{CX} \\ T_{CY} \\ T_{CZ} \end{bmatrix} \tag{5.38}$$

Now M_X and M_Z can be substituted into Equation (5.36) thus generating magnetic torques that are applied to the satellite. M_Y in Equation (5.36) is zero since there is no magnetic torque rod along the Y-axis. $\dot{h}_{wy}$ is the torque applied to the satellite by the Y-wheel. The system is now three axis stabilised.

Note: It is very important that the proportional gains (k_{PX} and k_{PZ}) should be multiplied by a factor of two when quaternions are used to represent attitude, in the control algorithm. This relation can be observed in the controllers in Section 5.1 as well. Also the wheel momentum $h_{wy} = -2$ Nms, is used in simulation since $h_{wy} = -h$.

Figure 5.4 shows the attitude, the control torques, magnetic torques and wheel torque delivered to the satellite. The X and Z-axis steady state errors are less than $0.05°$, which was the design requirement. The control torques can be observed to be exactly opposite in polarity to the disturbance torque in Figure 5.1.
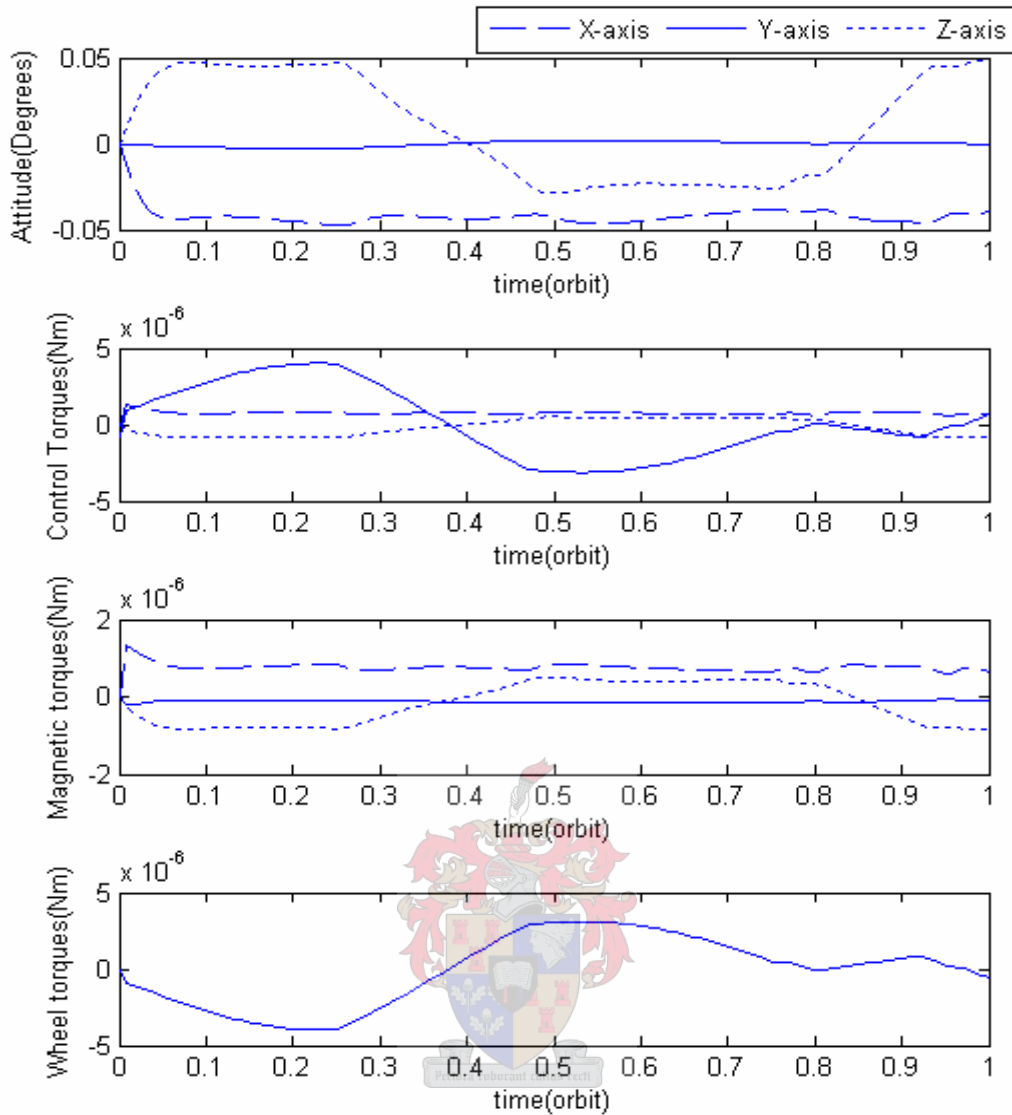
Figure 5.4 Momentum bias control

The magnetic torques track the control torques reasonably well in spite of the weak magnetic field. The Y-axis magnetic torque is due to the coupling between the X and Z-axis magnetic rods. The wheel torque delivered to the Y-axis by the momentum wheel is equal in magnitude but opposite in sign to the control torque. This satisfies the condition in Equation (5.3).

5.3.2   Momentum bias control without Yaw data

This control algorithm is widely used because of the lesser amount of ADCS hardware involved (Sidi, 1997). Since only the roll and pitch angles are measured, the ES is the only sensor being used. The drawback of this algorithm is the reduced accuracy along the yaw axis. This does not affect communication performance, as the

boresight of the antenna is along the yaw axis. The disadvantage might be reduced power system efficiency as the Sun rays are no more normal to the solar panels. As long as accuracies are maintained within the prescribed limits along the other two axes, communication can be performed without any interruption. The control torque equations along the X and Z-axis can be written as,

$$
\begin{aligned}
T_{CX} &= -(k_{PX}\phi + k_{DX}\dot{\phi}) \\
T_{CZ} &= -aT_{CX}
\end{aligned}
\tag{5.39}
$$

The control torque along the X-axis is similar as in the Section 5.3.1 where as the Z-axis torque is proportional to the X-axis torque. This is because in a momentum biased satellite, the roll and yaw errors interchange every quarter of an orbit. In other words, the roll error changes to a yaw error every quarter orbit. Therefore by controlling the roll error, the yaw error also gets controlled accordingly. Equation (5.39) can be substituted into Equation (5.21) giving,

$$
\begin{aligned}
T_{DX} &= I_{XX}\ddot{\phi} - \omega_o h_{wy}\phi - h_{wy}\dot{\psi} + (k_{PX}\phi + k_{DX}\dot{\phi}) \\
T_{DZ} &= I_{ZZ}\ddot{\psi} - \omega_o h_{wy}\psi + h_{wy}\dot{\phi} - ak_{PX}\psi - ak_{DX}\dot{\psi}
\end{aligned}
\tag{5.40}
$$

As in the previous section, the Laplace transform is performed;

$$
\begin{bmatrix} \dfrac{T_{DX}(s)}{I_{XX}} \\[3mm] \dfrac{T_{DZ}(s)}{I_{ZZ}} \end{bmatrix} = \begin{bmatrix} s^2 + \dfrac{1}{I_{XX}}(k_{PX} + sk_{DX} - \omega_o h_{wy}) & -\dfrac{sh_{wy}}{I_{XX}} \\[3mm] \dfrac{(sh_{wy} - ak_{PX} - sak_{DX})}{I_{ZZ}} & s^2 - \dfrac{\omega_o h_{wy}}{I_{ZZ}} \end{bmatrix} \begin{bmatrix} \phi(s) \\[3mm] \psi(s) \end{bmatrix}
\tag{5.41}
$$

The inverse of the Equation (5.41) is calculated as,

$$
\begin{bmatrix} \phi(s) \\[3mm] \psi(s) \end{bmatrix} = \dfrac{1}{\Delta(s)} \begin{bmatrix} s^2 - \dfrac{\omega_o h_{wy}}{I_{ZZ}} & \dfrac{sh_{wy}}{I_{XX}} \\[3mm] -\dfrac{(sh_{wy} - ak_{PX} - sak_{DX})}{I_{ZZ}} & s^2 + \dfrac{1}{I_{XX}}(k_{PX} + sk_{DX} - \omega_o h_{wy}) \end{bmatrix} \begin{bmatrix} \dfrac{T_{DX}(s)}{I_{XX}} \\[3mm] \dfrac{T_{DZ}(s)}{I_{ZZ}} \end{bmatrix}
\tag{5.42}
$$

where,

$$
\begin{aligned}
\Delta(s)I_{XX}I_{ZZ} ={}& s^4 I_{XX}I_{ZZ} + s^3 k_{DX}I_{ZZ} \\
&+ s^2[-\omega_o h_{wy}(I_{XX} + I_{ZZ}) + I_{ZZ}k_{PX} + h_{wy}^2 - ah_{wy}k_{DX}] \\
&+ s[-ah_{wy}k_{PX} - \omega_o h_{wy}k_{DX})] \\
&+ [(\omega_o h_{wy})^2 - \omega_o h_{wy}k_{PX})]
\end{aligned}
\tag{5.43}
$$

For stability reasons it is essential to have all the coefficients of the determinant to be positive. This is done by choosing $h_{wy} = -h$ with, $h > 0$. Therefore Equation (5.43) becomes,

$$
\begin{aligned}
\Delta(s) I_{XX} I_{ZZ} = {} & s^4 I_{XX} I_{ZZ} + s^3 k_{DX} I_{ZZ} \\
& + s^2 [\omega_o h (I_{XX} + I_{ZZ}) + I_{ZZ} k_{PX} + h^2 + ah k_{DX}] \\
& + s[ah k_{PX} + \omega_o h k_{DX})] \\
& + [(\omega_o h)^2 + \omega_o h k_{PX})]
\end{aligned}
\tag{5.44}
$$

The proportional gain k_{PX} is calculated from Equation (5.34) as mentioned in section 5.3.1. Equations (5.44) and (5.35) are equated to determine the differential gain k_{DX} and 'a' along with the natural frequencies ω_{n1} and ω_{n2}.

For simulation, T_{DX} is chosen as 1μNm from Figure 5.1, ϕ_{SS} is chosen to be 0.05° and 'h' as 2 Nms. Thus k_{PX} is calculated as 0.0010. Both damping coefficients are chosen to be 0.707. By equating Equations (5.44) and (5.35) the unknowns are calculated as,

$$k_{DX} = 2.47072, \, a = 0.308551, \, \omega_{n1} = 0.000257 \text{ rad/sec and } \omega_{n2} = 0.00529 \text{ rad/sec}$$

The control gains (k_{PX} and k_{DX}) along with 'a' is substituted into Equation (5.39). Once this is done the actuator (magnetic rod) torques are generated in a similar manner as mentioned from Equations (5.36) to (5.38).

Note: k_{PX} is multiplied by two when attitude is expressed in terms of quaternions and the wheel momentum $h_{wy} = -2$ Nms is used in simulation since $h_{wy} = -h$.

The various control and actuator torques along with the attitude is shown in Figure 5.5. The interesting observation is that the torques (control and magnetic) along the X-axis is larger than a normal momentum biased system, while the torques along the Z-axis is lesser than the normal case. This is because the X-axis control loop puts in extra effort to stabilise the entire system.
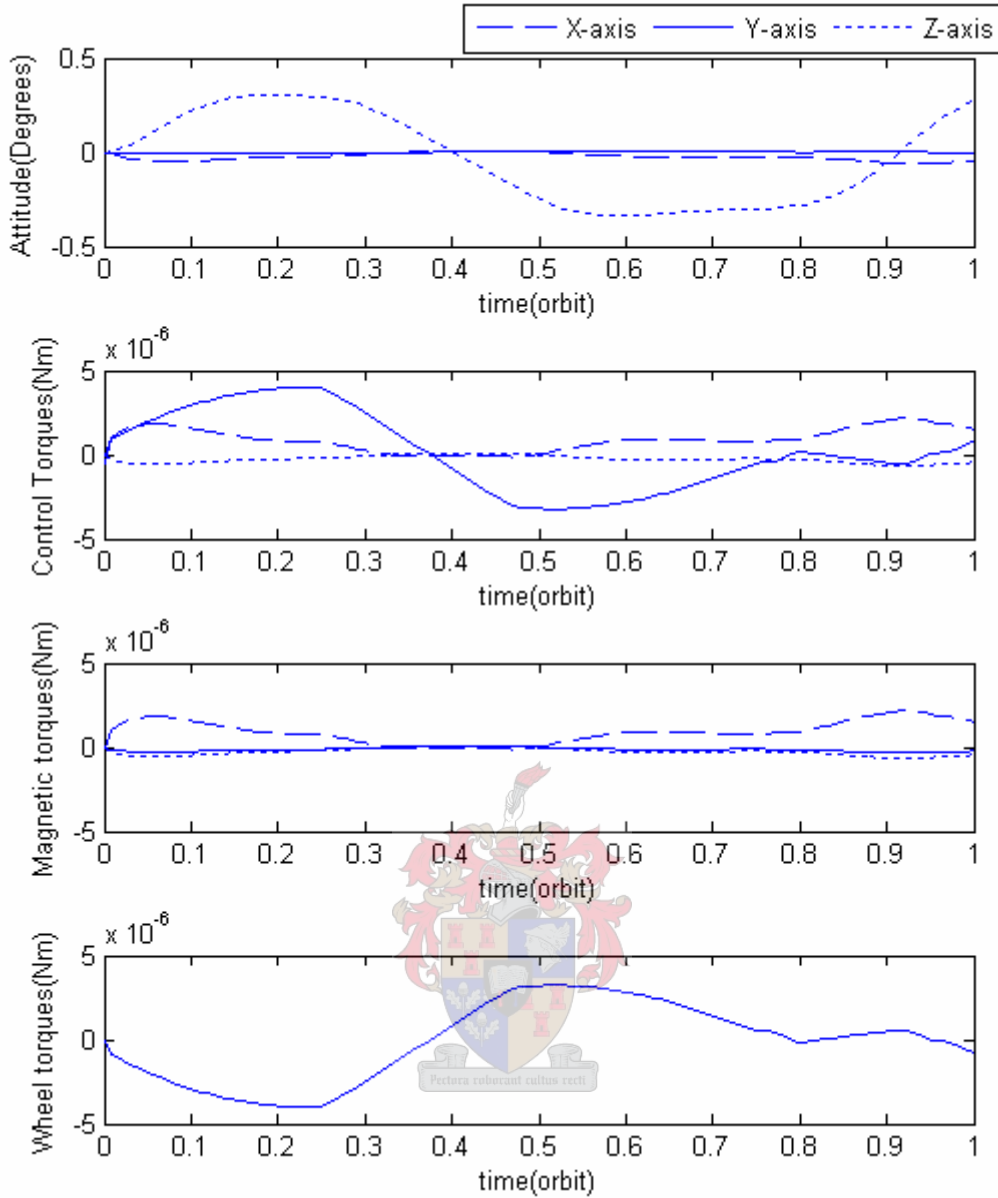
Figure 5.5 Momentum bias control (without yaw data)

As expected the steady state error along the Z-axis is greater. The error though is less than $0.5°$. This can be verified by using the expression,

$$\psi_{SS} \approx \frac{T_{DZ} - aT_{DX}}{\omega_o h} \qquad (5.45)$$

Thus, it can be concluded that this algorithm is be used when lower accuracy levels are acceptable without degrading communication performance significantly and with the advantage of reduced ADCS hardware.

5.4 Reaction Thruster Control

Active three axis control using reaction thrusters is done very rarely as it is a very propellant hungry control algorithm. Since thrusters happen to be non-linear actuating devices they are operated in a limit-cycle mode which means that the satellite is allowed to drift to one end of its accuracy limit at which point a thruster gets fired. The satellite is then allowed to drift to the other end of its accuracy limit where an equal but opposite thruster is fired. In other words thrusters provide bang-bang type of control. The satellite tends to go through marginal vibrational disturbances which could be harmful for the deployed solar panels. Hence this method is employed only in the case of emergencies where other actuators might have failed or when large control torques are required.
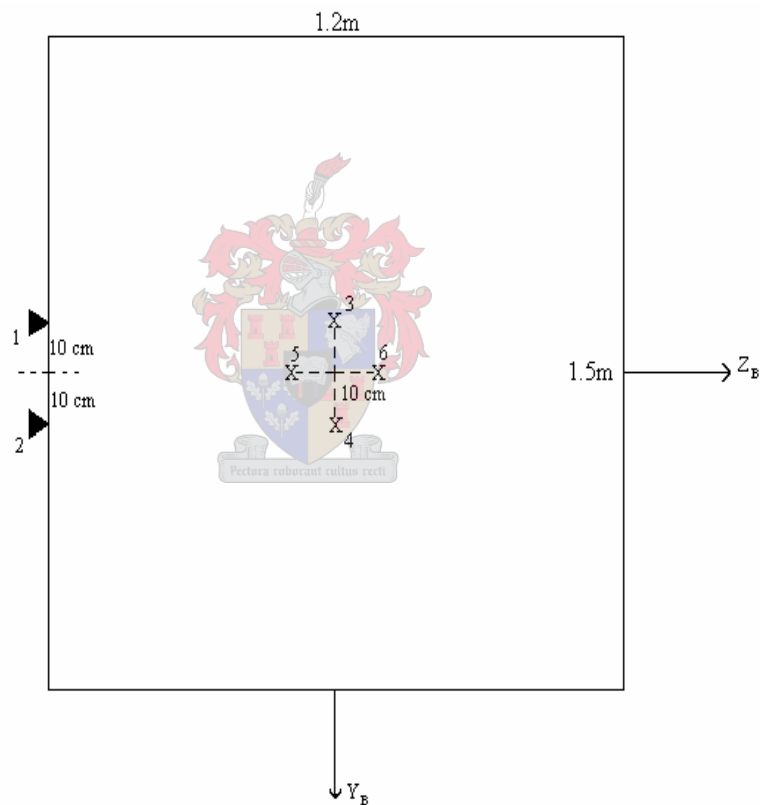
Figure 5.6 LPT displacement from centre of mass

Only LPTs are used in this control algorithm since fine attitude control requires torques of very small magnitude. The LPTs are placed such that they provide reaction torques and not forces to the associated body axis. The LPTs used to control the respective body axis is discussed in Table 4.1. The arrangement of the LPTs with

respect to the centre of mass of the satellite is shown in Figure 5.6. LPTs are also used for orbit control operations which are discussed in Chapter 7.

Note: The thruster arrangement in Figure 4.3 depicts the facet on which each thruster is mounted while Figure 5.6 emphasises on the displacement of the LPTs from the centre of mass of the satellite. The HPT is not shown because it is not used in fine attitude control and is not deliberately displaced from the centre of mass.

The pulsing technique used is a PWPF (Pulse Width Pulse Frequency) method which is implemented in Sidi 1997. However the analysis is repeated and explained for the convenience of the reader. Pulsing of thrusters is done by a Schmidt trigger which has a dead-zone incorporated in it. The idea behind using a dead-zone is to avoid unnecessary pulsing of the thrusters due to sensor noise. Also a time constant network is used prior to the hysteresis block to control the thruster firing frequency. The most important task in this analysis is to relate the error in attitude to the on and off pulse periods. Figure 5.7 shows the PWPF block diagram. A torque is generated only when the Schmitt trigger is activated. Once the trigger is activated a positive or negative pulse is generated thereby producing a torque. For periods when the trigger is not pulsed the satellite will drift as if it was in an open loop.
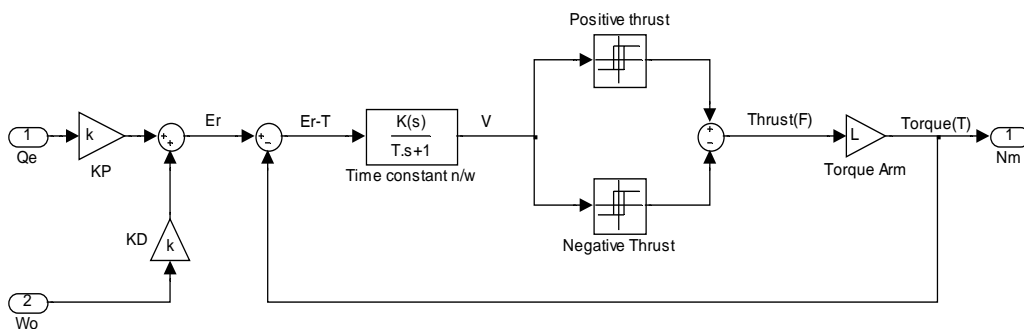
Figure 5.7 Thruster pulsing using PWPF

The proportional and differential gains used are those calculated in Section 5.1.2. The time behaviour of the output (*V*) of the time-constant network can be written in terms of its input ($Er - T$) as,

$$\dot{V}\tau + V = K(Er - T) \tag{5.46}$$

Performing Laplace transform for a constant step command we get,

$$V(s) = \frac{\tau V(0)}{1+\tau s} + \frac{K(Er-T)}{s(1+\tau s)} \tag{5.47}$$

The time domain solution of Equation (5.47) is,

$$V(t) = V(0)e^{-t/\tau} + K(Er-T)[1-e^{-t/\tau}] \tag{5.48}$$

Levels at which the trigger switches on and off are V_{ON} and V_{OFF} respectively and the on and off pulse periods are denoted as t_{ON} and t_{OFF}. The output of the Schmitt trigger when active is $F = 1$ Newton. When the trigger is activated, $V(0) = V_{ON}$ which decreases asymptotically to $K(Er\text{-}T)$. The decrease is stopped when $V(t) = V_{OFF}$. Hence Equation (5.48) can be re-written as,

$$V_{OFF} = V_{ON}\,e^{-t_{ON}/\tau} + K(Er-T)[1-e^{-t_{ON}/\tau}] \tag{5.49}$$

Equation (5.49) can be rearranged as,

$$e^{-t_{ON}/\tau} = \frac{V_{OFF} - KEr + KT}{V_{ON} - KEr + KT} = 1 - \frac{V_{ON} - V_{OFF}}{V_{ON} - KEr + KT} \tag{5.50}$$

For a small value of t_{ON}, $e^{-t_{ON}/\tau} \approx 1-(t_{ON}/\tau)$, which gives the approximation,

$$t_{ON} \approx \tau \frac{V_{ON} - V_{OFF}}{V_{ON} - KEr + KT} \tag{5.51}$$

A similar analysis is preformed to calculate the trigger off period. Initially when the trigger is off $V(0) = V_{OFF}$ and starts to progress to $K(Er\text{-}T)$. Since the trigger is off, $T = 0$ which gives $(K(Er\text{-}T) = KEr)$. The trigger is then switched on at $V(t) = V_{ON}$. Substitution of these terms into Equation (5.48) gives,

$$V_{ON} = V_{OFF}\,e^{-t_{OFF}/\tau} + KEr[1-e^{-t_{OFF}/\tau}] \tag{5.52}$$

Equation (5.52) can be rearranged as,

$$e^{-t_{OFF}/\tau} = \frac{V_{ON} - KEr}{V_{OFF} - KEr} = 1 - \frac{V_{ON} - V_{OFF}}{KEr - V_{OFF}} \tag{5.53}$$

For a small value of t_{OFF}, $e^{-t_{OFF}/\tau} \approx 1 - (t_{OFF}/\tau)$, which gives the approximation,

$$t_{OFF} \approx \tau \frac{V_{ON} - V_{OFF}}{KEr - V_{OFF}} \tag{5.54}$$

The Equations (5.49), (5.51), (5.52) and (5.54) are better understood with help of the figure below.
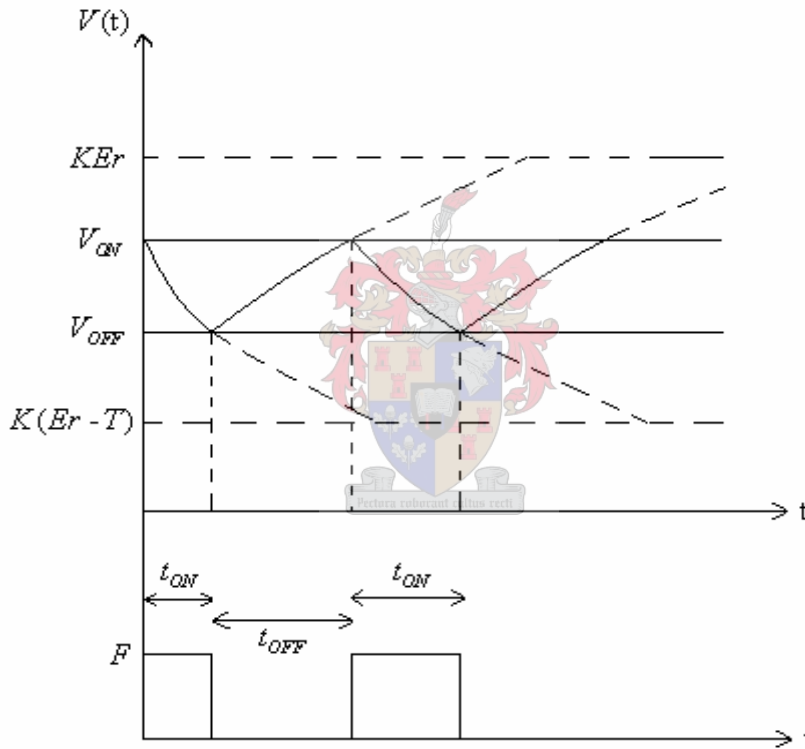
Figure 5.8 Thruster pulsing diagram

The value of $T = 0.1$ Nm because the torque arm $L = 10$ cm. These values are in accordance to Figure 5.6. V_{ON} and V_{OFF} were chosen to be 0.009 and 0.001 Nm respectively. The reason for choosing very small values is to keep the thruster pulses as short as possible in order to save propellant. The only time varying parameter in Equations (5.51) and (5.54) is the term Er which is the error in attitude. The time constant network parameters are chosen through fine tuning. Since the torque output is a very small value (0.1 Nm) in this case, a large value of K is required or else the

trigger will not switch on which will cause the error to grow to a large value. The time constant τ also plays a part in the frequency of thruster firings. Care must be taken to prevent sensor noise amplification while choosing K. Analysis of Equations (5.51) and (5.54) shows that the pulse periods will be longer when Er is large and this happens as soon as the reference input is applied. Also the frequency of pulse firings will be higher. As the error decreases and the attitude reaches the reference value the pulse periods become constant and the pulse frequency also decreases.

This phenomenon can be clearly seen in Figure 5.9. When the error between the measured attitude and reference attitude is large the thrusters are fired frequently but once the reference attitude is reached the pulses are a lot less frequent. After the satellite has reached the reference value the presence of external disturbances will cause drift. The thrusters are fired again to correct this drift.
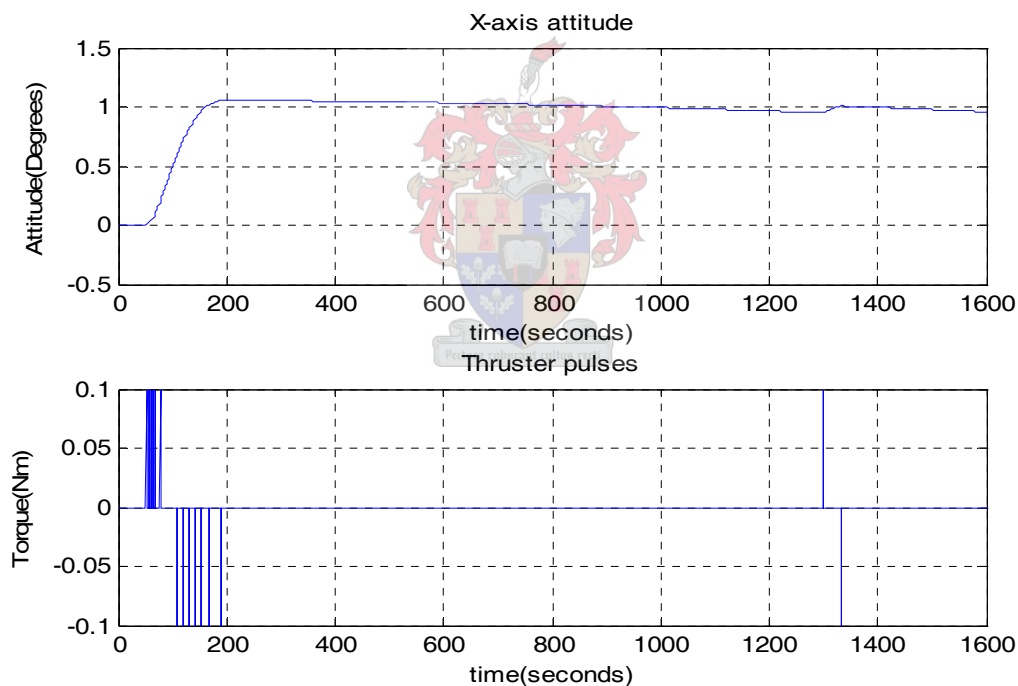
Figure 5.9 Thruster attitude control for X-axis (reference of $1°$)

When the satellite is maintained in its nominal position the only factor that affects the attitude will be the external disturbances. The thruster gets fired once the trigger is activated. Figure 5.10 shows thruster control at nominal attitude. It can be seen that the thrusters firing frequency is very low thereby minimising the propellant

consumption. The exact control algorithm is applied to the Y and Z-axis with their respective proportional and derivative control gains.

It is very important to have a sampling period which is shorter than the on pulse period or else the minimum on pulse period will be equal to the sampling period
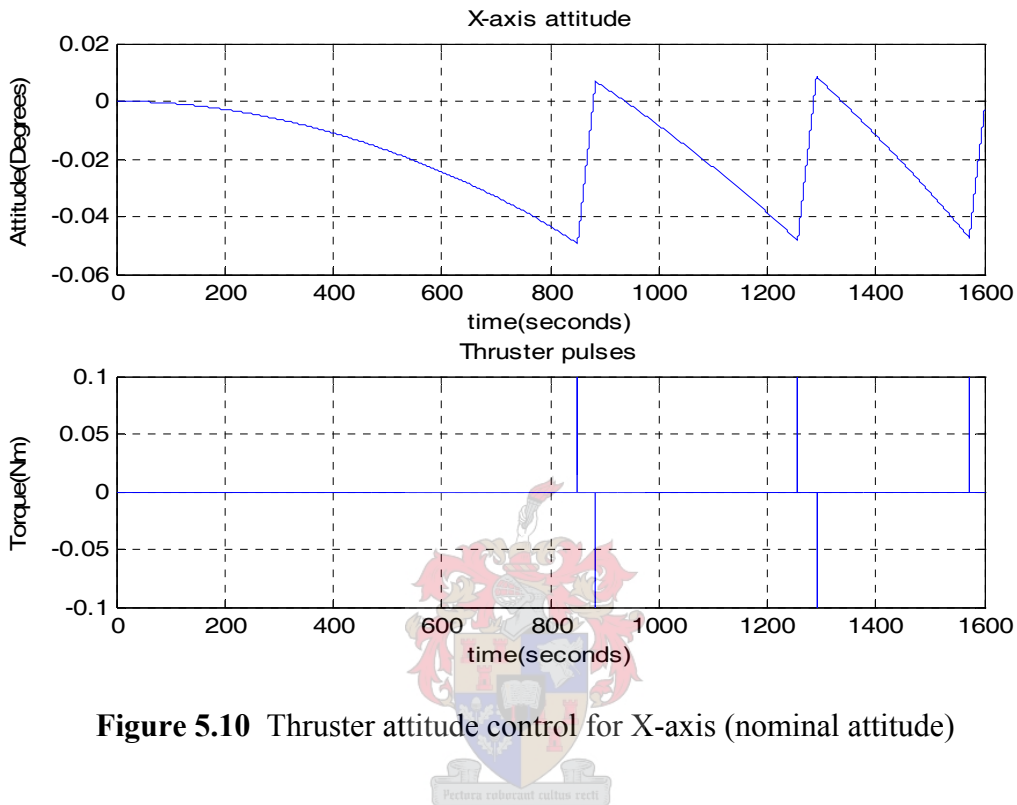
Figure 5.10 Thruster attitude control for X-axis (nominal attitude)

5.5 Summary

The choice of control algorithms depends on the accuracy and speed required. Also the accuracy and speed is determined by the type of actuator combination used in the control technique. The three axis quaternion based reaction wheel controller is the most preferred and commonly used controller because of the linearity and accuracy it provides. Magnetic controllers perform the very important task of momentum dumping. Three axis momentum biased controllers provide necessary back up in the event of reaction wheel failure which is highly possible for a GEO mission and the feature of gyroscopic stability adds to its merits. Though the accuracy is lesser in this case it is still within the necessary limits required for the mission. Finally three axis thruster attitude control in spite of the non-linearity involved finds preference when large control torques and fast control is required.

Chapter 6

Attitude Determination

Attitude determination (estimation) is used to convert raw sensor data to a form that can be used in the control algorithms. Attitude determination is also used to estimate parameters which cannot be measured directly from the sensors. The two estimation techniques that are discussed in this chapter are,

- Full state (attitude plus angular rate) EKF
- FOG bias plus attitude EKF

It so happens that sensors might be used sparingly in order to prolong the sensor life during which the associated sensor data will have to be estimated. The fact that the feedback control algorithms use the estimated or determined parameters signifies the importance of estimation techniques.

6.1 Full state EKF

The full state EKF uses sensor measurements from the magnetometer and the FSS/ES. It is not possible to perform full state estimation using the magnetometer alone because the magnetic field is almost constant for a GEO satellite. Attitude estimation with reduced accuracy ($\pm 1°$) is possible on LEO satellites because of a constantly changing magnetic field which provides three axis information.

Full state estimation can be done over an entire orbit by using a magnetometer along with an ES. This is not possible while using a magnetometer and a FSS as there are no FSS measurements during eclipse. Another possible option would be to use the magnetometer/FSS combination during the non-eclipse period and to switch over to the magnetometer/ES combination during eclipse. If a single FSS is being used on board, the FSS can be used only while the Sun is in the FOV of the sensor. Thus it can be said that the magnetometer/ES combination is the most ideal sensor combination for full state estimation. A similar EKF is discussed in Steyn (1995) which includes an estimate of a constant aerodynamic disturbance torque. The torque is neglected in this case for reasons discussed in Section 3.6.1.

The state vector (7 elements) to be estimated includes the inertial angular rates and the attitude in terms of the quaternions. The full state vector can be represented as,

$$\mathbf{x} = \begin{bmatrix} \boldsymbol{\omega}^I_B \\ \mathbf{q} \end{bmatrix} \tag{6.1}$$

System Model:

The reason for using an EKF is because of the non-linearity in the satellite dynamics and kinematics. Non-linearity in the dynamics and kinematics can be seen in Equations (2.8) and (2.9) respectively. The time-varying non-linear state vector is represented as,

$$\dot{\mathbf{x}}(t) = \mathbf{f}\{\mathbf{x}(t),t\} + \mathbf{s}(t) \tag{6.2}$$

where,

$$\mathbf{s}(t) = N\{\mathbf{0},\mathbf{Q}(t)\} \tag{6.3}$$

$\mathbf{s}(t)$ is the Gaussian system noise with zero mean and a covariance matrix $\mathbf{Q}$. The system noise is dependant on the characteristics of the plant.

The state perturbation is the difference between the real state and the estimated state and is denoted as,

$$\boldsymbol{\delta}\mathbf{x}(t) = \mathbf{x}(t) - \hat{\mathbf{x}}(t) \tag{6.4}$$

The first order Taylor series expansion of the non-linear function in Equation (6.2) is,

$$\mathbf{f}\{\mathbf{x}(t),t\} \approx \mathbf{f}\{\hat{\mathbf{x}}(t),t\} + \frac{\partial \mathbf{f}}{\partial \mathbf{x}}\bigg|_{\mathbf{x}=\hat{\mathbf{x}}} \boldsymbol{\delta}\mathbf{x}(t) \tag{6.5}$$

where we define,

$$\mathbf{F}\{\hat{\mathbf{x}}(t),t\} = \frac{\partial \mathbf{f}}{\partial \mathbf{x}}\bigg|_{\mathbf{x}=\hat{\mathbf{x}}}$$

Differentiating Equation (6.4) we get,

$$\boldsymbol{\delta}\dot{\mathbf{x}}(t) = \dot{\mathbf{x}}(t) - \dot{\hat{\mathbf{x}}}(t) \tag{6.6}$$

By substituting Equation (6.2) in Equation (6.6) it can be seen that,

$$\delta\ddot{\mathbf{x}}(t) = \mathbf{f}\{\mathbf{x}(t),t\} + \mathbf{s}(t) - \dot{\hat{\mathbf{x}}}(t) \tag{6.7}$$

Eventually substituting Equation (6.5) in Equation (6.7) we reach the relation,

$$\delta\dot{\mathbf{x}}(t) = \mathbf{f}\{\hat{\mathbf{x}}(t),t\} + \mathbf{F}\{\hat{\mathbf{x}}(t),t\}\delta\mathbf{x}(t) + \mathbf{s}(t) - \dot{\hat{\mathbf{x}}}(t) \tag{6.8}$$

where, $\dot{\hat{\mathbf{x}}}(t) = \mathbf{f}\{\hat{\mathbf{x}}(t),t\}$.

Therefore the linearised state perturbation equation can be expressed as,

$$\delta\dot{\mathbf{x}}(t) = \mathbf{F}\{\hat{\mathbf{x}}(t),t\}\delta\mathbf{x}(t) + \mathbf{s}(t) \tag{6.9}$$

The continuous state perturbation model needs to be a discretised so as to enable onboard implementation which uses a discrete EKF. The linearised discrete state perturbation is expressed as,

$$\delta\mathbf{x}_{k+1} = \exp[\mathbf{F}\{\hat{\mathbf{x}}(t_k),t_k\}T_s]\delta\mathbf{x}_k = \boldsymbol{\Phi}_k\delta\mathbf{x}_k \tag{6.10}$$

where,

$\boldsymbol{\Phi}_k = \exp[\mathbf{F}\{\hat{\mathbf{x}}(t_k),t_k\}T_s]$ for a short sampling interval T_s .

$\boldsymbol{\Phi}_k$ can be approximated using a first order Taylor series expansion which is,

$$\boldsymbol{\Phi}_k \approx \mathbf{I} + [\mathbf{F}\{\hat{\mathbf{x}}(t_k),t_k\}T_s] \tag{6.11}$$

A second (or higher) order Taylor series was avoided because it does not make any significant difference which improves the performance of the filter.

6.1.1 Computation of State (System) matrix F

The linearised perturbation state matrix $\mathbf{F}\{\hat{\mathbf{x}}(t_k),t_k\}$ is obtained by partially differentiating the dynamics (Equation (2.8)) and kinematics (Equation (2.9)) with respect to the state vector (Equation (6.1)).

$\mathbf{F}\{\hat{\mathbf{x}}(t_k),t_k\}$ is expressed in the matrix form as,

$$\mathbf{F}\{\hat{\mathbf{x}}(t_k),t_k\} = \begin{bmatrix} \dfrac{\partial\dot{\boldsymbol{\omega}}_B^I}{\partial\boldsymbol{\omega}_B^I} & \dfrac{\partial\dot{\boldsymbol{\omega}}_B^I}{\partial\mathbf{q}} \\ \dfrac{\partial\dot{\mathbf{q}}}{\partial\boldsymbol{\omega}_B^I} & \dfrac{\partial\dot{\mathbf{q}}}{\partial\mathbf{q}} \end{bmatrix} \tag{6.12}$$

The term $\dfrac{\partial \dot{\boldsymbol{\omega}}^I_B}{\partial \boldsymbol{\omega}^I_B}$ is obtained by partially differentiating each element of Equation

(A.11) by the inertial body rates and is calculated as,

$$\frac{\partial \dot{\boldsymbol{\omega}}^I_B}{\partial \boldsymbol{\omega}^I_B} = \begin{bmatrix} 0 & \dfrac{\hat{\omega}_{iz}(I_{YY} - I_{ZZ}) - h_{wz}}{I_{XX}} & \dfrac{\hat{\omega}_{iy}(I_{YY} - I_{ZZ}) + h_{wy}}{I_{XX}} \\[3mm] \dfrac{\hat{\omega}_{iz}(I_{ZZ} - I_{XX}) + h_{wz}}{I_{YY}} & 0 & \dfrac{\hat{\omega}_{ix}(I_{ZZ} - I_{XX}) - h_{wx}}{I_{YY}} \\[3mm] \dfrac{\hat{\omega}_{iy}(I_{XX} - I_{YY}) - h_{wy}}{I_{ZZ}} & \dfrac{\hat{\omega}_{ix}(I_{XX} - I_{YY}) + h_{wx}}{I_{ZZ}} & 0 \end{bmatrix} \quad (6.13)$$

$\dfrac{\partial \dot{\boldsymbol{\omega}}^I_B}{\partial \mathbf{q}}$ is calculated by partially differentiating Equation (A.11) by each quaternion

component. This happens to be a [3 x 4] zero matrix because the dynamic equations
does not contain any term that is expressed in terms of the quaternion.

$$\frac{\partial \dot{\boldsymbol{\omega}}^I_B}{\partial \mathbf{q}} = [\mathbf{0}]_{3\times 4} \qquad (6.14)$$

From Equation (2.11) we can see that,

$$\boldsymbol{\omega}^O_B = \boldsymbol{\omega}^I_B - \mathbf{A}\boldsymbol{\omega_o} \qquad (6.15)$$

where,

$$\boldsymbol{\omega_o} = \begin{bmatrix} 0 \\ -\omega_o \\ 0 \end{bmatrix} \text{ for a GEO satellite.}$$

Since, $\boldsymbol{\omega_o} \ \Box \ \boldsymbol{\omega}^O_B$ and $\boldsymbol{\omega}^I_B$ during attitude manoeuvres for a GEO satellite we can make

the assumption that $\boldsymbol{\omega}^O_B \approx \boldsymbol{\omega}^I_B$ for the following two equations.

$\dfrac{\partial \dot{\mathbf{q}}}{\partial \boldsymbol{\omega}^I_B}$ is calculated by partially differentiating Equation (2.9) with respect to the

inertial body rates and gets expressed as,

$$\frac{\partial \dot{\mathbf{q}}}{\partial \boldsymbol{\omega}^I_B} = \frac{1}{2}\begin{bmatrix} \hat{q}_4 & -\hat{q}_3 & \hat{q}_2 \\ \hat{q}_3 & \hat{q}_4 & -\hat{q}_1 \\ -\hat{q}_2 & \hat{q}_1 & \hat{q}_4 \\ -\hat{q}_1 & -\hat{q}_2 & -\hat{q}_3 \end{bmatrix} \qquad (6.16)$$

Finally $\dfrac{\partial \dot{\mathbf{q}}}{\partial \mathbf{q}}$ is obtained by partially differentiating Equation (2.9) with respect to individual quaternion components.

$$\frac{\partial \dot{\mathbf{q}}}{\partial \mathbf{q}} = \frac{1}{2}\begin{bmatrix} 0 & \hat{\omega}_{oz} & -\hat{\omega}_{oy} & \hat{\omega}_{ox} \\ -\hat{\omega}_{oz} & 0 & \hat{\omega}_{ox} & \hat{\omega}_{oy} \\ \hat{\omega}_{oy} & -\hat{\omega}_{ox} & 0 & \hat{\omega}_{oz} \\ -\hat{\omega}_{ox} & -\hat{\omega}_{oy} & -\hat{\omega}_{oz} & 0 \end{bmatrix} \tag{6.17}$$

The terms (6.13) to (6.17) are substituted into Equation (6.12) and then discretised using Equation (6.11). It can be seen that $\mathbf{F}\{\hat{\mathbf{x}}(t_k), t_k\}$ is a [7 x 7] matrix, which makes $\mathbf{\Phi}_k$ a [7 x 7] matrix as well.

Measurement Model:

The discrete non-linear measurement model of the EKF is generally expressed as,

$$\mathbf{y}_k = \mathbf{h}_k\{\mathbf{x}(t_k), t_k\} + \mathbf{m}_k \tag{6.18}$$

where,

$$\mathbf{m}_k = N\{\mathbf{0}, \mathbf{R}_k\} \tag{6.19}$$

$\mathbf{m}_k$ is the Gaussian measurement noise with zero mean and a covariance matrix $\mathbf{R}$. The measurement noise is dependent on the sensor characteristics.

The first order Taylor series expansion for the non-linear function in Equation (6.18) is given as,

$$\mathbf{h}_k\{\mathbf{x}(t_k), t_k\} \approx \mathbf{h}_k\{\hat{\mathbf{x}}(t_k), t_k\} + \left.\frac{\partial \mathbf{h}}{\partial \mathbf{x}}\right|_{\mathbf{x}=\hat{\mathbf{x}}} \delta\mathbf{x}_k \tag{6.20}$$

where we define,

$$\mathbf{H}_k(\hat{\mathbf{x}}_k) = \left.\frac{\partial \mathbf{h}}{\partial \mathbf{x}}\right|_{\mathbf{x}=\hat{\mathbf{x}}}$$

The innovation (error) term is difference between the real output and the estimated output which is expressed as,

$$\mathbf{e}_k = \mathbf{y}_k - \hat{\mathbf{y}}_k \tag{6.21}$$

By substituting Equation (6.20) into Equation (6.18) we get,

$$\mathbf{y}_k = \mathbf{h}_k \{\hat{\mathbf{x}}(t_k), t_k\} + \mathbf{H}_k(\hat{\mathbf{x}}_k)\boldsymbol{\delta}\mathbf{x}_k + \mathbf{m}_k \tag{6.22}$$

Finally by substituting Equation (6.22) into Equation (6.21) it can be seen that,

$$\mathbf{e}_k = \mathbf{h}_k \{\hat{\mathbf{x}}(t_k), t_k\} + \mathbf{H}_k(\hat{\mathbf{x}}_k)\boldsymbol{\delta}\mathbf{x}_k + \mathbf{m}_k - \hat{\mathbf{y}}_k \tag{6.23}$$

where, $\hat{\mathbf{y}}_k = \mathbf{h}_k \{\hat{\mathbf{x}}(t_k), t_k\}$.

Therefore the linearised innovation model is,

$$\mathbf{e}_k = \mathbf{H}_k(\hat{\mathbf{x}}_k)\boldsymbol{\delta}\mathbf{x}_k + \mathbf{m}_k \tag{6.24}$$

6.1.2 Computation of Output (Measurement) matrix H

The computation of the output matrix for a model which includes a constant aerodynamic torque is performed in Steyn (1995) and Engelbrecht (1999). However, since the torque is not included in this case the output matrix will be slightly simpler and different. The innovation vector is considered as the vector difference between a measured normalised vector $\mathbf{v}_{meas}$ in body coordinates and a modelled normalised vector $\hat{\mathbf{v}}_{body}$ in body coordinates. The $\hat{\mathbf{v}}_{body}$ vector is obtained by transforming the modelled vector $\mathbf{v}_{orb}$ in orbit coordinates to body coordinates using the estimated DCM matrix $\mathbf{A}(\mathbf{q}_k)$.

In an ideal world we would have a situation where there are no errors in measurement and modelling. Then,

$$\mathbf{v}_{meas,k}^{ideal} = \mathbf{A}(\mathbf{q}_k)\mathbf{v}_{orb,k}^{ideal} \tag{6.25}$$

But unfortunately in the real world we have errors that occur due to improper measurement and modelling where the transformation is done using the estimated quaternions. Equation (6.25) thus becomes,

$$\mathbf{v}_{meas,k} - \mathbf{m}_{meas,k} = [\mathbf{A}(\hat{\mathbf{q}}_k + \boldsymbol{\delta}\mathbf{q}_k)](\mathbf{v}_{orb,k} - \mathbf{m}_{orb,k}) \tag{6.26}$$

where, $\mathbf{m}_{meas,k}$ and $\mathbf{m}_{orb,k}$ are the measurement and modelling errors respectively.

Before proceeding further it is essential to mention that the innovation can also be represented as,

$$\mathbf{e}_k = \mathbf{v}_{meas,k} - \mathbf{A}(\hat{\mathbf{q}}_k)\mathbf{v}_{orb,k} \qquad (6.27)$$

A first order Taylor series expansion for the DCM in Equation (6.26) is,

$$\mathbf{A}(\hat{\mathbf{q}}_k + \delta\mathbf{q}_k) \approx \mathbf{A}(\hat{\mathbf{q}}_k) + \sum_{i=1}^{4} \frac{\delta\mathbf{A}(\hat{\mathbf{q}}_k)}{\delta q_{i,k}}\delta q_{i,k} \qquad (6.28)$$

Substituting Equation (6.28) into Equation (6.26) we get,

$$\mathbf{v}_{meas,k} - \mathbf{m}_{meas,k} = \left[\mathbf{A}(\hat{\mathbf{q}}_k) + \sum_{i=1}^{4} \frac{\delta\mathbf{A}(\hat{\mathbf{q}}_k)}{\delta q_{i,k}}\delta q_{i,k}\right](\mathbf{v}_{orb,k} - \mathbf{m}_{orb,k}) \qquad (6.29)$$

By ignoring the small higher order noise terms and with the assumption that $\mathbf{m}_k \approx \mathbf{m}_{meas,k} - \mathbf{A}(\hat{\mathbf{q}}_k)\mathbf{m}_{orb,k}$, Equation (6.29) gets modified to

$$\mathbf{v}_{meas,k} - \mathbf{A}(\hat{\mathbf{q}}_k)\mathbf{v}_{orb,k} = \left[\sum_{i=1}^{4} \frac{\delta\mathbf{A}(\hat{\mathbf{q}}_k)}{\delta q_{i,k}}\delta q_{i,k}\right]\mathbf{v}_{orb,k} + \mathbf{m}_k \qquad (6.30)$$

By comparing Equations (6.27) and (6.30) it can be seen that,

$$\mathbf{e}_k = \left[\sum_{i=1}^{4} \frac{\delta\mathbf{A}(\hat{\mathbf{q}}_k)}{\delta q_{i,k}}\delta q_{i,k}\right]\mathbf{v}_{orb,k} + \mathbf{m}_k \qquad (6.31)$$

$$= \left[\sum_{i=1}^{4} \frac{\delta\mathbf{A}(\hat{\mathbf{q}}_k)}{\delta q_{i,k}}\mathbf{v}_{orb,k}\right]\delta\mathbf{q}_k + \mathbf{m}_k$$

$$= [\mathbf{h}_1 \quad \mathbf{h}_2 \quad \mathbf{h}_3 \quad \mathbf{h}_4]\delta\mathbf{q}_k + \mathbf{m}_k$$

$$= [\mathbf{0}_{3x3} \quad \mathbf{h}_1 \quad \mathbf{h}_2 \quad \mathbf{h}_3 \quad \mathbf{h}_4]\delta\mathbf{x}_k + \mathbf{m}_k$$

$$\mathbf{e}_k = [\mathbf{H}_k(\hat{\mathbf{q}}_k)\mathbf{v}_{orb,k}]\delta\mathbf{x}_k + \mathbf{m}_k \qquad (6.32)$$

Comparison of Equations (6.24) and (6.32) shows that the output matrix $\mathbf{H}$ to be,

$$\mathbf{H}_k(\hat{\mathbf{x}}_k) = \mathbf{H}_k(\hat{\mathbf{q}}_k)\mathbf{v}_{orb,k} = [\mathbf{0}_{3x3} \quad \mathbf{h}_1 \quad \mathbf{h}_2 \quad \mathbf{h}_3 \quad \mathbf{h}_4] \qquad (6.33)$$

where,

$$\mathbf{h}_i = \frac{\delta\mathbf{A}(\hat{\mathbf{q}}_k)}{\delta q_{i,k}}\mathbf{v}_{orb,k} \quad , \quad i = 1,2,3,4 \qquad (6.34)$$

Equation (6.34) is obtained by partially differentiating the estimated DCM by each quaternion component and is determined to be,

$$\mathbf{h}_1 = \frac{\delta\mathbf{A}(\hat{\mathbf{q}}_k)}{\delta q_{1,k}} = 2\begin{bmatrix} \hat{q}_{1,k} & \hat{q}_{2,k} & \hat{q}_{3,k} \\ \hat{q}_{2,k} & -\hat{q}_{1,k} & \hat{q}_{4,k} \\ \hat{q}_{3,k} & -\hat{q}_{4,k} & -\hat{q}_{1,k} \end{bmatrix}\mathbf{v}_{orb,k} \ ; \ \mathbf{h}_2 = \frac{\delta\mathbf{A}(\hat{\mathbf{q}}_k)}{\delta q_{2,k}} = 2\begin{bmatrix} -\hat{q}_{2,k} & \hat{q}_{1,k} & -\hat{q}_{4,k} \\ \hat{q}_{1,k} & \hat{q}_{2,k} & \hat{q}_{3,k} \\ \hat{q}_{4,k} & \hat{q}_{3,k} & -\hat{q}_{2,k} \end{bmatrix}\mathbf{v}_{orb,k}$$

$$\mathbf{h}_3 = \frac{\delta\mathbf{A}(\hat{\mathbf{q}}_k)}{\delta q_{3,k}} = 2\begin{bmatrix} -\hat{q}_{3,k} & \hat{q}_{4,k} & \hat{q}_{1,k} \\ -\hat{q}_{4,k} & -\hat{q}_{3,k} & \hat{q}_{2,k} \\ \hat{q}_{1,k} & -\hat{q}_{2,k} & -\hat{q}_{3,k} \end{bmatrix}\mathbf{v}_{orb,k} \ ; \ \mathbf{h}_4 = \frac{\delta\mathbf{A}(\hat{\mathbf{q}}_k)}{\delta q_{4,k}} = 2\begin{bmatrix} \hat{q}_{4,k} & \hat{q}_{3,k} & -\hat{q}_{2,k} \\ -\hat{q}_{3,k} & \hat{q}_{4,k} & \hat{q}_{1,k} \\ \hat{q}_{2,k} & -\hat{q}_{1,k} & \hat{q}_{4,k} \end{bmatrix}\mathbf{v}_{orb,k}$$

EKF Algorithm:

The EKF algorithm is discussed in Steyn (1995) as well as Engelbrecht (1999). It is repeated in order to preserve continuity in literature. First and foremost the perturbation covariance matrix is defined as,

$$\mathbf{P}_k = E\{\boldsymbol{\delta}\mathbf{x}_k.\boldsymbol{\delta}\mathbf{x}_k^T\}$$

which is the expectation of the state perturbation vector multiplied by its transpose.

The steps involved in the computation of the EKF algorithm are as follows:

Between Measurements:

1) Propagate the dynamic (Equation (2.8)) and kinematic (Equation (2.9)) equations of motion using numerical integration.

$$\hat{\mathbf{x}}_{k+1/k} = \hat{\mathbf{x}}_{k/k} + \int_k^{k+1} \mathbf{f}(\hat{\mathbf{x}}_{k/k},k)dt \qquad (6.35)$$

2) Compute the linearised perturbation state matrix, $\mathbf{F}\{\hat{\mathbf{x}}(t_{k+1}),t_{k+1}\}$.

$$\mathbf{F}\{\hat{\mathbf{x}}(t_{k+1}),t_{k+1}\} = \frac{\partial\mathbf{f}}{\partial\mathbf{x}}\bigg|_{\mathbf{x}=\hat{\mathbf{x}}_{k+1/k}} \qquad (6.36)$$

3) Obtain the discrete system matrix, $\boldsymbol{\Phi}_{k+1/k}$.

$$\boldsymbol{\Phi}_{k+1/k} \approx \mathbf{I} + [\mathbf{F}\{\hat{\mathbf{x}}(t_{k+1/k}),t_{k+1}\}T_s] \qquad (6.37)$$

4) Propagate the perturbation covariance matrix, $\mathbf{P}_{k+1/k}$.

$$\mathbf{P}_{k+1/k} = \boldsymbol{\Phi}_{k+1/k}\mathbf{P}_{k/k}\boldsymbol{\Phi}_{k+1/k}^T + \mathbf{Q} \qquad (6.38)$$

Across Measurements:

1) Compute the Kalman filter gain, $\mathbf{K}_{k+1}$ using the discrete output matrix $\mathbf{H}_{k+1/k}$ from Equation (6.33)

$$\mathbf{K}_{k+1} = \mathbf{P}_{k+1/k}\mathbf{H}_{k+1/k}^{T}[\mathbf{H}_{k+1/k}\mathbf{P}_{k+1/k}\mathbf{H}_{k+1/k}^{T} + \mathbf{R}]^{-1} \tag{6.39}$$

2) Calculate the innovation vector, $\mathbf{e}_{k+1}$.

$$\mathbf{e}_{k+1} = \mathbf{v}_{meas,k+1} - \mathbf{A}(\hat{\mathbf{q}}_{k+1/k})\mathbf{v}_{orb,k+1} \tag{6.40}$$

3) Update the state vector using the innovation.

$$\hat{\mathbf{x}}_{k+1/k+1} = \hat{\mathbf{x}}_{k+1/k} + \mathbf{K}_{k+1}\mathbf{e}_{k+1} \tag{6.41}$$

The quaternion elements of the updated state vector are normalised to preserve the quaternion constraint by,

$$\hat{\mathbf{q}}_{norm,k+1/k} = \frac{\hat{\mathbf{q}}_{k+1/k+1}}{\left\|\hat{\mathbf{q}}_{k+1/k+1}\right\|}$$

4) Recompute the discrete output matrix, $\mathbf{H}_{k+1/k+1}$ using the updated state, $\hat{\mathbf{x}}_{k+1/k+1}$.

$$\mathbf{H}_{k+1/k+1} = \left.\frac{\partial \mathbf{h}}{\partial \mathbf{x}}\right|_{\mathbf{x}=\hat{\mathbf{x}}_{k+1/k+1}} \tag{6.42}$$

5) Update the perturbation covariance matrix.

$$\mathbf{P}_{k+1/k+1} = [\mathbf{I} - \mathbf{K}_{k+1}\mathbf{H}_{k+1/k+1}]\mathbf{P}_{k+1/k}[\mathbf{I} - \mathbf{K}_{k+1}\mathbf{H}_{k+1/k+1}]^{T} + \mathbf{K}_{k+1}\mathbf{R}\mathbf{K}_{k+1}^{T} \tag{6.43}$$

6.1.3 Results

Figure 6.1 shows the performance of the full state EKF. The EKF was disabled initially when the simulation is performed. The filter was then enabled at 0.25 orbit period at which point the estimates start to track the real attitude. The result shows that the estimates track the actual attitude within the required accuracy levels (Section 2.1). The time taken by the estimates to converge to the actual attitude is less than 45 minutes (0.03 orbit) which is satisfactory.
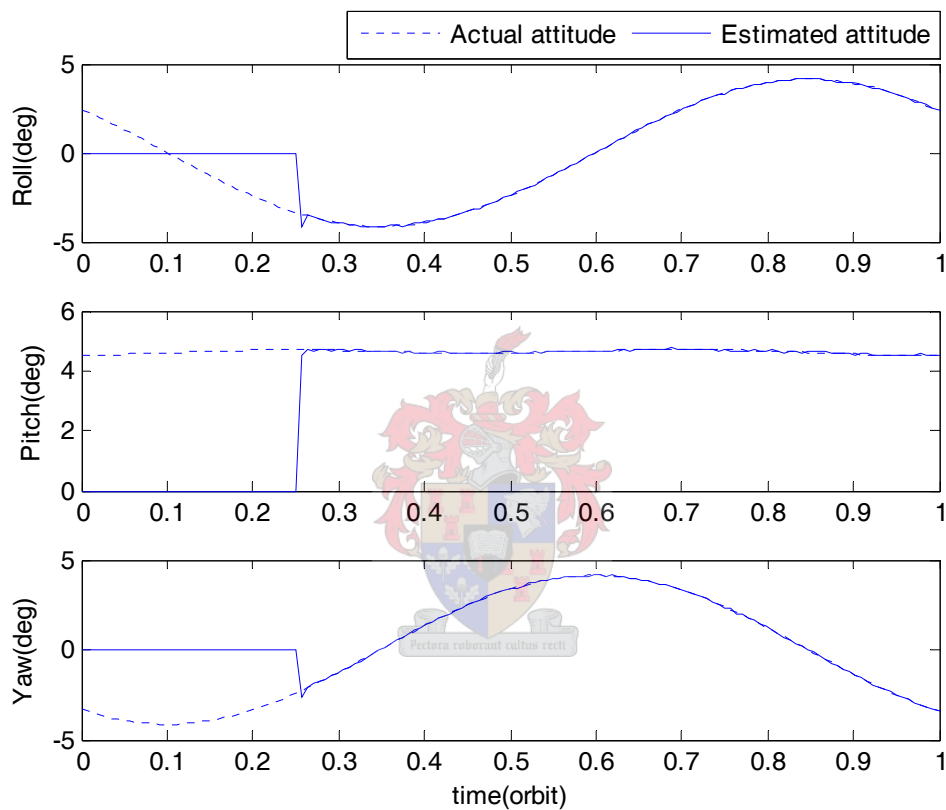
Figure 6.1 Actual attitude versus estimated attitude

The IGRF modelling errors were extrapolated from Table 5.1 in Wertz (1978) and assumed to have a maximum value of 1 nTesla. A uniform distributed noise of 1 nTesla was added to each axis of the modelled IGRF vector to get the measurements. The ES measurement angles were obtained by adding uniform distributed noise of the range $-0.025°$ to $0.025°$ (RMS error of approximately $0.018°$). The FSS measurement angles were added with uniform distributed noise of the range $-0.05°$ to $0.05°$ (RMS error of approximately $0.035°$). The RMS error in the estimated attitude and angular rates is shown in Figure 6.2. The average RMS error

was calculated to be less than $0.04°$ while the error in the angular rate estimates is 2.146×10^{-4} deg/sec.
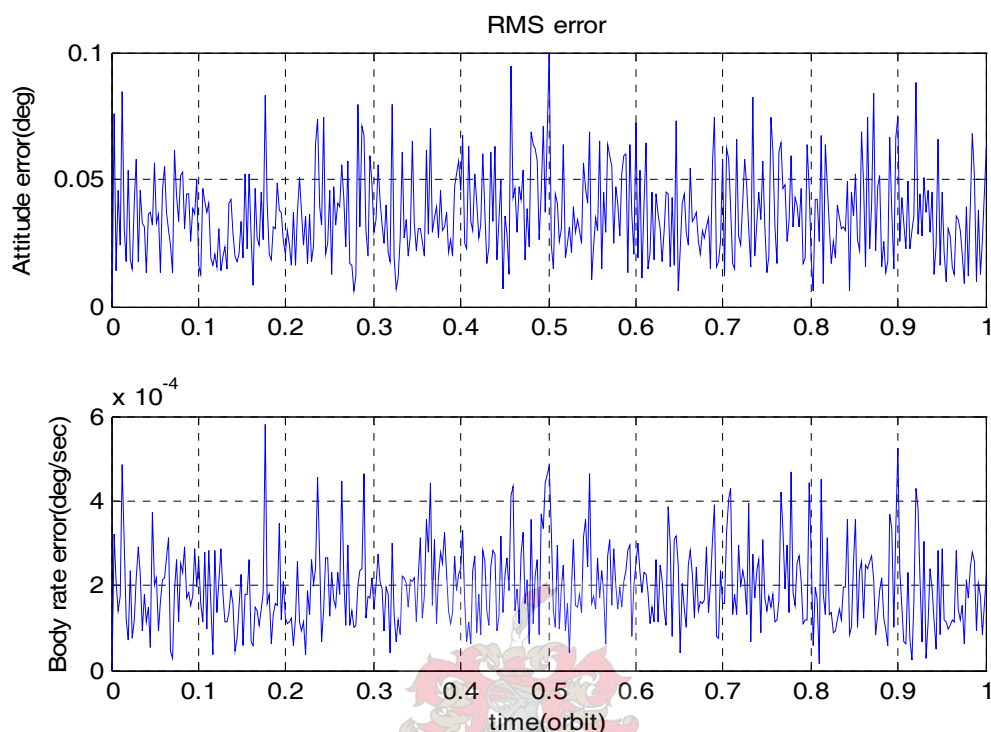
Figure 6.2 RMS error in attitude and body rates

6.2 FOG bias plus attitude estimator

This estimator uses angular rate measurements from the FOGs. The idea behind the estimator was obtained from Lefferts *et.al.* (1982). The sensor combinations used here are similar to that discussed in Section 6.1 except that FOGs are also used. Since the angular rate measurements are directly obtained from the FOGs, the attitude estimate is expected to be more accurate. This estimator is used whenever manoeuvres are performed on the satellite where estimates of the angular rates are not sufficient. The state vector to be estimated is represented as,

$$\mathbf{x} = \begin{bmatrix} \mathbf{q} \\ \mathbf{b} \end{bmatrix} \tag{6.44}$$

where, $\mathbf{q}$ = quaternion attitude

$\mathbf{b}$ = bias vector

The quaternion vector **q** is calculated using quaternion multiplication between the perturbation quaternion and the estimated quaternion and is expressed as (Markley, 2004),

$$\mathbf{q} = \boldsymbol{\delta q} \otimes \hat{\mathbf{q}} \qquad (6.45)$$

where,

$\boldsymbol{\delta q}$ = perturbation quaternion

$\hat{\mathbf{q}}$ = estimated quaternion

The perturbation quaternion is represented as,

$$\boldsymbol{\delta q} = \begin{bmatrix} \boldsymbol{\delta q}_{vec} \\ \delta q_4 \end{bmatrix} \qquad (6.46)$$

where $\delta q_4 = \sqrt{1 - \|\boldsymbol{\delta q}_{vec}\|}$.

Thus the quaternion vector **q** according to the special quaternion multiplication convention (Appendix B), can be shown to be,

$$\mathbf{q} = \begin{bmatrix} \boldsymbol{\delta q}_{vec} \\ \delta q_4 \end{bmatrix} \otimes \hat{\mathbf{q}} = \begin{bmatrix} \delta q_4 & \delta q_3 & -\delta q_2 & \delta q_1 \\ -\delta q_3 & \delta q_4 & \delta q_1 & \delta q_2 \\ \delta q_2 & -\delta q_1 & \delta q_4 & \delta q_3 \\ -\delta q_1 & -\delta q_2 & -\delta q_3 & \delta q_4 \end{bmatrix} \begin{bmatrix} \hat{q}_1 \\ \hat{q}_2 \\ \hat{q}_3 \\ \hat{q}_4 \end{bmatrix} \qquad (6.47)$$

Since the perturbation vector is a vector which contains just three unknowns (the fourth term is a function of the first three terms) the state perturbation vector can be represented as,

$$\boldsymbol{\delta x} = \begin{bmatrix} \boldsymbol{\delta q}_{vec} \\ \Delta \mathbf{b} \end{bmatrix} \qquad (6.48)$$

The system model is similar to that discussed in Section 6.1 as it is a general model for any EKF. It is important to note that the method used in Equation (6.47) often leads to this particular EKF being called the MEKF (Multiplicative Extended Kalman Filter). This terminology can be found in Markley (2004).

6.2.1 Computation of State matrix F

The F matrix computation is based on the discussions in Lefferts *et.al.* (1982) and Bijker (2006). The derivation begins from the differentiation of Equation (6.45) which is,

$$\dot{\mathbf{q}} = \delta\dot{\mathbf{q}} \otimes \hat{\mathbf{q}} + \delta\mathbf{q} \otimes \dot{\hat{\mathbf{q}}} \tag{6.49}$$

The kinematics (Equation (2.10)) of the satellite can also be represented as,

$$\dot{\mathbf{q}} = \frac{1}{2}\boldsymbol{\omega} \otimes \mathbf{q} \tag{6.50}$$

where, $\boldsymbol{\omega}$ has the same components as $\boldsymbol{\omega}_B^O$.

Substituting Equation (6.50) into Equation (6.49) we get the relation,

$$\frac{1}{2}\boldsymbol{\omega} \otimes \mathbf{q} = \delta\dot{\mathbf{q}} \otimes \hat{\mathbf{q}} + \delta\mathbf{q} \otimes \left[\frac{1}{2}\hat{\boldsymbol{\omega}} \otimes \hat{\mathbf{q}}\right] \tag{6.51}$$

Rearranging the above equation gives,

$$\delta\dot{\mathbf{q}} \otimes \hat{\mathbf{q}} = \frac{1}{2}\boldsymbol{\omega} \otimes \mathbf{q} - \delta\mathbf{q} \otimes \left[\frac{1}{2}\hat{\boldsymbol{\omega}} \otimes \hat{\mathbf{q}}\right] \tag{6.52}$$

which is then multiplied by $\hat{\mathbf{q}}^{-1}$ to give,

$$\delta\dot{\mathbf{q}} = \frac{1}{2}\left[\boldsymbol{\omega} \otimes \delta\mathbf{q} - \delta\mathbf{q} \otimes \hat{\boldsymbol{\omega}}\right] \tag{6.53}$$

The measurements of the FOGs are in described in Equation (4.1). The perturbation in the '$\delta\boldsymbol{\omega}$' can be represented as,

$$\begin{bmatrix} \delta\boldsymbol{\omega} \\ 0 \end{bmatrix} = \begin{bmatrix} \boldsymbol{\omega} - \hat{\boldsymbol{\omega}} \\ 0 \end{bmatrix} = \begin{bmatrix} (\boldsymbol{\omega}_B^I + \mathbf{A}\boldsymbol{\omega}_o + \mathbf{b}) - (\boldsymbol{\omega}_B^I + \hat{\mathbf{A}}\boldsymbol{\omega}_o + \hat{\mathbf{b}} + \boldsymbol{\eta}_1) \\ 0 \end{bmatrix}$$
$$\approx \begin{bmatrix} -\Delta\mathbf{b} - \boldsymbol{\eta}_1 \\ 0 \end{bmatrix} \tag{6.54}$$

where, $\mathbf{A}\boldsymbol{\omega}_o - \hat{\mathbf{A}}\boldsymbol{\omega}_o \Box\, 0$ for a GEO orbit.

Equation (6.53) can be written as,

$$\delta\dot{\mathbf{q}} = \frac{1}{2}\left[(\hat{\boldsymbol{\omega}}+\delta\boldsymbol{\omega})\otimes\delta\mathbf{q} - \delta\mathbf{q}\otimes\hat{\boldsymbol{\omega}}\right]$$
$$= \frac{1}{2}\left[(\hat{\boldsymbol{\omega}}\otimes\delta\mathbf{q} - \delta\mathbf{q}\otimes\hat{\boldsymbol{\omega}})\right] + \frac{1}{2}\left[\delta\boldsymbol{\omega}\otimes\delta\mathbf{q}\right]$$

(6.55)

From Lefferts *et.al.* (1982),

$$\frac{1}{2}\left[(\hat{\boldsymbol{\omega}}\otimes\delta\mathbf{q} - \delta\mathbf{q}\otimes\hat{\boldsymbol{\omega}})\right] = \begin{bmatrix} -\hat{\boldsymbol{\omega}}\times\delta\mathbf{q} \\ 0 \end{bmatrix}$$

(6.56)

Substituting Equations (6.54) and (6.56) into Equation (6.55) we get,

$$\delta\dot{\mathbf{q}} = \begin{bmatrix} -\hat{\boldsymbol{\omega}}\times\delta\mathbf{q} \\ 0 \end{bmatrix} + \frac{1}{2}\left[\begin{bmatrix} -\Delta\mathbf{b}-\boldsymbol{\eta}_1 \\ 0 \end{bmatrix}\otimes\delta\mathbf{q}\right]$$

(6.57)

We ignore the last row of Equation (6.57) since only the vector part of the perturbation vector is required. The higher order terms are also ignored which leaves us with,

$$\delta\dot{\mathbf{q}}_{\text{vec}} = -\hat{\boldsymbol{\omega}}\times\delta\mathbf{q}_{\text{vec}} - \frac{1}{2}(\Delta\mathbf{b}+\boldsymbol{\eta}_1)$$

(6.58)

The above equation can be represented in terms of the complete state vector as,

$$\delta\dot{\mathbf{x}} = \mathbf{F}\{\hat{\mathbf{x}}(t_k),t_k\}\delta\mathbf{x} + \mathbf{G}\{\hat{\mathbf{x}}(t_k),t_k\}\mathbf{s}$$

where, $\mathbf{s} = \begin{bmatrix} \boldsymbol{\eta}_1 & \boldsymbol{\eta}_2 \end{bmatrix}^T$ and $\boldsymbol{\eta}_2 =$ FOG bias noise (modelled as $\dot{\mathbf{b}}$).

The $\mathbf{F}\{\hat{\mathbf{x}}(t_k),t_k\}$ and $\mathbf{G}\{\hat{\mathbf{x}}(t_k),t_k\}$ matrices can now be represented as,

$$\mathbf{F}\{\hat{\mathbf{x}}(t_k),t_k\} = \begin{bmatrix} [\hat{\boldsymbol{\omega}}\times]_{3\times3} & -\frac{1}{2}[\mathbf{I}]_{3\times3} \\ [\mathbf{0}]_{3\times3} & [\mathbf{0}]_{3\times3} \end{bmatrix} \text{ and } \mathbf{G}\{\hat{\mathbf{x}}(t_k),t_k\} = \begin{bmatrix} -\frac{1}{2}[\mathbf{I}]_{3\times3} & [\mathbf{0}]_{3\times3} \\ [\mathbf{0}]_{3\times3} & [\mathbf{I}]_{3\times3} \end{bmatrix}$$

Only the $\mathbf{F}\{\hat{\mathbf{x}}(t_k),t_k\}$ matrix is required to compute the discrete matrix '$\boldsymbol{\Phi}_k$' using Equation (6.11). The $\mathbf{G}\{\hat{\mathbf{x}}(t_k),t_k\}$ matrix does not get used anywhere in the EKF propagation or update.

6.2.2 Computation of Output matrix H

The innovation vector has been computed using a method similar to the one discussed in Steyn (1995) which is based on Psiaki *et.al* (1990). The innovation matrix is calculated as the cross product between the normalised measurement vector $\mathbf{v}_{meas}$ and the normalised body vector $\hat{\mathbf{v}}_{body}$. The reason for using a cross-product innovation is to have rapid convergence of the EKF when the initial attitude is some arbitrary large value. An innovation vector which is based on the difference between the measurement vector and body vector is discussed in Bijker (2006), was also found to perform satisfactorily.

$$\mathbf{e}_k = \mathbf{v}_{meas,k} \times \hat{\mathbf{v}}_{body,k} = \mathbf{v}_{meas,k} \times \mathbf{A}(\hat{\mathbf{q}}_k)\mathbf{v}_{orb,k} \tag{6.59}$$

We know that,

$$\mathbf{v}_{meas,k} = \mathbf{A}(\mathbf{q}_k)\mathbf{v}_{orb,k} \tag{6.60}$$

and because $\mathbf{A}(\mathbf{q}_k) = \mathbf{A}(\delta\mathbf{q} \otimes \hat{\mathbf{q}}_k) = \mathbf{A}(\delta\mathbf{q}_k)\mathbf{A}(\hat{\mathbf{q}}_k)$ (from Equation (6.45)), Equation (6.60) with the addition of measurement and modelling noise becomes,

$$\mathbf{v}_{meas,k} - \mathbf{m}_{meas,k} = \mathbf{A}(\delta\mathbf{q}_k)\,\mathbf{A}(\hat{\mathbf{q}}_k)(\mathbf{v}_{orb,k} - \mathbf{m}_{orb,k}) \tag{6.61}$$

Since $\mathbf{v}_{body,k} = \mathbf{A}(\hat{\mathbf{q}}_k)\,\mathbf{v}_{orb,k}$, Equation (6.61) becomes,

$$\mathbf{v}_{meas,k} = \mathbf{A}(\delta\mathbf{q}_k)\mathbf{v}_{body,k} + \tilde{\mathbf{m}}_k \tag{6.62}$$

where, $\tilde{\mathbf{m}}_k = \mathbf{m}_{meas,k} - \mathbf{A}(\hat{\mathbf{q}}_k)\mathbf{m}_{orb,k}$.

$\mathbf{A}(\delta\mathbf{q}_k)$ can be approximated (from Equation 2.4) for very small values of $\|\delta\mathbf{q}_{vec}\|$ as,

$$\mathbf{A}(\delta\mathbf{q}_k) = \begin{bmatrix} 1 & 2\delta q_3 & -2\delta q_2 \\ -2\delta q_3 & 1 & 2\delta q_1 \\ 2\delta q_2 & -2\delta q_1 & 1 \end{bmatrix} \tag{6.63}$$

The innovation equation can now be written as,

$$\mathbf{e}_k = \mathbf{A}(\delta\mathbf{q}_k)\hat{\mathbf{v}}_{body,k} \times \hat{\mathbf{v}}_{body,k} + \tilde{\mathbf{m}}_k \times \hat{\mathbf{v}}_{body,k} \tag{6.64}$$

Substituting Equation (6.63) into Equation (6.62) and performing the vector multiplication gives,

$$\mathbf{e}_k = 2 \begin{bmatrix} \hat{v}_{by,k}^2 + v_{bz,k}^2 & -\hat{v}_{by,k}\hat{v}_{bx,k} & -\hat{v}_{bz,k}\hat{v}_{bx,k} \\ -\hat{v}_{by,k}\hat{v}_{bx,k} & \hat{v}_{bx,k}^2 + v_{bz,k}^2 & -\hat{v}_{by,k}\hat{v}_{bz,k} \\ -\hat{v}_{bz,k}\hat{v}_{bx,k} & -\hat{v}_{by,k}\hat{v}_{bz,k} & \hat{v}_{bx,k}^2 + v_{by,k}^2 \end{bmatrix} \boldsymbol{\delta q}_k + \mathbf{m}_k$$

$$= \tilde{\mathbf{H}}_k(\hat{\mathbf{v}}_{body,k})\boldsymbol{\delta q}_k + \mathbf{m}_k \qquad (6.65)$$

$$= \begin{bmatrix} \tilde{\mathbf{H}}_k(\hat{\mathbf{v}}_{body,k}) & \mathbf{0}_{3\times3} \end{bmatrix} \boldsymbol{\delta x}_k + \mathbf{m}_k$$

where, $\mathbf{m}_k = \tilde{\mathbf{m}}_k \times \hat{\mathbf{v}}_{body,k}$.

EKF Algorithm:

The EKF algorithm for the FOG bias and attitude estimator is similar to the algorithm presented in Section 6.1 except for a few differences, which will be mentioned below.

Between Measurements:

1) Only the non-linear kinematic equations are propagated because the angular rate measurements are directly obtained from the FOGs. The angular rates in both body and inertial coordinates are obtained to perform the kinematic propagation which is given as,

$$\hat{\boldsymbol{\omega}}_{B,k}^I = \boldsymbol{\omega}_{fog,k}^I - \hat{\mathbf{b}}_k$$
$$\hat{\boldsymbol{\omega}}_{B,k}^O = \hat{\boldsymbol{\omega}}_{B,k}^I - [\mathbf{A}(\hat{\mathbf{q}}_{k/k})]\boldsymbol{\omega}_{o,k} \qquad (6.66)$$

Steps 2) to 4) are similar to the EKF algorithm mentioned in Section 6.1.

Across Measurements:

1) The Kalman filter gain $\mathbf{K}_{k+1}$ is computed in a similar manner as in the previous algorithm.

2. a) Calculate the innovation vector, $\mathbf{e}_{k+1}$.

$$\mathbf{e}_{k+1} = \mathbf{v}_{meas,k+1} \times \mathbf{A}(\hat{\mathbf{q}}_{k+1/k})\mathbf{v}_{orb,k+1} \qquad (6.67)$$

2. b) Obtain the perturbation update.

$$\boldsymbol{\delta x}_{k+1} = [\mathbf{K}_{k+1}]\mathbf{e}_{k+1} \qquad (6.68)$$

in which,

$$\delta \mathbf{q}_{\mathbf{vec},k+1} = [\mathbf{K}_{q,k+1}]\mathbf{e}_{k+1} \quad \text{and} \quad \delta \mathbf{q}_{k+1} = \begin{bmatrix} \delta \mathbf{q}_{\mathbf{vec},k+1} \\ \sqrt{1 - \|\delta \mathbf{q}_{\mathbf{vec},k+1}\|} \end{bmatrix}$$

3) Update the state vector using the innovation.

$$\hat{\mathbf{q}}_{k+1/k+1} = \delta \mathbf{q}_{k+1} \otimes \hat{\mathbf{q}}_{k+1/k}$$
$$\hat{\mathbf{b}}_{k+1} = \hat{\mathbf{b}}_k + [\mathbf{K}_{b,k+1}]\mathbf{e}_{k+1}$$

(6.69)

Steps 4) and 5) are similar to the EKF algorithm in Section 6.1

6.2.3 Results

The attitude states will not be shown because an examination of the attitude RMS error is sufficient to analyse attitude state performance. The graphs in Figure 6.3 shows the RMS error associated with the attitude estimate and the FOG bias estimates.
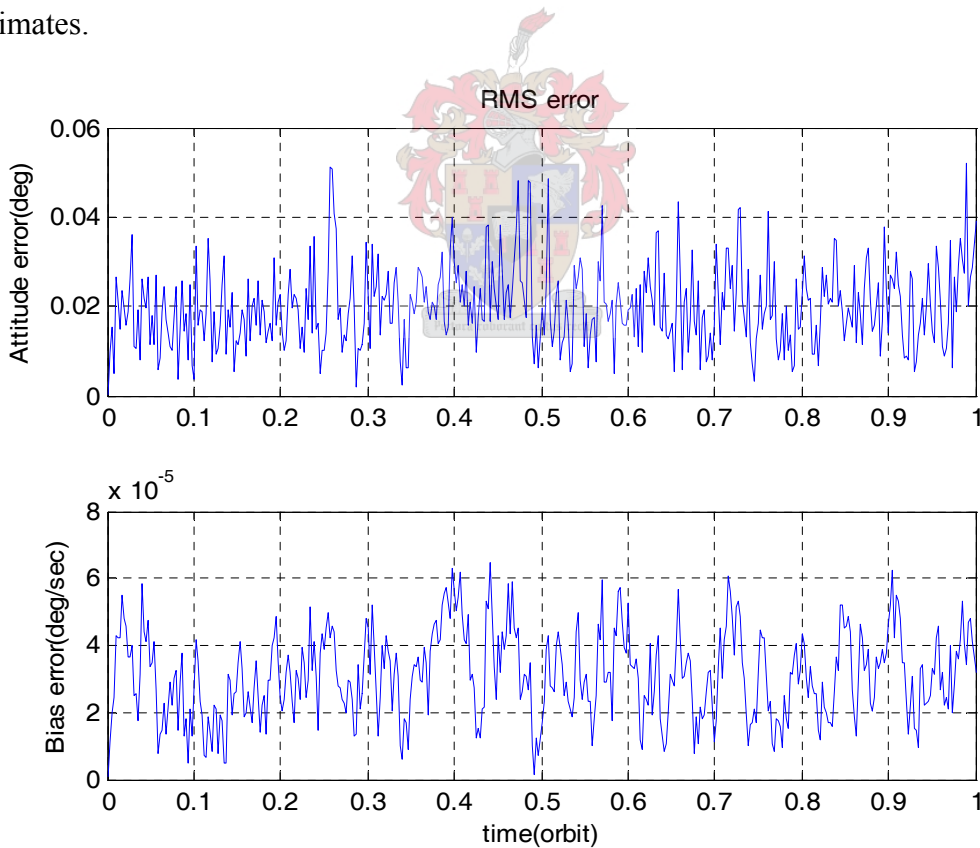
Figure 6.3 RMS error in attitude and bias estimates

The sensors that were used in this simulation included the magnetometer along with the ES. All noise specifications for the sensors are similar to that mentioned in

Section 6.1.3.   The FOGs were assumed to have a measurement noise standard deviation (σ_{FOG}) of 1×10^{-4} deg/sec and a bias noise standard deviation that is 0.01 times the measurement noise standard deviation.   The RMS error in attitude was around 0.02° while the bias error was determined to be 3×10^{-5} deg/sec.   As expected the RMS error in attitude is smaller than a full state EKF.   This is because the body rate measurements are directly available in this case whereas body rates were estimated in a full state EKF.

The bias estimates and the actual estimates are shown in Figure 6.4.   As expected the estimated bias components follow the actual bias components of the FOGs.   Once the bias components are estimated they are subtracted from the FOG measurements thereby cancelling out the effects of the actual bias components.   The actual and estimated bias components which are shown in Figure 6.4 have been converted from rad/sec to deg/sec and then plotted.   The same applies to the bias RMS error in Figure 6.3.
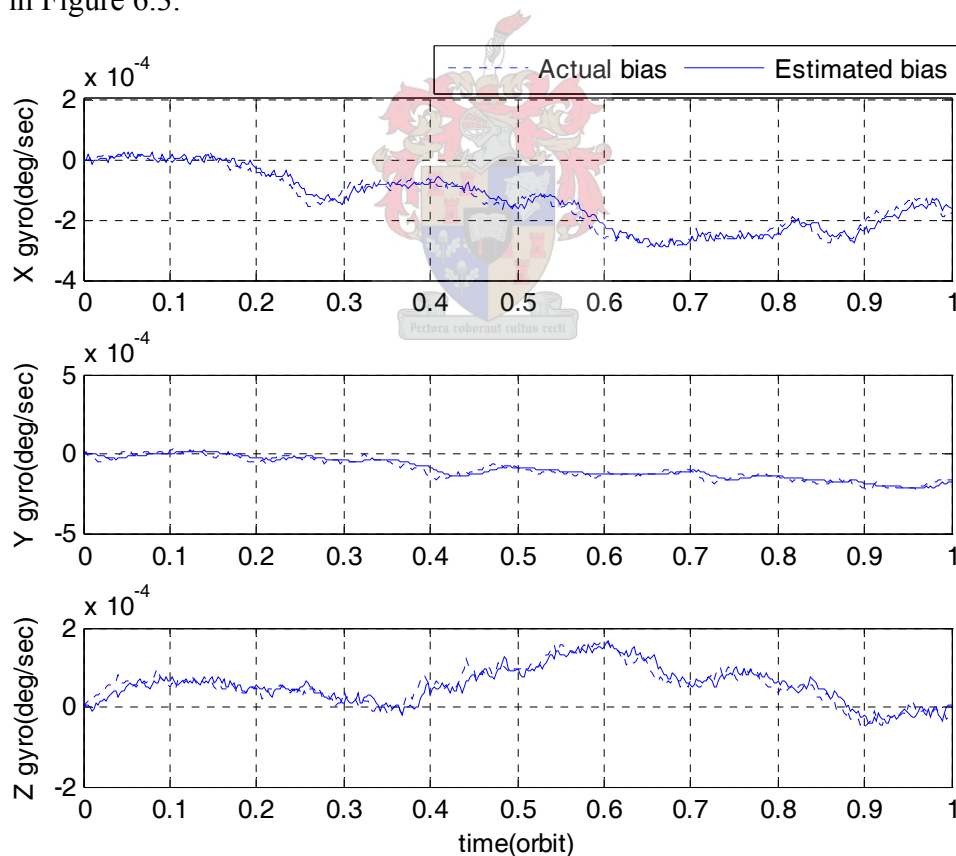
Figure 6.4 Actual bias versus estimated bias

6.3 Vector computation from Sensors

Magnetometer vector pair:

The measured magnetic measurements are obtained from a magnetometer in reality. In this case the measured magnetic measurements are obtained from Equation C.14 to which a random noise signal is added (Section 4.2). The measured vector is then normalised to obtain the measured innovation vector (which is a unit vector).

$$\mathbf{v}_{meas,k} = \frac{\mathbf{B}_{VEC,k}^{B}}{\left\|\mathbf{B}_{VEC,k}^{B}\right\|} \tag{6.70}$$

The modelled magnetic vector is obtained from the IGRF model mentioned in Appendix C (Equation C.13). This vector is then normalised to give the modelled innovation vector.

$$\mathbf{v}_{orb,k} = \frac{\mathbf{B}_{VEC,k}^{O}}{\left\|\mathbf{B}_{VEC,k}^{O}\right\|} \tag{6.71}$$

N.B. The 'k' subscript on the modelled and measured sensor vectors indicates the vectors during the sample instant when sensor measurements are available.
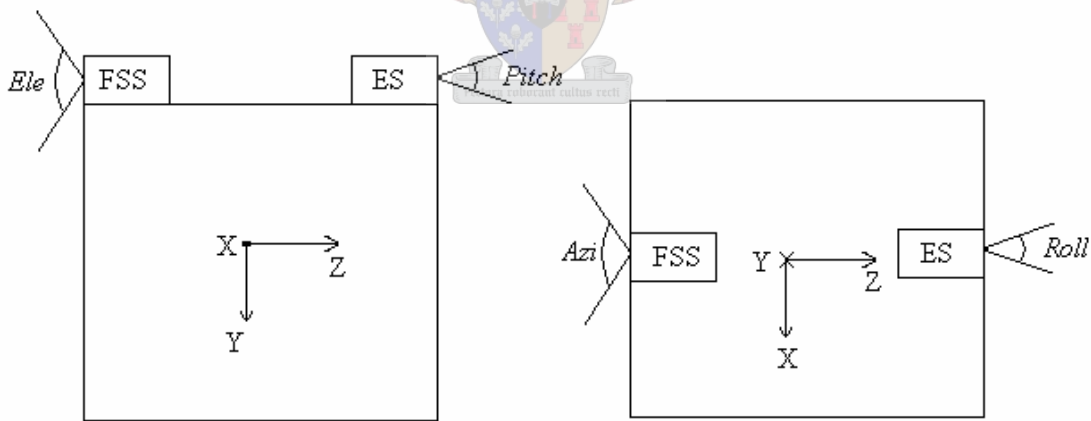
Figure 6.5 FSS and ES placement

Earth Sensor vector pair:

The ES (Section 4.2.2) gives the output directly in the roll and pitch angles. These angles need to be converted to unit vectors in body coordinates before they can

be used as a measured innovation vector. The modelled vector of the Earth or the nadir vector is $\mathbf{E}_{VEC}^{O}$ (Section 3.5) and the components of $\mathbf{E}_{VEC}^{O}$ are represented as,

$$\mathbf{E}_{VEC}^{O} = [E_x^o \ E_y^o \ E_z^o]^T = [0 \ 0 \ 1]^T \tag{6.72}$$

Using this data the ES output can be converted to the body coordinates. Before proceeding further it would be helpful to describe the notation for the nadir vector in body coordinates.

$$\mathbf{E}_{VEC}^{B} = [E_x^b \ E_y^b \ E_z^b]^T \tag{6.73}$$

The stepwise procedure of calculating the nadir vector in body coordinates is given:

1) Since the boresight of the ES is placed along the Z body axis, the Z component of the nadir vector in body coordinates can be calculated using the estimated DCM as,

$$\hat{E}_z^b = [E_x^o \hat{A}_{31} + E_y^o \hat{A}_{32} + E_z^o \hat{A}_{33}] = \hat{A}\mathbf{E}_{VEC}^{O} \tag{6.74}$$

2) When ES measurement angles are available, the nadir vector components in the X and Y body coordinates are calculated as,

$$E_{xk}^b = \tan(Pitch)\,\hat{E}_z^b$$
$$E_{yk}^b = \tan(Roll)\,\hat{E}_z^b$$

along with $E_{zk}^b = \hat{E}_z^b$.

   Pitch and *Roll* are the ES measurement angles along the X-body and Y-body axis respectively (Figure 6.5).

Therefore the measured nadir vector in body coordinates is,

$$\mathbf{E}_{VEC,k}^{B} = [E_{xk}^b \ E_{yk}^b \ E_{zk}^b]^T \tag{6.75}$$

The measured innovation vector from the ES is then calculated as,

$$\mathbf{v}_{meas,k} = \frac{\mathbf{E}_{VEC,k}^{B}}{\left\|\mathbf{E}_{VEC,k}^{B}\right\|} \tag{6.76}$$

while the modelled innovation vector for the ES output is calculated as,

$$\mathbf{v}_{orb,k} = \frac{\mathbf{E}_{VEC,k}^{O}}{\left\|\mathbf{E}_{VEC,k}^{O}\right\|} \tag{6.77}$$

Fine Sun Sensor vector pair:

The conversion of the FSS (Section 4.3.3) outputs from azimuth and elevation angles to unit vectors in body coordinates are done in a similar fashion as that was done for the ES. The difference occurs when the FSS is placed in a sensor frame rather than the normal body coordinates.

Figure 6.5 FSS is not placed in the body coordinates and has its boresight opposite to the Z body axis, the sensor measurements need to be transformed to body coordinates before being used by the EKF. A vector in the body coordinates can be transformed to the sensor coordinates using a transformation matrix **[D]**. This matrix can be formed using an Euler rotation sequence. The components of this matrix do not change because the displacement of the sensor coordinates from the body frame is fixed. The relation between the two coordinates can be given as,

$$\mathbf{S}_{\text{VEC}}^{\mathbf{S}} = [\mathbf{D}]\mathbf{S}_{\text{VEC}}^{\mathbf{B}} \tag{6.78}$$

where,

$$\mathbf{S}_{\text{VEC}}^{\mathbf{B}} = [S_x^b \ S_y^b \ S_z^b]^T = \text{components of Sun vector in body coordinates}$$

$$\mathbf{S}_{\text{VEC}}^{\mathbf{S}} = [S_x^s \ S_y^s \ S_z^s]^T = \text{components of Sun vector in sensor coordinates}$$

Since the FSS vector is obtained in sensor coordinates, the FSS vector in body coordinates is calculated using the inverse of the matrix **[D]** which is expressed as,

$$\mathbf{S}_{\text{VEC}}^{\mathbf{B}} = [\mathbf{D}]^{-1}\mathbf{S}_{\text{VEC}}^{\mathbf{S}} \tag{6.79}$$

The step wise calculation of the Sun vector in body coordinates is give next:

1) Convert the FSS output angles to a unit vector in the sensor coordinates. The Z-component of the Sun vector in the sensor coordinates is expressed as,

$$S_z^s = [S_x^b D_{31} + S_y^b D_{32} + S_z^b D_{33}] \tag{6.80}$$

where, $\mathbf{S}_{\text{VEC}}^{\mathbf{B}}$ is obtained from $\mathbf{S}_{\text{VEC}}^{\mathbf{B}} = \mathbf{A}(\hat{\mathbf{q}})\mathbf{S}_{\text{VEC}}^{\mathbf{O}}$

$\mathbf{S}_{\text{VEC}}^{\mathbf{O}}$ is calculated in Section 3.3 and is represented as,

$$\mathbf{S}_{\text{VEC}}^{\mathbf{O}} = [S_x^o \ S_y^o \ S_z^o]^T = \text{components of Sun vector in orbit coordinates}$$

2) The components of the Sun vector in the X and Y sensor coordinates is calculated as,

$$S_{xk}^{s} = \tan(Azi)\, S_{z}^{s}$$

$$S_{yk}^{s} = \tan(Ele)\, S_{z}^{s}$$

along with $S_{zk}^{s} = S_{z}^{s}$.

Ele and Azi are the FSS measurement angles along the X-body and Y-body axis respectively (Figure 6.5).

Therefore the measured Sun vector in sensor coordinates is,

$$\mathbf{S}_{\mathbf{VEC},k}^{\mathbf{S}} = [S_{xk}^{s} \;\; S_{yk}^{s} \;\; S_{zk}^{s}]^{T} \tag{6.81}$$

3) Using the above equation and Equation (6.79) the Sun vector in body coordinates is calculated as,

$$\mathbf{S}_{\mathbf{VEC},k}^{\mathbf{B}} = [\mathbf{D}]^{-1} \mathbf{S}_{\mathbf{VEC},k}^{\mathbf{S}} \tag{6.82}$$

We are now in a position where we can calculate the innovation pair vectors. The measured innovation vector from the FSS is given as,

$$\mathbf{v}_{meas,k} = \frac{\mathbf{S}_{\mathbf{VEC},k}^{\mathbf{B}}}{\left\| \mathbf{S}_{\mathbf{VEC},k}^{\mathbf{B}} \right\|} \tag{6.83}$$

while the modelled innovation vector is,

$$\mathbf{v}_{orb,k} = \frac{\mathbf{S}_{\mathbf{VEC},k}^{\mathbf{O}}}{\left\| \mathbf{S}_{\mathbf{VEC},k}^{\mathbf{O}} \right\|} \tag{6.84}$$

6.4 Propagation of states by numerical integration

The numerical integration technique constitutes an integral part of the EKF propagation section. The most common technique used for spacecrafts is the R-stage Runge-Kutta method (Wertz, 1978 and Pocha, 1987). Steyn (1995) has discussed a technique called Hodgart's single step method which is suited for satellites spinning around the Z-body axis. However a modified Euler integration technique was deemed to be sufficient in this case due to the near stationary dynamic characteristics of a GEO satellite. The modified Euler method is a two stage, 2nd order, single step method. The state propagation methods employed in the two EKFs discussed earlier

differ slightly in nature and will therefore be discussed separately. The sampling period used to implement the EKFs was chosen to be $T_s = 1$ second.

State Propagation for a Full State EKF:

1) Calculate current angular acceleration along each body axis.

$$\dot{\omega}_{ix,k} = \frac{T_{MX} + T_{TX} + [I_{YY} - I_{ZZ}]\hat{\omega}_{iy,k/k}\hat{\omega}_{iz,k/k} - \hat{\omega}_{iy,k/k}h_{wz} + \hat{\omega}_{iz,k/k}h_{wy} - \dot{h}_{wx}}{I_{XX}}$$

$$\dot{\omega}_{iy,k} = \frac{T_{MY} + T_{TY} + [I_{ZZ} - I_{XX}]\hat{\omega}_{iz,k/k}\hat{\omega}_{ix,k/k} - \hat{\omega}_{iz,k/k}h_{wx} + \hat{\omega}_{ix,k/k}h_{wz} - \dot{h}_{wy}}{I_{YY}} \qquad (6.85)$$

$$\dot{\omega}_{iz,k} = \frac{T_{MZ} + T_{TZ} + [I_{XX} - I_{YY}]\hat{\omega}_{ix,k/k}\hat{\omega}_{iy,k/k} - \hat{\omega}_{ix,k/k}h_{wy} + \hat{\omega}_{iy,k/k}h_{wx} - \dot{h}_{wz}}{I_{ZZ}}$$

2) Calculate the angular rate increment.

$$\Delta\omega_{ix,k} = 0.5T_s\,(3\dot{\omega}_{ix,k} - \dot{\omega}_{ix,k-1})$$
$$\Delta\omega_{iy,k} = 0.5T_s\,(3\dot{\omega}_{iy,k} - \dot{\omega}_{iy,k-1}) \qquad (6.86)$$
$$\Delta\omega_{iz,k} = 0.5T_s\,(3\dot{\omega}_{iz,k} - \dot{\omega}_{iz,k-1})$$

3) Propagate angular rate increments.

$$\hat{\omega}_{ix,k+1/k} = \hat{\omega}_{ix,k/k} + \Delta\omega_{ix,k}$$
$$\hat{\omega}_{iy,k+1/k} = \hat{\omega}_{iy,k/k} + \Delta\omega_{iy,k} \qquad (6.87)$$
$$\hat{\omega}_{iz,k+1/k} = \hat{\omega}_{iz,k/k} + \Delta\omega_{iz,k}$$

4) Obtain the orbit referenced angular rates.

$$\hat{\omega}_{ox,k+1/k} = \hat{\omega}_{ix,k+1/k} + \hat{A}_{12}\omega_{o,k}$$
$$\hat{\omega}_{oy,k+1/k} = \hat{\omega}_{iy,k+1/k} + \hat{A}_{22}\omega_{o,k} \qquad (6.88)$$
$$\hat{\omega}_{oz,k+1/k} = \hat{\omega}_{iz,k+1/k} + \hat{A}_{32}\omega_{o,k}$$

5) Once the angular rates in orbit coordinates have been obtained, we can propagate the kinematic quaternion equations. The equations used to propagate the kinematics are given as (Wertz, 1978 p.565)

$$\mathbf{q}_{k+1} = \exp\left[\frac{1}{2}\mathbf{\Omega}_k T_s\right]\mathbf{q}_k$$

$$= \left[\cos\left(\frac{\bar{\omega}_k T_s}{2}\right)\mathbf{I} + \frac{1}{\bar{\omega}_k}\sin\left(\frac{\bar{\omega}_k T_s}{2}\right)\mathbf{\Omega}_k\right]\mathbf{q}_k$$

(6.89)

where,

$$\bar{\omega}_k = \sqrt{\hat{\omega}_{ox,k+1/k}^2 + \hat{\omega}_{oy,k+1/k}^2 + \hat{\omega}_{oz,k+1/k}^2} \quad \text{and } \mathbf{\Omega}_k \text{ is similar to Equation (2.10).}$$

State Propagation for the FOG bias and attitude EKF:

Since the angular rate measurements are directly obtained from the FOGs the need to determine and propagate angular rate measurements are eliminated.

1) The angular rates are obtained using the FOG measurements and bias estimates.

$$\hat{\omega}_{ix,k+1/k} = \omega_{fogx,k} - \hat{b}_{x,k}$$

$$\hat{\omega}_{iy,k+1/k} = \omega_{fogy,k} - \hat{b}_{y,k}$$

$$\hat{\omega}_{iz,k+1/k} = \omega_{fogz,k} - \hat{b}_{z,k}$$

(6.90)

Steps 2) and 3) are similar to steps 4) and 5) in the full state EKF.

6.5 Practical Considerations

The selection of the perturbation state covariance matrix $\mathbf{P}_k$ and the system and measurement noise covariance matrices $\mathbf{Q}$ and $\mathbf{R}$ requires some attention. The $\mathbf{P}_k$ matrix has non-zero positive elements only along the diagonal. The initial value of the $\mathbf{P}_k$ matrix denoted as $\mathbf{P}_o$ was chosen to be three orders of magnitude larger than the system covariance matrix $\mathbf{Q}$ (Steyn, 1995). Simulations were done to observe the convergence of $\mathbf{P}(k)$ to the steady-state values. In-spite of fine tuning the $\mathbf{P}_o$ values to minimise the convergence time, the overall performance of the EKFs did not change much. This was due to the non-linear characteristics of the system.
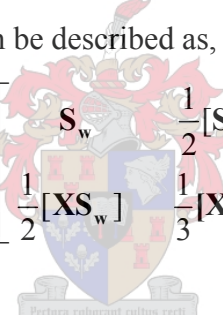
According to Psiaki (1990) values of $\mathbf{Q}$ and $\mathbf{R}$ determines the trade off between the tracking of disturbance noise induced state variations and the filtering of measurement noise. This can be explained by the fact that a low value of $\mathbf{R}$ indicates

a low covariance on the sensor measurements which gives the filter the impression that the measurements contain very little noise. In reality we might have a noisy sensor and this could cause filter divergence. The same explanation applies for the **Q** matrix and the characteristics of the system. Therefore it is essential to obtain a certain amount of balance between the two.

The **R** matrix value can be obtained from the sensor accuracy characteristics in the data sheets which usually only tend to be an approximation. As an example the calculation of the variance of the ES will be discussed. The data sheet in Section F.1 gives the $3\sigma_{ES}$ accuracy of the ES to be $0.025°$. The variance (σ_{ES}^2) can then be calculated to be 6.94×10^{-5}. This value can then be fine tuned to optimise the performance.

6.5.1 Q matrix for full state estimator

The system noise covariance matrix **Q** was calculated according to the discussion in Steyn (2004) and can be described as,

$$\mathbf{Q} = \begin{bmatrix} \mathbf{S}_\mathbf{w} & \frac{1}{2}[\mathbf{S}_\mathbf{w}\mathbf{X}^T] \\ \frac{1}{2}[\mathbf{X}\mathbf{S}_\mathbf{w}] & \frac{1}{3}[\mathbf{X}\mathbf{S}_\mathbf{w}\mathbf{X}^T] \end{bmatrix} \tag{6.91}$$

where,

$$\mathbf{X} = \frac{\partial \dot{\mathbf{q}}}{\partial \boldsymbol{\omega}_B^I} \text{ (as described in Equation (6.16))}$$

$$\mathbf{S}_\mathbf{w} = \sigma_{wbo}^2 [\mathbf{I}]_{3\times3}$$

σ_{wbo}^2 is the angular rate noise variance and is assumed to be equal for all three axes. The terms off the diagonal describes the coupling covariance between the attitude and the angular rates. The standard deviation σ_{wbo} was chosen to be 3.15×10^{-7} rad after few trials. A good starting point is to choose a value close two orders of magnitude lesser than ω_o.

6.5.2 Q matrix for FOG bias estimator

The values of the **Q** matrix for the FOG bias estimator was also chosen from Steyn (2004) and is described as,

$$\mathbf{Q} = \begin{bmatrix} \dfrac{\sigma_{\eta 1}^2}{4}[\mathbf{I}]_{3\times 3} & \dfrac{-\sigma_{\eta 1}^2}{16}[\mathbf{I}]_{3\times 3} \\ \dfrac{-\sigma_{\eta 2}^2}{4}[\mathbf{I}]_{3\times 3} & \sigma_{\eta 2}^2[\mathbf{I}]_{3\times 3} \end{bmatrix} \tag{6.92}$$

where,

$\dfrac{\sigma_{\eta 1}^2}{4}[\mathbf{I}]_{3\times 3}$ is the FOG measurement covariance ($\sigma_{\eta 1} = \sigma_{FOG}$)

$\sigma_{\eta 2}^2[\mathbf{I}]_{3\times 3}$ is the FOG bias covariance ($\sigma_{\eta 2} = 0.01\sigma_{\eta 1}$)

The standard deviation 'σ_{FOG}' value has been discussed in Section 6.2.3. However while using the covariance values in the covariance matrix care must be taken to convert (deg/sec) to (rad/sec).
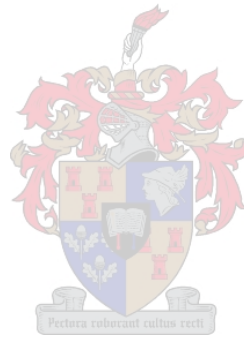
Chapter 7

Orbit Control

This chapter explains the factors that cause drifts along the East-west (longitudinal) and North-south (latitudinal) direction of the spacecraft. The techniques employed in correcting these drifts are called station-keeping manoeuvres. These manoeuvres are performed by thrusters which when fired generate an effective thrust vector along the centre of mass of the satellite.

It is impossible to fire a thruster along the *exact* centre of mass because of the practical inaccuracies while mounting a thruster. The misalignment of the thrust vector from the centre of mass of the satellite is termed as thruster misalignment. Thruster misalignment can also occur if the centre of mass varies as a result of propellant consumption. The torques generated due to the thruster misalignment tends to destabilise the satellite. Therefore it becomes essential to control the attitude of the satellite while performing orbit control.

The amount of propellant required to perform station-keeping over a 10 year period (lifetime of the GEO satellite considered) is also calculated.

7.1 North-South Station Keeping (NSSK)

Station-keeping in the North-south direction is done by controlling the inclination of the satellite orbit. Failure to do so will lead to a figure '8' type of oscillation of the satellite around the nominal longitude. The actual orbital inclination will be half the oscillation's peak to peak amplitude. Figure 1.1 (chapter 1) shows satellite 'B' located at 120° W longitude oscillating between 30° N and 30° S latitude, the inclination of the orbit being 30°. This is an apparent motion to an observer on the Earth's surface (Wertz and Larson, 1999). The oscillation occurs once a day and makes satellite tracking complicated. Also, this type of oscillation is not at all acceptable on communication satellites where the footprint of the satellite has to cover a particular geographical area continuously.

7.1.1 Causes of North-south drift

The primary reason for the drift in orbital inclination is the gravitational attraction of the Sun and the Moon on the satellite. The gravitational forces depend very much on how the orbit is oriented. From Pocha (1987) it can be seen that if the orbit pole (normal to the orbit plane) is oriented towards the vernal equinox, the inclination drift gradually starts to build up. This can be described also in terms of the RAAN (Right Ascension of Ascending Node-Ω). The RAAN is the angle between Vernal equinox and the ascending node of the satellite. The ascending node in turn is the point where the satellite crosses the equator from the southern hemisphere to the northern hemisphere. When the RAAN is between $0°$ and $180°$, the orbit pole will be inclined towards the vernal equinox.
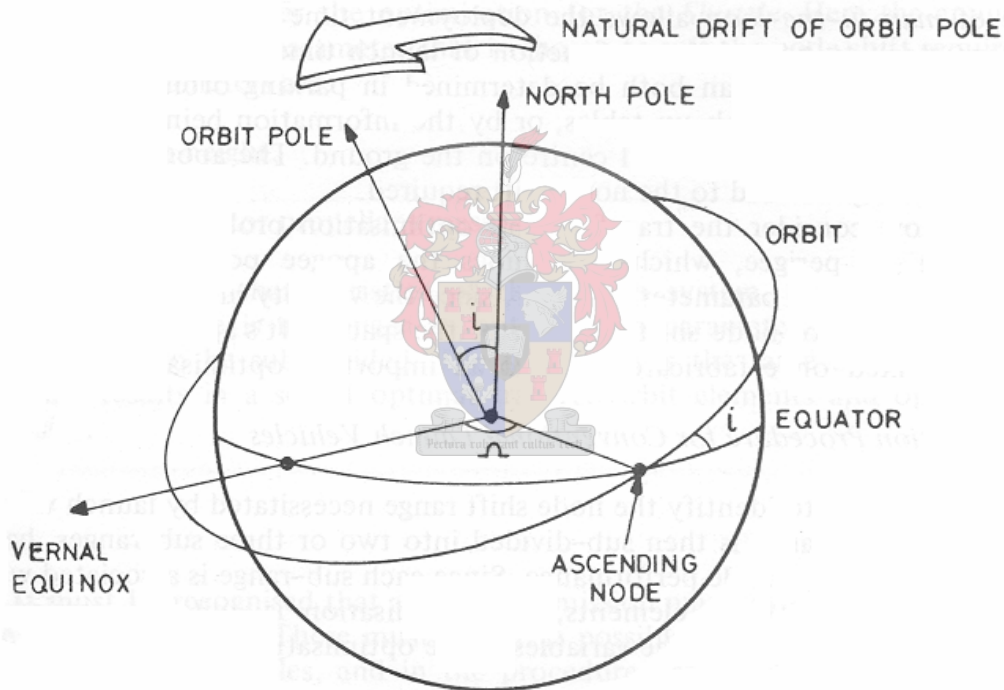
Figure 7.1 Orbit pole drift (From Pocha, 1987, p 35)

By changing the RAAN to a value between 180° and 360° the orbit pole gets oriented to the side of the North Pole away from the vernal equinox. After this the orbit pole drifts back gradually towards the vernal equinox via the North Pole, thereby decreasing the inclination. Once the orbit pole has passed the North Pole, the inclination starts to increase again and the RAAN changes to an angle between

$0°$ and $180°$. Berlin (1988) tells us that the drift rate of the inclination vector can be described as,

$$\frac{\mathrm{d}i}{\mathrm{d}t} = \sqrt{u^2 + v^2} \quad \text{(deg/year)} \tag{7.1}$$

where,

$$u = -0.1314\sin\Omega_m \quad \text{(deg/year)}$$

$$v = 0.8541 + 0.09855\cos\Omega_m \quad \text{(deg/year)}$$

$$\Omega_m = 12.111 - 0.052954t \quad \text{(deg)}$$

Ω_m is the RAAN of the Moon which has a period of 18.6 years. With these data the drift rate ($\mathrm{d}i/\mathrm{d}t$) can be calculated to be between 0.756 and $0.952°/\text{year}$. The inclination vector can be represented in terms of the inclination and RAAN angles, in the inertial coordinates (by comparing Figures 2.2 and 7.1) as,

$$\mathbf{i} = [\sin i \cos\Omega \quad \sin i \sin\Omega \quad \cos i]^T \tag{7.2}$$

This representation will be helpful in future analysis.

7.1.2 Corrections of North-south drift

The frequency of the NSSK manoeuvres depends on the size of inclination window permitted for the satellite. The maximum drift limit allowed for a communication satellite is usually $\pm 0.1°$. As mentioned earlier a drift in the inclination vector translates to a drift of 'i' and 'Ω'. Maintaining the inclination vector around $0°$ inclination is a very fuel hungry process. To avoid this, the satellite is usually allowed to drift to one end of the permitted window and then pushed back to the other end so as to minimise the number of corrections. The two inclination vectors (before and after inclination correction) can be represented in the vector form as,

$$\mathbf{i}_1 = [\sin i_1 \cos\Omega_1 \quad \sin i_1 \sin\Omega_1 \quad \cos i_1]^T$$

$$\mathbf{i}_2 = [\sin i_2 \cos\Omega_2 \quad \sin i_2 \sin\Omega_2 \quad \cos i_2]^T$$

where,

$i_1, \Omega_1 = $ inclination and RAAN angle of the inclination vector before orbit correction

$i_2, \Omega_2 = $ inclination and RAAN angle of the inclination vector after orbit correction

The orbital plane change between the two vectors is calculated as,

$$\cos\theta = \mathbf{i}_1 . \mathbf{i}_2 \qquad (7.3)$$

The two inclination angles i_1 and i_2 will be equal. This can be illustrated better with an example. The communication satellite is allowed to drift to one end of the inclination window where the inclination vector $\mathbf{i}_1$ has an inclination of i_1, $0.1°$. At this point the RAAN angle is changed in order to shift the orbit pole away from the vernal equinox. The inclination vector now gets shifted to the other end of the inclination window. This new inclination vector $\mathbf{i}_2$ also tends to have an inclination of $0.1°$. Even though the inclination angles of the two vectors $\mathbf{i}_1$ and $\mathbf{i}_2$ are the same their directions are different, which justifies the representation of inclination in terms of vectors.

Thus,

$$i_1 = i_2 = i = 0.1° \ .$$

Equation (7.3) with the above relation gets simplified to,

$$\cos\theta = \sin^2 i \ \cos(\Omega_2 - \Omega_1) + \cos^2 i \qquad (7.4)$$

The amount of propellant required to bring about a plane change of 'θ' is given as,

$$\Delta V^2 = 2V^2(1 - \cos\theta) \qquad (7.5)$$

where,

ΔV = change in velocity required to perform the manoeuvre

V = nominal velocity of a GEO satellite = 3075 m/s

The average drift rate of the inclination vector can be assumed to be $0.8°$/ year or $0.067°$/month. A communication satellite with $0.2°$ ($\pm 0.1°$) window will require a NSSK manoeuvre once in 3 months (4 manoeuvres/year).

The satellite is assumed to have an initial RAAN of $\Omega_1 = 90°$. The aim is to reorient the inclination vector or the orbit pole so that the satellite has a RAAN of $\Omega_2 = 270°$. Therefore, $\Delta\Omega = \Omega_2 - \Omega_1 = 180°$. With this data, the plane change required (θ) can

be calculated from Equation (7.4) which in turn is substituted into Equation (7.5). ΔV is thus calculated to be 10.73 m/s. The amount of propellant required can be calculated from the rocket equation which is given as

$$\Delta V = g I_{sp} \ln\left(\frac{m_i}{m_f}\right) \tag{7.6}$$

where,

ΔV = change in velocity required to perform the manoeuvre

g = Earth's gravitational acceleration

I_{sp} = specific impulse of propellant used

m_i = mass of satellite before the manoeuvre (initial mass)

m_f = mass of satellite after the manoeuvre (final mass)

The final mass can also be written as $m_f = m_i - \Delta m$, where Δm is the mass of the propellant used. Equation (7.6) can be rearranged as,

$$\Delta m = m_i \left\{ 1 - \exp\left(\frac{-\Delta V}{g I_{sp}}\right) \right\} \tag{7.7}$$

The propellant considered is Hydrazine (N_2H_4) which has an I_{sp} of 290 seconds. Initial mass of satellite is considered to be 500kg (section 2.1). Δm is thus calculated to be 1.87 kg. The amount of propellant required for a year would approximately be 7.52 kg (for four manoeuvres). Care must be taken while computing the propellant mass because the initial mass keeps decreasing according to amount of propellant consumed. A worst case approximation of the amount of propellant required to perform NSSK over a 10 year period would be around 75 kg.

The thrust impulse of a NSSK thruster firing can be calculated using the formula,

$$\int_0^t F = I_{sp} g \Delta m \tag{7.8}$$

$\int F$ is calculated to be approximately 5350 Ns (Newton-second) which can be interpreted as 20 Newton thrust which lasts for 267.5 seconds. Mathematically it is also possible to fire a 2 Newton thrust for 2675 seconds to give an equivalent thrust impulse. Practically, long duration thruster firings are avoided but decreasing the thrust duration comes at a cost of higher thrust levels. Large thrust levels can only be

achieved by increasing the size of the thruster which leads to an increase in mass of the entire system. Therefore choosing the thrust level of the thruster is a trade-off depending on the type of manoeuvre and its impact on the weight of the entire system. Hence it can be concluded that NSSK requires a high power thruster and a 10 Newton thruster fired for 535 seconds provides a good trade-off.

7.1.3 NSSK Thruster Placement

The thruster used for NSSK is a high power thruster as shown in Figure 4.3. The idea behind using a single thruster for NSSK is because the drift of the orbit pole tends to shift the latitude upwards and not downwards. The correcting thrust should therefore push the satellite downwards which justifies the placement of the HPT on the upper facet of the satellite.

7.2 East-West Station Keeping (EWSK)

The idea behind EWSK is to maintain the longitude of the satellite around an allotted longitude position. The longitude window permitted for communication satellites are generally $\pm 0.1°$. A $0.1°$ tolerance at GEO altitude translates to a distance of approximately 75km in the GEO sphere. The total width of the window is $0.2°$. These stringent specifications are necessary in order to avoid signal interference with neighbouring satellites.

7.2.1 Causes of East-west drift

The drift in longitude of the satellite is mainly caused by the non-uniform gravitational field of the Earth which is a result of the non-homogenous distribution of the mass on Earth. Since the Earth's gravity varies slightly with latitude and longitude, the satellite experiences gravity gradients at different points above Earth. These gradients give rise to accelerations and decelerations depending on the sub-satellite position. According to Berlin (1988) a simplified representation of the East-west (longitudinal) acceleration on a GEO satellite along the equator is,

$$\frac{d^2 L}{dt^2} = \ddot{L} = C \sin(150° - 2L) \quad (\text{deg}/\text{day}^2) \tag{7.9}$$

where,

L = nominal longitude of satellite

$$C = \{16.9 + 2.9\sin(L - 35°)\} \times 10^{-4}$$

A detailed analysis of the gravitational perturbation is provided in Maral and Bousquet (1986).

As Equation (7.9) suggests there will be four points on the equator where the longitudinal drift of the satellite will become zero. This is graphically shown in Figure 7.2. The points where Equation (7.9) becomes zero is when L takes the values $-15°, -105°, 75°$ and $165°$. The negative values of L constitute longitudes to the west of the Greenwich meridian while the positive values are to the east. Thus,

$$\ddot{L} = 0 \quad \text{when} \quad L = 15°W, 105°W, 75°E \text{ and } 165°E$$

A satellite which is stationed at any of these four points will not move, whereas it will accelerate east or west for any other longitude.
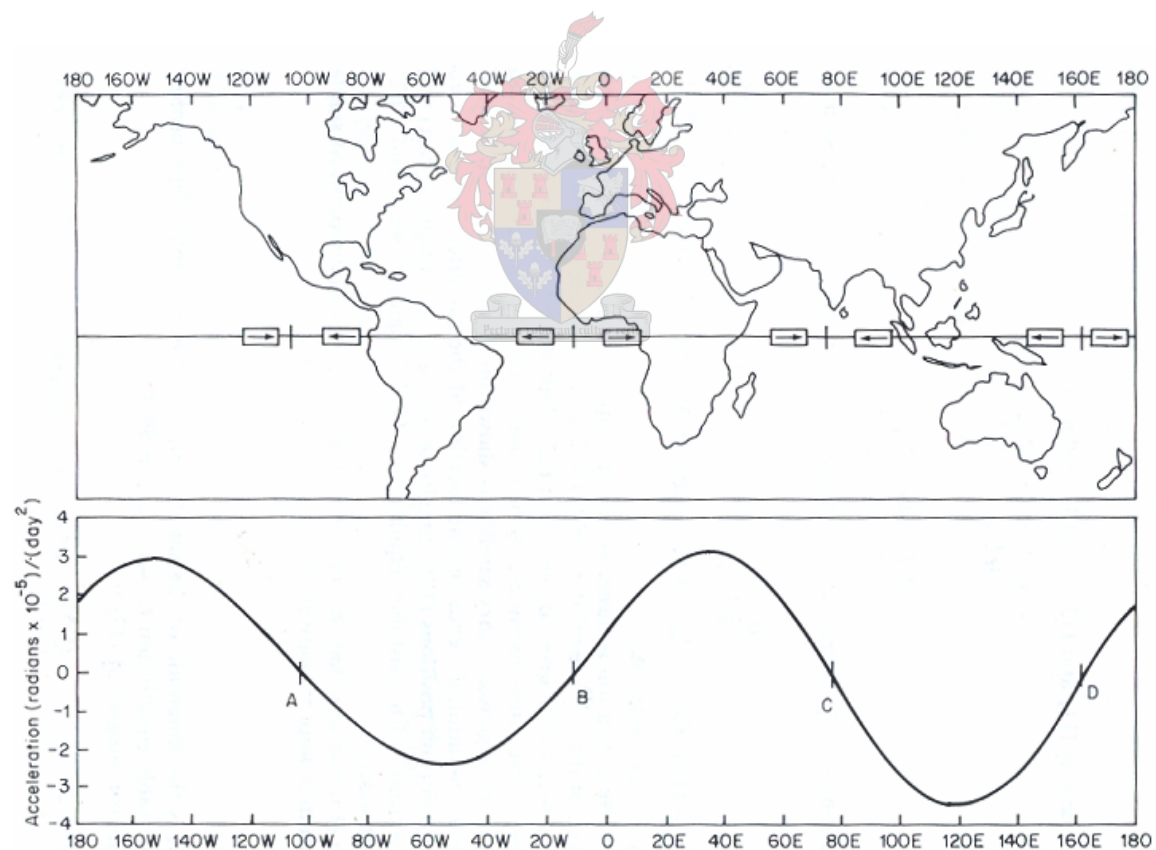
Figure 7.2 Longitudinal acceleration of a GEO satellite depending on its longitude

Points A ($105°W$) and C ($75°E$) (Figure 7.2) are called stable points whereas B ($15°W$) and D ($165°E$) are unstable points. The reason for such a terminology is

because of the fact that a satellite approaching point A or C will have a longitudinal acceleration which increases at a very slow rate. Once these points are passed the acceleration becomes negative (deceleration). If any further external torques such as luni-solar torques act on the satellite it will just oscillate around those points. Points B and D are called unstable points because, the presence of any external torques will cause the satellite to drift away from the point (B or D) towards the nearest stable points. Therefore a satellite placed at B or D will continue to stay there only if it is left unperturbed which is hardly a real world scenario. In the real world however, the stable points are located at $104°$W and $74°$E , while the unstable points are at $12°$W and $162°$E (Berlin 1988).

7.2.2 Corrections of East-west drift

As Figure 7.2 suggests a satellite placed in between the stable and unstable points will undergo maximum drift and will require larger amounts of propellant to perform EWSK. Also the frequency of the EWSK manoeuvres will be larger.

The strategy involved is similar to the one employed in NSSK. The satellite is allowed to drift to one end of the longitude window, at which the EWSK manoeuvre is performed. The thrust impulse is given in the direction opposite to the drift so that the satellite reaches the other end of the longitude window. The longitudinal drift for a GEO satellite can be calculated using Equation(7.9). The nominal longitude of the satellite is chosen as $19.5°$East (section 3.1). Longitudinal drift acceleration is calculated as,

$$\ddot{L} = 1.5054 \times 10^{-3} \text{ (deg/day}^2) \quad \text{where } C = 1.6125 \times 10^{-3}.$$

ΔL is the half-width of the drift window, which in this case is $0.1°$.

The required change in velocity of the satellite is calculated as,

$$\Delta V = 11.36\sqrt{\ddot{L}\Delta L} \quad (m/s) \tag{7.10}$$

ΔV for a single EWSK manoeuvre happens to be 0.139m/s. Propellant mass required for a single manoeuvre can be calculated from Equation (7.7) as 0.0245 kg. The period the satellite takes to travel from one end of the longitude window to the other end is given as,

$$\tau = 4\sqrt{\Delta L / \ddot{L}} \quad \text{(days)} \tag{7.11}$$

The satellite takes 32.6 days to transverse form one end to the other end of the inclination window. Using this data the amount of propellant required to perform EWSK over a year is calculated as,

$$\frac{\Delta m}{\text{year}} = \frac{\Delta m}{\text{manoeuvre}} \times \frac{360°}{\tau} \qquad\qquad (7.12)$$

Annual propellant consumption for EWSK is calculated to be 0.2705 kg. It can be observed that the annual propellant consumption for EWSK is much less than the propellant consumption during a single NSSK manoeuvre. The 10 year fuel budget for EWSK can be linearly approximated to be 2.705 kg.

As mentioned earlier the initial mass (Equation (7.7)) decreases after every manoeuvre but when the amount of propellant consumed is very small the initial mass difference does not make a huge difference to overall fuel budget calculation. The above performed analysis clearly shows that EWSK consumes far less fuel compared to NSSK.

The thrust impulse required for a EWSK manoeuvre is calculated using Equation (7.8). $\int F$ is calculated to be 69.7 Ns which translates to a 2 Newton thrust (combined thrust capability of two 1 Newton LPT's) being fired for approximately 35 seconds. Thus it is sufficient and possible to use LPT's to perform EWSK.

7.2.3 EWSK Thruster Placement

The placement of EWSK thrusters is highly dependent on the drift direction of the satellite. In the case where a satellite is placed at a nominal longitude of 19.5° East, it tends to drift towards the nearest stable point C (Figure 7.2) which means the drift is towards the East. Hence the thrusters must be placed such that the thrust takes the satellite westwards. For a GEO satellite a thruster can generate a west drift only if it is placed on the facet in the velocity direction ($+X_B$ facet). As shown in Figure 4.3 and Table 4.1 the thrusters used for EWSK are also used for fine attitude control. Since these thrusters are placed away form the centre of mass, firing any one of them alone will generate a parasitic torque. Therefore two LPTs have to be fired simultaneously for the exact required duration. Firing LPTs (5 and 6) or (3 and 4) generates the same effect thereby providing the required redundancy.

7.3 Attitude control while Station-keeping

It is practically impossible to mount a thruster through the exact centre of mass. Also as the propellant gets used, the centre of mass of the satellite tends to change. Due to these reasons firing of station-keeping thrusters leads to torques which can destabilise the attitude thereby affecting communication. Therefore it is mandatory that additional attitude control needs to be performed while station-keeping.

7.3.1 Attitude control while NSSK

The 10N HPT, if misaligned from the centre of mass by 1 cm, upon firing will generate a torque of 0.1 Nm. Considering the misalignment to be along the $+Z_B$ facet and since the thrust vector is along the $+Y_B$ axis (Figure 4.3), the generated misalignment torque can be calculated in the vector form as,

$$\mathbf{T_{mis}} = \mathbf{r \, x \, F} = [0.0 \quad 0.0 \quad 0.01]^T \text{ m} \times [0.0 \ 10.0 \ 0.0]^T \text{ N}$$
$$= [-0.1 \quad 0.0 \quad 0.0]^T \text{ Nm}$$

In order to cancel out the misalignment torque an equal but opposite torque needs to be generated which is called the compensating torque. This can be done by firing LPT 2 in Figure 5.6 for the same amount of time that the HPT is fired. The thrust vector from LPT 2 is in the direction of the $+Z_B$ facet and since the displacement of LPT 2 is along the $+Y_B$ axis, the compensating torque is calculated to be,

$$\mathbf{T_{comp}} = \mathbf{r \, x \, F} = [0.0 \quad 0.10 \quad 0.0]^T \text{ m} \times [0.0 \quad 0.0 \quad 1.0]^T \text{ N}$$
$$= [0.1 \quad 0.0 \quad 0.0]^T \text{ Nm}$$

Thus an equivalent but opposite torque is generated to counteract the misalignment torque. Figure 7.3 shows the attitude of the satellite with and without disturbance compensation. Figure 7.3(a) shows the disturbance along the X-axis when no compensation is done. The thruster is fired at time instant 200 seconds for 535 seconds (duration of NSSK manoeuvre). Once the thruster is switched off the satellite's attitude is stabilised by the feedback controllers.
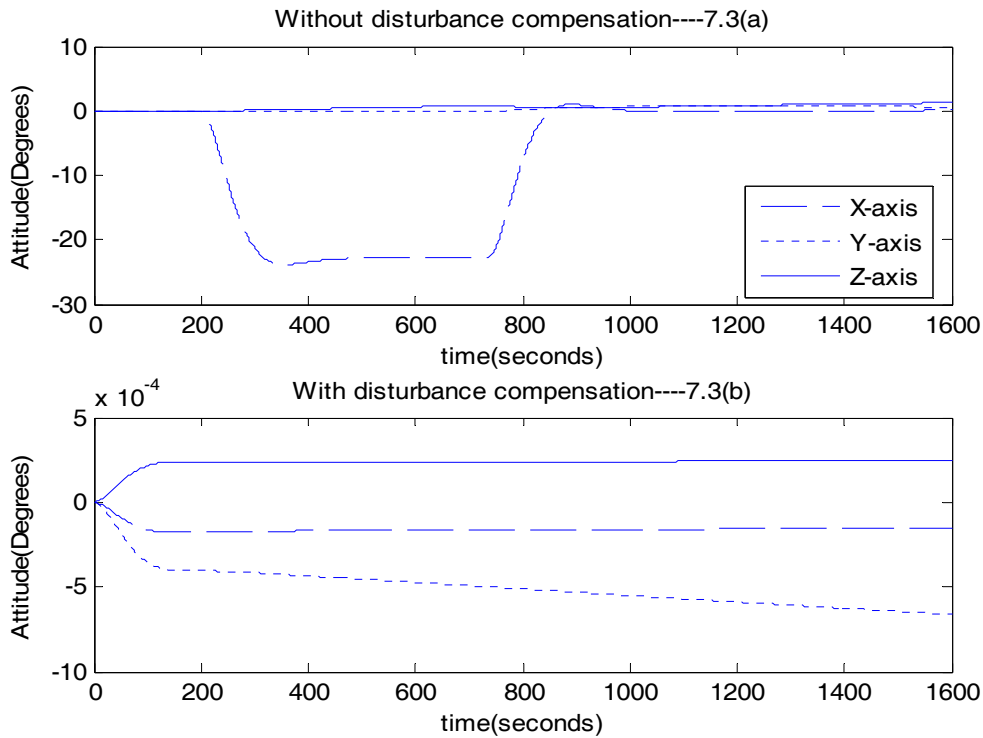
Figure 7.3 Effect of compensation torque on satellite attitude during NSSK

As expected the attitude disturbances in Figure 7.3(b) is due to the solar radiation torque shown in Figure 5.1.

The drawback of this process is the additional propellant being expelled while performing the compensations. The amount of propellant required to perform compensation can be determined from the firing duration of LPT 2. Since LPT 2 has a 1 Newton thrust being fired for 535 seconds, the thrust impulse will be 535 Nsec. Using Equation (7.8) the amount of propellant consumed is calculated to be 0.188 kg. If four compensation firings are done in a year over a 10 year period it would require an additional 7.52 kg of propellant. Normal reaction wheel feedback controllers are used simultaneously to provide fine attitude control.

It is also possible to provide a compensating torque using reaction wheels depending on the wheel's maximum momentum level. Since a large torque is required for a long period (0.1 Newton for 535 seconds) to perform NSSK misalignment compensation, the maximum momentum required will be 53.5 Nms. This momentum level cannot be achieved by the wheel being used in this simulation study which has a momentum saturation of 4 Nms. The compensation using reaction wheels will be discussed in the next section.

7.3.2 Attitude control while EWSK

The first step is so to determine the misalignment torque generated while performing EWSK. As mentioned in section 7.1.3 either LPTs 5 and 6 or LPTs 3 and 4 are used to perform EWSK. It so happens that the combined thrust vector could be off-centred from the centre of mass thereby generating the misalignment torque. It can be seen from Figure 4.3 and Figure 5.6 and Section 7.2.2 that firing the combination of LPTs used for EWSK generates a 2 Newton thrust vector along the $-X_B$ facet. For a misalignment of 1 cm along the $+Y_B$ and $+Z_B$ axes the misalignment torque is,

$$\mathbf{T_{mis}} = \mathbf{r \, x \, F} = [0.0 \quad 0.01 \quad 0.01]^T \text{ m } \times [-2.0 \quad 0.0 \quad 0.0]^T \text{ N}$$
$$= [0.0 \quad -0.02 \quad 0.02]^T \text{ Nm}$$

The next step would be to see if this torque can be compensated using the reaction wheels. A 0.02 Nm torque for a period of 35 seconds (duration of EWSK manoeuvre) leads to a maximum angular momentum requirement of 0.70 Nms which can be easily achieved by the reaction wheels used in the satellite. This means that the momentum wheel has to supply a wheel torque of 0.02 Nm for 35 seconds by linearly increasing its angular momentum from 0 to 0.70 Nms in 35 seconds. Increase in angular momentum is achieved by increasing the angular velocity of the wheel (integral of Equation (5.1)). The increase in angular velocity is dependent on the wheel inertia.

The required compensation torque thus happens to be $\mathbf{T_{comp}} = [0.0 \quad 0.02 \quad -0.02]^T \text{ Nm}$. Therefore the Y and Z wheels are used to generate the required compensating torques. The momentum vector of the reaction wheels and the wheel torques are shown in Figure 7.4.

The EWSK thrusters are fired at the time instant 250 seconds for a duration of 35 seconds. Simultaneously the Y and Z wheel momentums are increased linearly so that it reaches 0.7 Nms within 35 seconds. This increase in wheel momentum generates the required torques for the needed duration. Even though the wheel torques have an opposite direction to the required compensation torque, the torques applied to the satellite are opposite in direction to the wheel torques. This is better stated by the relation (from Equation (5.3)),

$$-\mathbf{T_{wheel}} = \mathbf{T_{control}} = \mathbf{T_{comp}}$$
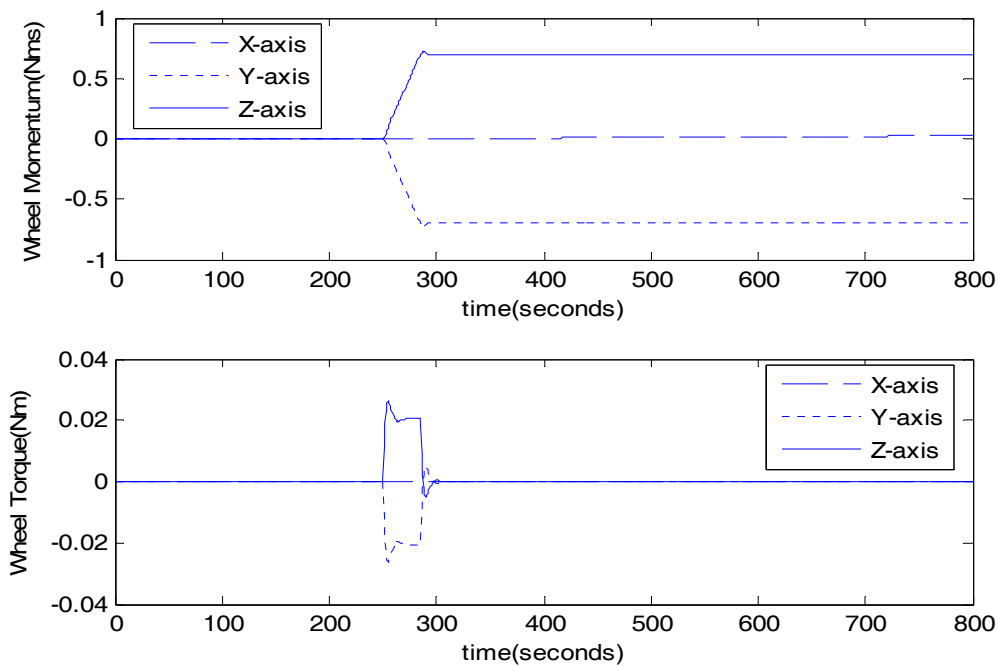
Figure 7.4 Wheel momentum Vs wheel torques during EWSK compensation

The overshoot in the wheel torque is due to the dynamics of the wheel speed controllers. The momentum build-up on the wheels are dumped using magnetic rods, once the momentum levels reach 0.7 Nms.
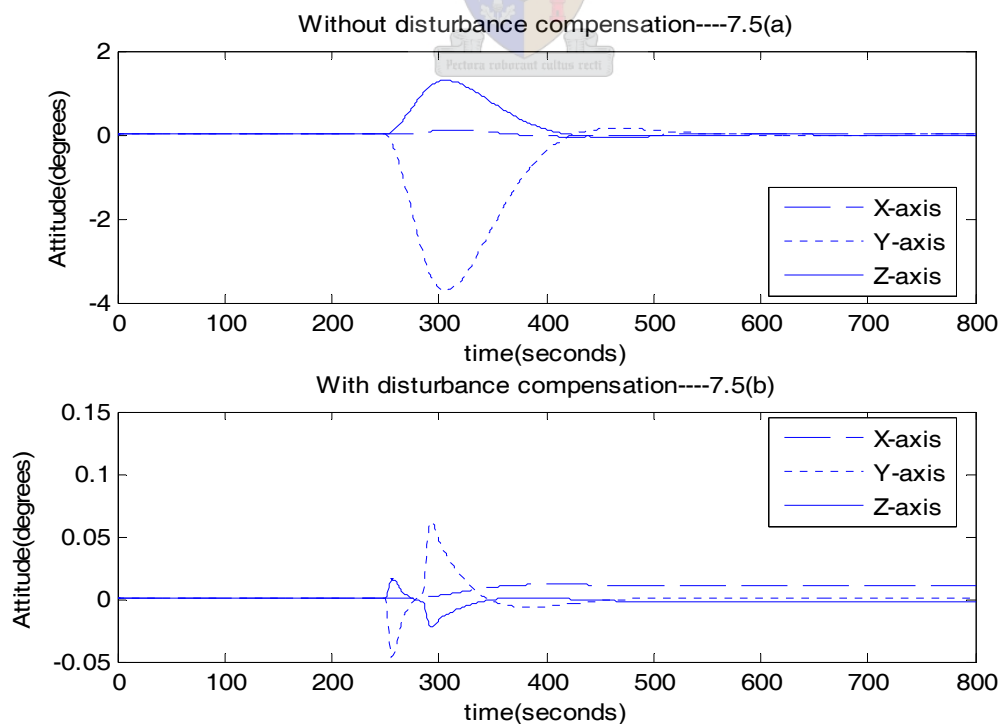
Figure 7.5 Effect of compensation torque on satellite attitude during EWSK

The dumping effect cannot be seen in Figure 7.4 because magnetic momentum dumping is a slow process (Section 5.2) and it takes almost 2 orbit periods to completely dump the momentum.   The attitude of the satellite with and without disturbance compensation is shown in Figure 7.5. The larger disturbance along the Y-axis in Figure 7.5(b) is due to the lower moment of inertia along the Y-axis. In spite of this the attitude is well within the required accuracy limit.

7.4 Summary

Factors which caused the satellite to drift from its nominal assigned position need was compensated using thrusters. The drift of the satellite also depends on where the satellite is stationed. NSSK consumes more propellant as compared to EWSK. Open loop control techniques were performed to cancel out the torques generated due to thruster misalignments. This is essential to keep the satellite within the required accuracy limits.
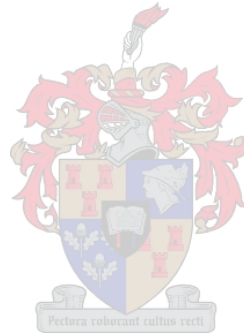
Chapter 8

Conclusion

8.1 Summary

Different control algorithms were presented in Chapter 5 which performs all the basic control functions for a GEO satellite in mission mode. Three axis control techniques which employed reaction wheels exclusively, were found to provide accuracies close to $0.005°$. A trade-off analysis between the controller specifications and the actuator capability was performed and the best solution was implemented. Momentum dumping using magnetic torque rods was performed to control the excessive momentum build-up. It was seen that the momentum levels on the X and Z axis wheels could be dumped to less than 0.1 Nms from an initial value of 0.4 Nms, within 1.5 orbits using torque rods of 75 Am^2. This was found to be extremely satisfactory considering the weak and near constant magnetic field of the Earth at GEO altitude. Momentum bias control was performed to evaluate the performance of the ADCS using only an Earth sensor. Even though the accuracy was less than a reaction wheel control system, it was well within the requirements. Finally a reaction thruster control system was implemented and analysed. The aim of this control system is to provide three axis control during station-keeping.

Attitude determination was performed in Chapter 6 to estimate attitude and body angular rates from sensor data. Two separate EKFs were discussed, each performing a specific task. The first EKF estimates quaternion attitude along with the body angular rates. The second EKF which is also called the MEKF, makes use of FOG measurements thereby eliminating the need to estimate the angular rates. However, the MEKF estimates the bias vector on the FOGs along with the quaternion attitude. From simulations it was seen that the RMS error of the estimated attitude ($0.04°$) using the first EKF was at least twice as compared to the error of the MEKF. The filters were also tested with initial attitude values and found to have a convergence time of less than 45 minutes for the estimated attitude.

An analytical station-keeping study was performed in Chapter 7. The frequency of station-keeping manoeuvres in both the East-west and North-south plane was calculated for a satellite with sub-satellite point similar to Astra 1B. It was found that to perform NSSK and EWSK for ten years, approximately 75 kg and 2.7 kg of propellant was required respectively. Finally attitude compensation to overcome thruster misalignment during NSSK required an additional 7.52 kg of propellant. However attitude compensation during EWSK was performed using reaction wheels and torque rods thereby avoiding propellant expenditure.

8.2 Recommendations

There are several possible ways in which the evaluation of the overall performance of the GEO satellite AODCS system can be improved. A simple but important method is to model the sensors more accurately. A star tracker can be included into the sensor system to improve the accuracy of the overall system. Also the GEO satellite AODCS can be equipped with additional control algorithms to enhance the performance. One possible method is to implement a tetrahedral reaction wheel configuration which provides redundancy as well as control to all three axes using all four wheels. Another possible technique is to use two skewed momentum wheels to perform momentum bias control which provides three axis control (Sidi, 1997) thereby eliminating the need to use additional actuators like magnetic torque rods.

Momentum dumping can be performed using thrusters in order to minimise the momentum dumping time. However, since this method comes at the cost of additional propellant consumption, care must be taken to analyse the amount of propellant left to perform station-keeping operations. If the GEO satellite happens to have a payload which needs to be reoriented frequently, time optimal controllers can be used to minimise the manoeuvre time.

Finally, the air bearing table in the ESL at Stellenbosch University or any similar facility can be used to analyse thruster misalignment and implement feed forward compensation during station-keeping, along a single axis.

References

Berlin, P. 1988.

The Geostationary Applications Satellite. Cambridge Aerospace Series. Cambridg*e*: University Press.

Bijker, J. 2006.

Development of an Attitude Heading Reference System for an Airship, Masters Thesis, University of Stellenbosch, December 2006.

Engelbrecht, J.A.A. 1999.

A Hardware–In–The–Loop Simulation Facility For The Attitude Determination and Control Of   Sunsat, Masters Thesis, University of Stellenbosch, December 1999.

Lefferts E.J., Markley F.L and M.D. Shuster. 1982.

"Kalman Filter for Spacecraft Attitude Estimation", *Journal of Guidance, Control and Dynamics,* Vol 5, No.5, Sept.-Oct. 1982, pp.417-429.

Maral,G. and M. Bousquet. 1986.

Satellite Communications Systems. Chichester: John Wiley.

Markley, F.L. 2003.

"Attitude Error Representations for Kalman Filering", *Journal of Guidance, Control and Dynamics,* Vol 26, No.2, March-April 2003, pp.311-317.

Markley, F.L. 2004.

"Multiplicative vs. Additive Filtering for Spacecraft Attitude Determination", *Dynamics and Control of Systems and Structures in Space*, 6th Conference, July 2004, Riomaggiore, Italy.

Pocha, J.J. 1987.

An introduction to Mission Design for Geostationary Satellites. Space Technology Library Series. Dordrecht: D. Reidel Publishing Company.

Psiaki M.L., Martel F and P.K Pal. 1990

"Three-Axis Atttitude Determination via Kalman Filtering of Magnetometer Data", *Journal of Guidance, Control and Dynamics,* Vol. 13, No.3, May-June 1990, pp.506-514.

Sidi, M.J. 1997.

Spacecraft Dynamics and Control: A practical engineering approach. Cambridge Aerospace Series. Cambridge: University Press.

Steyn, W.H. 1995.

A Multi-mode Attitude Determination and Control System for Small Satellites, PhD Thesis, University of Stellenbosch, December 1995.

Steyn, W.H. 2004.

AODCS training, University of Stellenbosch, 2004. whsteyn@Sun.ac.za.

Wertz, J.R. 1978

Spacecraft Attitude Determination and Control. Dordrecht: Kluwer

Wertz, J.R. and W.J Larson. 1999.

Space Mission Analysis and Design. 3rd edition. Space Technology Library Series. El Segundo: Microcosm Press.

Wie, B, 1998.

Space Vehicle Dynamics and Control. AIAA Education Series. Reston: American Institute of Aeronautics and Astronautics, Inc.

Bibliography

Additional Books

Gelb A. 1989

Applied optimal Estimation, The Analytical Sciences Corporation, M.I.T Press, Eleventh Printing.

Franklin G.F., Powell J.D. and M.L. Workman. 1998

Digital Control of Dynamic Systems, 3rd Edition. California: Addison-Wesley Publishing Longman,Inc.

Websites

GEO satellite history:

http://www.boeing.com/defense-space/space/bss/factsheets/376/syncom/syncom.html

IGRF model verification:

http://swdcwww.kugi.kyoto-u.ac.jp/igrf/point/index.html

SDP4 orbit propagator:

http://www.amsat.org/amsat/ftp/docs/spacetrk.pdf

Sir Arthur. C. Clarke's pioneering paper:

http://www.arthur-c-clarke.de/extra-terrestrial-relays/wireless_world.htm

Thruster information:

http://cs.space.eads.net/sp/

Appendix A

Transformation Matrix and Momentum Biased Dynamics

A.1 Inertial to Orbit Coordinates Transformation matrix

The relation between the two coordinate systems is shown in Figure 2.4. The relations in the figure are better understood when described in an equational manner. To begin with it is most logical to describe the position ($\overline{pos}$) and velocity ($\overline{vel}$) unit vector components of the satellite in the inertial coordinates. The '$\overline{pos}$' and '$\overline{vel}$' vectors are obtained from the SDP4 orbit propagator or any other propagation model.

The '$\overline{pos}$' and '$\overline{vel}$' unit vectors in inertial coordinates are represented as,

$$\begin{aligned}
\overline{pos} &= P_x \bar{x}_I + P_y \bar{y}_I + P_z \bar{z}_I \\
\overline{vel} &= V_x \bar{x}_I + V_y \bar{y}_I + V_z \bar{z}_I
\end{aligned} \tag{A.1}$$

where,

$[P_x, P_y, P_z]$ = components of unit position vector of satellite in inertial coordinates

$[V_x, V_y, V_z]$ = components of unit velocity vector of satellite in inertial coordinates

$[\bar{x}_I, \bar{y}_I, \bar{z}_I]$ = unit vectors in inertial coordinates

From Figure 2.4 one can deduce the following relations,

$$\begin{aligned}
\bar{z}_O &= -\overline{pos} \\
\bar{y}_O &= \overline{vel} \times \overline{pos} \\
\bar{x}_O &= \bar{y}_O \times \bar{z}_O
\end{aligned} \tag{A.2}$$

where,

$[\bar{x}_O, \bar{y}_O, \bar{z}_O]$ = unit vectors in the orbit coordinates

With these relations the directions of the orbit unit vectors can be expressed in terms of the '$\overline{pos}$' and '$\overline{vel}$' unit vectors.

Each orbit unit vector can be individually expressed as,

$$\bar{z}_O = -(P_x \bar{x}_I + P_y \bar{y}_I + P_z \bar{z}_I) \tag{A.3}$$

$$
\begin{aligned}
\bar{y}_O &= \overline{vel} \times \overline{pos} \\
&= (V_x \bar{x}_I + V_y \bar{y}_I + V_z \bar{z}_I) \times (P_x \bar{x}_I + P_y \bar{y}_I + P_z \bar{z}_I) \\
&= (V_y P_z - V_z P_y)\bar{x}_I + (V_z P_x - V_x P_z)\bar{y}_I + (V_x P_y - V_y P_x)\bar{z}_I \\
&= W_x \bar{x}_I + W_y \bar{y}_I + W_z \bar{z}_I
\end{aligned} \tag{A.4}
$$

$$
\begin{aligned}
\bar{x}_O &= \bar{y}_O \times \bar{z}_O \\
&= (W_x \bar{x}_I + W_y \bar{y}_I + W_z \bar{z}_I) \times (-P_x \bar{x}_I - P_y \bar{y}_I - P_z \bar{z}_I) \\
&= (W_z P_y - W_y P_z)\bar{x}_I + (W_x P_z - W_z P_x)\bar{y}_I + (W_y P_x - W_x P_y)\bar{z}_I \\
&= A_x \bar{x}_I + A_y \bar{y}_I + A_z \bar{z}_I
\end{aligned} \tag{A.5}
$$

Equations (A.3), (A.4) and (A.5) can now be expressed in the matrix form as,

$$[\bar{x}_O \ \bar{y}_O \ \bar{z}_O]^T = [\mathbf{T}][\bar{x}_I \ \bar{y}_I \ \bar{z}_I]^T \tag{A.6}$$

where,

$$[\mathbf{T}] = \begin{bmatrix} A_x & A_y & A_z \\ W_x & W_y & W_z \\ -P_x & -P_y & -P_z \end{bmatrix} \tag{A.7}$$

Substituting Equation (A.7) into (A.6) we get,

$$\begin{bmatrix} \bar{x}_O \\ \bar{y}_O \\ \bar{z}_O \end{bmatrix} = \begin{bmatrix} A_x & A_y & A_z \\ W_x & W_y & W_z \\ -P_x & -P_y & -P_z \end{bmatrix} \begin{bmatrix} \bar{x}_I \\ \bar{y}_I \\ \bar{z}_I \end{bmatrix} \tag{A.8}$$

Thus it can be seen that a vector which is expressed in terms of the unit vector in the inertial coordinates can be transformed to a unit vector expressed in the orbit coordinates.

A.2 Analysis of a Momentum Biased Satellite

The momentum biased satellite which is discussed in Section 5.3 makes use of Equation (5.21) which is the dynamic equation of motion for a momentum biased satellite.

A.2.1 Dynamic Equations of a Momentum Biased Satellite

The equations of motion for a momentum biased satellite are derived from the general dynamic equation of motion mentioned in Equation (2.8) which can also be rewritten as,

$$\mathbf{I_I}\dot{\boldsymbol{\omega}}_B^I = \mathbf{T_D} + \mathbf{T_C} - \boldsymbol{\omega}_B^I \times (\mathbf{I}\boldsymbol{\omega}_B^I + \mathbf{h_w}) - \dot{\mathbf{h}}_\mathbf{w} \tag{A.9}$$

where,

$$\mathbf{T_C} = \mathbf{T_M} + \mathbf{T_T} \tag{A.10}$$

Equation (A.9) can be written in terms of the components of the inertial body angular rates as,

$$\dot{\omega}_{ix} = \frac{T_{DX} + T_{CX} + [I_{YY} - I_{ZZ}]\omega_{iy}\omega_{iz} - \omega_{iy}h_{wz} + \omega_{iz}h_{wy} - \dot{h}_{wx}}{I_{XX}}$$

$$\dot{\omega}_{iy} = \frac{T_{DY} + T_{CY} + [I_{ZZ} - I_{XX}]\omega_{iz}\omega_{ix} - \omega_{iz}h_{wx} + \omega_{ix}h_{wz} - \dot{h}_{wy}}{I_{YY}} \tag{A.11}$$

$$\dot{\omega}_{iz} = \frac{T_{DZ} + T_{CZ} + [I_{XX} - I_{YY}]\omega_{ix}\omega_{iy} - \omega_{ix}h_{wy} + \omega_{iy}h_{wx} - \dot{h}_{wz}}{I_{ZZ}}$$

Since the momentum biased satellite has only the Y-wheel in it, terms h_{wx} and h_{wz} become zero. Equation (A.11) gets modified to,

$$\dot{\omega}_{ix} = \frac{T_{DX} + T_{CX} + [I_{YY} - I_{ZZ}]\omega_{iy}\omega_{iz} + \omega_{iz}h_{wy}}{I_{XX}}$$

$$\dot{\omega}_{iy} = \frac{T_{DY} + T_{CY} + [I_{ZZ} - I_{XX}]\omega_{iz}\omega_{ix} - \dot{h}_{wy}}{I_{YY}} \tag{A.12}$$

$$\dot{\omega}_{iz} = \frac{T_{DZ} + T_{CZ} + [I_{XX} - I_{YY}]\omega_{ix}\omega_{iy} - \omega_{ix}h_{wy}}{I_{ZZ}}$$

Before proceeding further it is important to state a few assumptions that are required in the derivation. Equation (2.11) can be rearranged as,

$$\boldsymbol{\omega}_B^I = \boldsymbol{\omega}_B^O - \mathbf{A} \begin{bmatrix} 0 \\ \omega_o \\ 0 \end{bmatrix} \tag{A.13}$$

where, $\tilde{\omega}_o(t) = \omega_o$ for a GEO satellite.

The DCM matrix [**A**] in Equation (2.1) for small Euler angles becomes,

$$\mathbf{A} = \begin{bmatrix} 1 & \psi & -\theta \\ -\psi & 1 & \phi \\ \theta & -\phi & 1 \end{bmatrix} \tag{A.14}$$

Therefore Equation (A.13) becomes,

$$\boldsymbol{\omega}_B^I = \boldsymbol{\omega}_B^O + \begin{bmatrix} -\psi\omega_o \\ -\omega_o \\ \phi\omega_o \end{bmatrix} \tag{A.15}$$

$\boldsymbol{\omega}_B^O = [\omega_{ox} \ \omega_{oy} \ \omega_{oz}]^T = [\dot{\phi} \ \dot{\theta} \ \dot{\psi}]^T$ for small angles.

Equation (A.15) gets rewritten as,

$$\boldsymbol{\omega}_B^I = \begin{bmatrix} \dot{\phi} - \psi\omega_o \\ \dot{\theta} - \omega_o \\ \dot{\psi} + \phi\omega_o \end{bmatrix} \tag{A.16}$$

Finally, by differentiating Equation (A.16) we get,

$$\dot{\boldsymbol{\omega}}_B^I = \begin{bmatrix} \dot{\omega}_{ix} \\ \dot{\omega}_{iy} \\ \dot{\omega}_{iz} \end{bmatrix} = \begin{bmatrix} \ddot{\phi} - \dot{\psi}\omega_o \\ \ddot{\theta} \\ \ddot{\psi} + \dot{\phi}\omega_o \end{bmatrix} \tag{A.17}$$

The dynamic equations can be derived now. Equation (A.12) can be rewritten with the help of Equations (A.16) and (A.17) as,

$$I_{XX}(\ddot{\phi} - \dot{\psi}\omega_o) = T_{DX} + T_{CX} + [I_{YY} - I_{ZZ}](\dot{\theta} - \omega_o)(\dot{\psi} + \phi\omega_o) + (\dot{\psi} + \phi\omega_o)h_{wy} \tag{A.18}$$

$$I_{YY}(\ddot{\theta}) = T_{DY} + T_{CY} + [I_{ZZ} - I_{XX}](\dot{\psi} + \phi\omega_o)(\dot{\phi} - \psi\omega_o) - \dot{h}_{wy} \tag{A.19}$$

$$I_{ZZ}(\ddot{\psi} + \dot{\phi}\omega_o) = T_{DZ} + T_{CZ} + [I_{XX} - I_{YY}](\dot{\phi} - \psi\omega_o)(\dot{\theta} - \omega_o) - (\dot{\phi} - \psi\omega_o)h_{wy} \tag{A.20}$$

The analysis of Equations (A.18) and (A.20) are similar therefore only one of them will be analysed here. In Equation (A.18) the terms which include 'ω_o' and those which include the inertia difference '$I_{YY} - I_{ZZ}$' are ignored because they happen to be much lesser than the terms which include the wheel momentum 'h_{wy}'. This is because $\omega_o \approx 7.3 \times 10^{-5}$ rad/sec for a GEO satellite. Equation (A.18) becomes,

$$T_{DX} + T_{CX} = I_{XX}(\ddot{\phi}) - h_{wy}\dot{\psi} - h_{wy}\phi\omega_o \qquad\qquad\text{(A.21)}$$

Similarly Equation (A.20) becomes,

$$T_{DZ} + T_{CZ} = I_{ZZ}(\ddot{\psi}) + h_{wy}\dot{\phi} - h_{wy}\psi\omega_o \qquad\qquad\text{(A.22)}$$

Equation (A.19) is different in the sense that it contains a wheel torque along this axis and gets simplified to,

$$T_{DY} + T_{CY} = I_{YY}(\ddot{\theta}) + \dot{h}_{wy} \qquad\qquad\text{(A.23)}$$

It can be seen that when Equations (A.21), (A.22) and (A.23) are combined they form the components of Equation (5.21) which is the dynamic equation for a momentum biased GEO satellite.
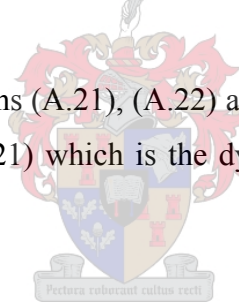
A.2.2 Derivation of Steady state Equations

This section derives the steady state equations (Equations (5.31) and (5.32)) from Equation (5.28). Equation (5.28) can be expanded to give the following equations.

$$\phi(s) = \frac{\left[s^2 + \dfrac{1}{I_{ZZ}}(k_{PZ} + sk_{DZ} - \omega_o h_{wy})\right] \times \dfrac{T_{DX}(s)}{I_{XX}}}{\Delta(s)} + \frac{\left(\dfrac{sh_{wy}}{I_{XX}}\right) \times \dfrac{T_{DZ}(s)}{I_{ZZ}}}{\Delta(s)} \qquad\text{(A.24)}$$

$$\psi(s) = \frac{\left(-\dfrac{sh_{wy}}{I_{ZZ}}\right) \times \dfrac{T_{DX}(s)}{I_{XX}}}{\Delta(s)} + \frac{\left[s^2 + \dfrac{1}{I_{XX}}(k_{PX} + sk_{DX} - \omega_o h_{wy})\right] \times \dfrac{T_{DZ}(s)}{I_{ZZ}}}{\Delta(s)} \qquad\text{(A.25)}$$

where, $\Delta(s)$ is same as Equation (5.30).

From the final value theorem we know that,

$$\phi_{SS} = \lim_{s \to 0} s\phi(s) \quad \text{and} \quad \psi_{SS} = \lim_{s \to 0} s\psi(s) \tag{A.26}$$

Also,

$$T_{DX}(s) = \frac{T_{DX}}{s} \quad \text{and} \quad T_{DZ}(s) = \frac{T_{DZ}}{s} \tag{A.27}$$

Substituting Equations (A.24) and (A.25) along with (A.27) into Equation (A.26) we get,

$$\phi_{SS} = \lim_{s \to 0} \frac{\left[\dfrac{I_{ZZ}s^3 + s(k_{PZ} + sk_{DZ} - \omega_o h_{wy})}{I_{XX}I_{ZZ}} \right] \dfrac{T_{DX}}{s} + \left[\dfrac{s^2 h_{wy} T_{DZ}}{sI_{XX}I_{ZZ}} \right]}{\Delta(s)} \tag{A.28}$$

$$\psi_{SS} = \lim_{s \to 0} \frac{\left[\dfrac{-s^2 h_{wy} T_{DX}}{sI_{XX}I_{ZZ}} \right] + \left[\dfrac{I_{ZZ}s^3 + s(k_{PX} + sk_{DX} - \omega_o h_{wy})}{I_{XX}I_{ZZ}} \right] \times \dfrac{T_{DZ}}{s}}{\Delta(s)} \tag{A.29}$$

By applying the limits to $\Delta(s)$ also and by performing the necessary simplification, Equations (A.28) and (A.29) become,

$$\phi_{SS} = \frac{(k_{PZ} + \omega_o h)T_{DX}}{k_{PX}k_{PZ} + (\omega_o h)^2 + \omega_o h(k_{PX}k_{PZ})}$$

$$\psi_{SS} = \frac{(k_{PX} + \omega_o h)T_{DZ}}{k_{PX}k_{PZ} + (\omega_o h)^2 + \omega_o h(k_{PX}k_{PZ})}$$

which are the steady state Equations (5.31) and (5.32).

APPENDIX B

Attitude Definitions and Quaternion Operations

B.1 DCM Computation

In Figure 2.7, it has been shown that the combination of three successive rotations leads to the DCM matrix which is expressed in terms of the Euler angles. For an Euler 2-1-3 rotation the first rotation which is along the pitch axis is represented as $(\cos(\text{angle}) = \text{cangle}$ and $\sin(\text{angle}) = \text{sangle})$,

$$\begin{bmatrix} X^{'} \\ Y^{'} \\ Z^{'} \end{bmatrix} = \begin{bmatrix} c\theta & 0 & -s\theta \\ 0 & 1 & 0 \\ s\theta & 0 & c\theta \end{bmatrix} \begin{bmatrix} X_O \\ Y_O \\ Z_O \end{bmatrix} \tag{B.1}$$

The next rotation which is along the roll axis is expressed as,

$$\begin{bmatrix} X^{''} \\ Y^{''} \\ Z^{''} \end{bmatrix} = \begin{bmatrix} 1 & 0 & 0 \\ 0 & c\phi & s\phi \\ 0 & -s\phi & c\phi \end{bmatrix} \begin{bmatrix} X^{'} \\ Y^{'} \\ Z^{'} \end{bmatrix} \tag{B.2}$$

And finally the yaw rotation is represented as,

$$\begin{bmatrix} X_B \\ Y_B \\ Z_B \end{bmatrix} = \begin{bmatrix} X^{'''} \\ Y^{'''} \\ Z^{'''} \end{bmatrix} = \begin{bmatrix} c\psi & s\psi & 0 \\ -s\psi & c\psi & 0 \\ 0 & 0 & 1 \end{bmatrix} \begin{bmatrix} X^{''} \\ Y^{''} \\ Z^{''} \end{bmatrix} \tag{B.3}$$

By combining the three rotations, a vector in the orbit coordinates can be transformed to the body coordinates.

$$\begin{bmatrix} X_B \\ Y_B \\ Z_B \end{bmatrix} = \begin{bmatrix} c\psi & s\psi & 0 \\ -s\psi & c\psi & 0 \\ 0 & 0 & 1 \end{bmatrix} \begin{bmatrix} 1 & 0 & 0 \\ 0 & c\phi & s\phi \\ 0 & -s\phi & c\phi \end{bmatrix} \begin{bmatrix} c\theta & 0 & -s\theta \\ 0 & 1 & 0 \\ s\theta & 0 & c\theta \end{bmatrix} \begin{bmatrix} X_O \\ Y_O \\ Z_O \end{bmatrix} \tag{B.4}$$

Performing the matrix multiplications in the correct order (left to right) on the left hand side of Equation (B.4) we obtain the DCM matrix as shown in Equation (2.1).

116

Equation (2.6) which calculates the Euler angles from the DCM matrix is repeated here for simplicity.

$$(\text{Roll})\phi = \operatorname{asin}(-a_{32}), \ (\text{Pitch})\theta = \operatorname{atan2}(a_{31}/a_{33}), \ (\text{Yaw})\psi = \operatorname{atan2}(a_{12}/a_{22})$$

It is possible that we could encounter discontinuities in Pitch and Yaw angles when terms a_{33} and a_{22} are zero.

However the exists an alternative representation which makes use of a single rotation (Φ) along an axis called the Euler axis of rotation which is defined by the Euler axis vector (**e**) where,

$$\mathbf{e} = [e_x \quad e_y \quad e_z]^T. \ (\text{Similar to description on Page.14})$$

Φ = rotation angle around Euler axis

An analysis of Equations (B.1),(B.2) and (B.3) shows that the trace of the matrices are equal and is shown to be,

$$\operatorname{trace}[\mathbf{A}_\Phi] = [1 + 2\cos\Phi] \tag{B.5}$$

The attitude matrix in terms of the Euler axis and Euler angle which satisfies the condition in Equation (B.5) can be expressed as,

$$[\mathbf{A}_\Phi] = \cos(\Phi)\mathbf{I} + [1 - \cos(\Phi)]\mathbf{e}\mathbf{e}^T - \sin(\Phi)[\mathbf{E}] \tag{B.6}$$

where,

$$[\mathbf{E}] = \begin{bmatrix} 0 & -e_z & e_y \\ e_z & 0 & -e_x \\ -e_y & e_x & 0 \end{bmatrix}$$

Equation (B.6) thus becomes,

$$[\mathbf{A}_\Phi] = \begin{bmatrix} c\Phi + e_x^2(1-c\Phi) & e_x e_y(1-c\Phi) + e_z s\Phi & e_x e_z(1-c\Phi) - e_y s\Phi \\ e_x e_y(1-c\Phi) - e_z s\Phi & c\Phi + e_y^2(1-c\Phi) & e_y e_z(1-c\Phi) + e_x s\Phi \\ e_x e_z(1-c\Phi) + e_y s\Phi & e_y e_z(1-c\Phi) - e_x s\Phi & c\Phi + e_z^2(1-c\Phi) \end{bmatrix} \tag{B.7}$$

Equation (B.7) is another representation of the DCM matrix. The Euler axis vector components and the Euler angle can be calculated from the DCM matrix in the following manner:

$$\Phi = \cos^{-1}\left[\frac{1}{2}(\text{trace}[\mathbf{A}_\Phi]-1)\right] \tag{B.8}$$

and

$$\begin{aligned}
e_x &= [a_{23} - a_{32}]/[2\sin(\Phi)] \\
e_y &= [a_{31} - a_{13}]/[2\sin(\Phi)] \\
e_z &= [a_{12} - a_{21}]/[2\sin(\Phi)]
\end{aligned} \tag{B.9}$$

However we tend to have discontinuities while calculating the Euler axis components when $\sin(\Phi) = 0$. Another possible representation of the DCM is in terms of the Euler symmetric parameters called the quaternions which are discussed as in Equation (2.2). The quaternion DCM is derived by equating the relations from Equation 2.2 into Equation (B.7) and can be represented as,

$$[\mathbf{A}(\mathbf{q})] = (q_4^2 - \mathbf{q}^2)\mathbf{I} + 2\mathbf{q}\mathbf{q}^T - 2q_4[\mathbf{Q}] \tag{B.10}$$

where,

$$[\mathbf{Q}] = \begin{bmatrix} 0 & -q_3 & q_2 \\ q_3 & 0 & -q_1 \\ -q_2 & q_1 & 0 \end{bmatrix}$$
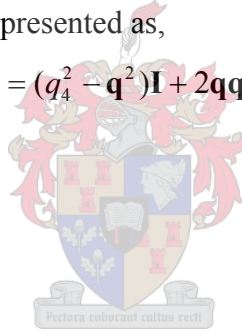
Equation (B.10) on expansion gives us the DCM in Equation (2.4). The popularity of the quaternion DCM arises from the fact that it does not have any trigonometric terms which could lead to discontinuities.

Equation (2.5) calculates the individual quaternion elements when q_4 is the largest. The alternative calculations using the largest corresponding pivot elements are,

$$\begin{aligned}
q_1 &= 0.5[1 + a_{11} - a_{22} - a_{33}]^{0.5}, \\
q_2 &= \frac{0.25}{q_1}[a_{12} + a_{21}], \quad q_3 = \frac{0.25}{q_1}[a_{13} + a_{31}], \quad q_4 = \frac{0.25}{q_1}[a_{23} + a_{32}]
\end{aligned} \tag{B.11}$$

$$q_2 = 0.5[1 - a_{11} + a_{22} - a_{33}]^{0.5},$$

$$q_1 = \frac{0.25}{q_3}[a_{12} + a_{21}], \quad q_3 = \frac{0.25}{q_2}[a_{23} + a_{32}], \quad q_4 = \frac{0.25}{q_2}[a_{31} - a_{13}]$$

(B.12)

$$q_3 = 0.5[1 - a_{11} - a_{22} + a_{33}]^{0.5},$$

$$q_1 = \frac{0.25}{q_3}[a_{13} + a_{31}], \quad q_2 = \frac{0.25}{q_3}[a_{23} + a_{32}], \quad q_4 = \frac{0.25}{q_3}[a_{12} + a_{21}]$$

(B.13)

B.2 Calculation of Attitude rates

A very important aspect that needs to be discussed is the attitude rate calculation of the satellite. Here we will look at the different possible ways of calculating the attitude rates from the body angular rates of the satellite. Sidi (1997, p102) has a discussion along the same lines for an Euler 3-2-1 rotation sequence.

The first method is to calculate the attitude rate using the Euler angle DCM matrix. Depending on the type of rotation used in the DCM the body angular rates can be related to the attitude rates. Since we use an Euler 2-1-3 rotation the pitch rate is multiplied by the complete DCM and is shown to be,

$$\begin{bmatrix} 0 \\ \omega_{oy} \\ 0 \end{bmatrix} = \begin{bmatrix} c\psi\,c\theta + s\psi\,s\phi\,s\theta & s\psi\,c\phi & -c\psi\,s\theta + s\psi\,s\phi\,c\theta \\ -s\psi\,c\theta + c\psi\,s\phi\,s\theta & c\psi\,c\phi & s\psi\,s\theta + c\psi\,s\phi\,c\theta \\ c\phi\,s\theta & -s\phi & c\phi\,c\theta \end{bmatrix} \begin{bmatrix} 0 \\ \dot{\theta} \\ 0 \end{bmatrix}$$

(B.14)

Next the roll rate is multiplied by the product of the [3x3] matrices in Equations (B.3) and (B.2) (product of yaw and roll rotation).

$$\begin{bmatrix} \omega_{ox} \\ 0 \\ 0 \end{bmatrix} = \begin{bmatrix} c\psi & s\psi\,c\phi & s\psi\,s\phi \\ -s\psi & c\psi\,c\phi & c\psi\,s\phi \\ 0 & -s\phi & c\phi \end{bmatrix} \begin{bmatrix} \dot{\phi} \\ 0 \\ 0 \end{bmatrix}$$

(B.15)

And finally yaw rate is multiplied by the yaw rotation matrix.

$$\begin{bmatrix} 0 \\ 0 \\ \omega_{oz} \end{bmatrix} = \begin{bmatrix} c\psi & s\psi & 0 \\ -s\psi & c\psi & 0 \\ 0 & 0 & 1 \end{bmatrix} \begin{bmatrix} 0 \\ 0 \\ \dot{\psi} \end{bmatrix}$$

(B.16)

Adding Equations (B.14), (B.15) and (B.16) after performing the respective matrix multiplications give us,

$$
\begin{bmatrix} \omega_{ox} \\ \omega_{oy} \\ \omega_{oz} \end{bmatrix} = \begin{bmatrix} c\psi & s\psi\,c\phi & 0 \\ -s\psi & c\psi\,c\phi & 0 \\ 0 & -s\phi & 1 \end{bmatrix} \begin{bmatrix} \dot{\phi} \\ \dot{\theta} \\ \dot{\psi} \end{bmatrix}
\tag{B.17}
$$

Now the attitude rates can be obtained from the body angular rates using the inverse of Equation (B.17).

$$
\begin{bmatrix} \dot{\phi} \\ \dot{\theta} \\ \dot{\psi} \end{bmatrix} = \frac{1}{\cos\phi} \begin{bmatrix} \cos\psi\cos\phi & \sin\psi\cos\phi & 0 \\ \sin\psi & \cos\psi & 0 \\ \sin\psi\sin\phi & \cos\psi\sin\phi & \cos\phi \end{bmatrix} \begin{bmatrix} \omega_{ox} \\ \omega_{oy} \\ \omega_{oz} \end{bmatrix}
\tag{B.18}
$$

Equation (B.18) can be rewritten as,

$$
\begin{bmatrix} \dot{\phi} \\ \dot{\theta} \\ \dot{\psi} \end{bmatrix} = \begin{bmatrix} \cos\psi & \sin\psi & 0 \\ \sin\psi\sec\phi & \cos\psi\sec\phi & 0 \\ \sin\psi\tan\phi & \cos\psi\tan\phi & 1 \end{bmatrix} \begin{bmatrix} \omega_{ox} \\ \omega_{oy} \\ \omega_{oz} \end{bmatrix}
\tag{B.19}
$$

which tends to have singularities when $\phi = 90°$ because of the presence of 'tan' and 'sec' functions.

The calculation of the attitude rates in terms of the Euler angle and Euler axis components are,

$$
\dot{\Phi} = \mathbf{e}^T \boldsymbol{\omega}_B^O
$$
$$
\dot{\mathbf{e}} = \frac{1}{2}\left[\mathbf{E} - \cot\frac{\Phi}{2}\mathbf{E}\mathbf{E} \right] \boldsymbol{\omega}_B^O
\tag{B.20}
$$

However we tend to have singularities when $\Phi = 0°$ or $360°$.

Equation (B.20) can be manipulated using Euler symmetric parameter representation which helps in representing the attitude rates in terms of the quaternions as,

$$
\dot{q} = \frac{1}{2}\begin{bmatrix} \mathbf{Q} + q_4\mathbf{I} \\ -\mathbf{q}^T \end{bmatrix} \boldsymbol{\omega}_B^O
\tag{B.21}
$$

Since this representation does not have any trigonometric functions, it does not suffer from any singularities. Equation (B.21) on expansion gives the kinematic equations which are described in Equation (2.9).

B.3 Quaternion Operations

B.3.1 Quaternion Division

Quaternion division is used to subtract two quaternions from each other. The reason for using quaternion division rather than subtraction is to prevent the scalar part of the difference quaternion approaching zero.

Quaternion division can be represented as,

$$\mathbf{q_{div}} = \mathbf{q} \Theta \mathbf{q_c} \tag{B.22}$$

where,

$$\mathbf{q} = iq_1 + jq_2 + kq_3 + q_4$$

$$\mathbf{q_c} = iq_{1c} + jq_{2c} + kq_{3c} + q_{4c}$$

Equation (B.22) then gets expressed as,

$$\begin{aligned}
\mathbf{q_{div}} &= q_4 q_{4c} + \mathbf{q_{vec}} \cdot \mathbf{q_{c,vec}} + q_{4c}\mathbf{q_{vec}} - q_4\mathbf{q_{c,vec}} + (\mathbf{q_{vec}} \times \mathbf{q_{c,vec}}) \\
&= \begin{bmatrix} q_{4c}\mathbf{q_{vec}} - q_4\mathbf{q_{c,vec}} + (\mathbf{q_{vec}} \times \mathbf{q_{c,vec}}) \\ q_4 q_{4c} + \mathbf{q_{vec}} \cdot \mathbf{q_{c,vec}} \end{bmatrix}
\end{aligned} \tag{B.23}$$

B.3.2 Quaternion multiplication

The normal (historical) method of quaternion multiplication is performed in the following manner:

$$\begin{aligned}
\mathbf{q_{mul}} &= \mathbf{q} \otimes \mathbf{q_c} \\
&= q_4 q_{4c} - \mathbf{q_{vec}} \cdot \mathbf{q_{c,vec}} + q_{4c}\mathbf{q_{vec}} + q_4\mathbf{q_{c,vec}} + (\mathbf{q_{vec}} \times \mathbf{q_{c,vec}}) \\
&= \begin{bmatrix} q_{4c}\mathbf{q_{vec}} + q_4\mathbf{q_{c,vec}} + (\mathbf{q_{vec}} \times \mathbf{q_{c,vec}}) \\ q_4 q_{4c} - \mathbf{q_{vec}} \cdot \mathbf{q_{c,vec}} \end{bmatrix}
\end{aligned} \tag{B.24}$$

However a unique quaternion multiplication is performed to satisfy the condition mentioned in Equation 6.59. To validate this further, if a matrix $\mathbf{A}[\,\mathbf{q_{mul}}\,]$ is expressed as $\mathbf{A}[\,\mathbf{q} \otimes \mathbf{q_c}\,]$ then according to Markley (2003) and Lefferts *et.al.* (1982),

$$\mathbf{A}[\,\mathbf{q}\,]\mathbf{A}[\,\mathbf{q_c}\,] = \mathbf{A}[\,\mathbf{q} \otimes \mathbf{q_c}\,]$$

This is possible only if,

$$
\begin{aligned}
\mathbf{q_{mul}} &= \mathbf{q} \otimes \mathbf{q_c} \\
&= q_4 q_{4c} - \mathbf{q_{vec}} \cdot \mathbf{q_{c,vec}} + q_{4c}\mathbf{q_{vec}} + q_4 \mathbf{q_{c,vec}} - (\mathbf{q_{vec}} \times \mathbf{q_{c,vec}}) \\
&= \begin{bmatrix} q_{4c}\mathbf{q_{vec}} + q_4\mathbf{q_{c,vec}} - (\mathbf{q_{vec}} \times \mathbf{q_{c,vec}}) \\ q_4 q_{4c} - \mathbf{q_{vec}} \cdot \mathbf{q_{c,vec}} \end{bmatrix}
\end{aligned}
\qquad \text{(B.25)}
$$
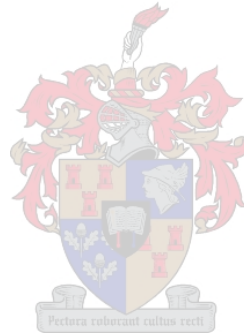
APPENDIX C

10th Order IGRF model

The contents of this appendix are based on the contents in Appendix A of Steyn (1995) which discusses an 8th order IGRF model. The mathematical theory is discussed in Wertz (1986) as well. For regions on the surface of the Earth and above which are free from external magnetic effects, the main magnetic field due to Earth is the negative gradient of a scalar potential and is represented as,

$$\mathbf{B} = -\nabla V \tag{C.1}$$

The scalar potential V is represented as,

$$V(r,\theta,\phi) = a\sum_{n=1}^{k}\left(\frac{a}{r}\right)^{n+1}\sum_{m=0}^{n}(g_n^m\cos m\phi + h_n^m\sin m\phi)P_n^m(\theta) \tag{C.2}$$

where,

a = equatorial radius of Earth (6371.2 km)

g and h = gaussian coefficients

P = legendre functions (Schmidt semi-normalised)

r = geocentric distance

θ = co-elevation (south positive)

ϕ = East longitude from Greenwhich

The Legendre functions are solved recursively to reduce the computation time required for the model which includes converting the Legendre functions from Schmidt to Gauss normalisation. This can be done by using the relation,

$$P^{n,m} = S_{n,m}P_n^m \tag{C.3}$$

However since the Legendre functions have trigonometric functions associated (will be shown subsequently), it is more suitable to associate the normalisation factor with the Gaussian coefficients. This is represented as (refer Table C.1),

$$g^{n,m} = S_{n,m}\, g_n^m \quad \& \quad h^{n,m} = S_{n,n}\, h_n^m \tag{C.4}$$

The normalisation factor $S_{n,m}$ is calculated using mathematical induction in the following manner;

$$S_{0,0} = 1$$

$$S_{n,0} = S_{n-1,0}\left[\frac{2n-1}{n}\right] \qquad\qquad n \geq 1 \qquad\qquad \text{(C.5)}$$

$$S_{n,m} = S_{n,m-1}\sqrt{\frac{(n-m+1)(\delta_m^1 + 1)}{n+m}} \qquad m \geq 1$$

The Gauss normalised Legendre functions are calculated recursively by using the relations,

$$P^{0,0} = 1$$

$$P^{n,m} = \sin\theta P^{n-1,n-1} \qquad\qquad\qquad\qquad \text{(C.6)}$$

$$P^{n,m} = \cos\theta P^{n-1,m} - K^{n,m}P^{n-2,m}$$

where,

$$K^{n,m} = \frac{(n-1)^2 - m^2}{(2n-1)(2n-3)} \qquad\qquad n > 1 \qquad\qquad \text{(C.7)}$$

$$K^{n,m} = 0 \qquad\qquad\qquad\qquad\qquad n = 1$$

The presence of the gradient in Equation(C.1) will require partial derivatives of $P^{n,m}$, which is determined recursively as,

$$\frac{\partial P^{0,0}}{\partial\theta} = 0$$

$$\frac{\partial P^{n,n}}{\partial\theta} = (\sin\theta)\frac{\partial P^{n-1,n-1}}{\partial\theta} + (\cos\theta)P^{n-1,n-1} \qquad\qquad \text{(C.8)}$$

$$\frac{\partial P^{n,m}}{\partial\theta} = (\cos\theta)\frac{\partial P^{n-1,m}}{\partial\theta} - (\sin\theta)P^{n-1,m} - K^{n,m}\frac{\partial P^{n-2,m}}{\partial\theta}$$

It is also important to mention a set of trigonometric functions which are required for future calculations.

$$\cos m\phi = \cos((m-1)\phi)\cos\phi - \sin((m-1)\phi)\sin\phi$$
$$\sin m\phi = \sin((m-1)\phi)\cos\phi + \cos((m-1)\phi)\sin\phi \qquad\qquad \text{(C.9)}$$

By using the Gauss normalised coefficients (Equation(C.4)) and the partial derivative functions (Equation(C.8)) the components of the IGRF vector in the local tangent coordinates are determined to be,

$$B_r = \frac{-\partial V}{\partial r} = \sum_{n=1}^{k} \left(\frac{a}{r}\right)^{n+2} (n+1) \sum_{m=0}^{n} (g^{n,m} \cos m\phi + h^{n,m} \sin m\phi) P^{n,m}(\theta)$$

$$B_\theta = \frac{-1}{r} \frac{\partial V}{\partial \theta} = -\sum_{n=1}^{k} \left(\frac{a}{r}\right)^{n+2} \sum_{m=0}^{n} (g^{n,m} \cos m\phi + h^{n,m} \sin m\phi) \frac{\partial P^{n,m}(\theta)}{\partial \theta} \qquad \text{(C.10)}$$

$$B_\phi = \frac{-1}{r \sin \theta} \frac{\partial V}{\partial \phi} = \frac{-1}{\sin \theta} \sum_{n=1}^{k} \left(\frac{a}{r}\right)^{n+2} \sum_{m=0}^{n} m(-g^{n,m} \sin m\phi + h^{n,m} \cos m\phi) P^{n,m}(\theta)$$

where,

B_r = radial component of field (Outward positive)

B_θ = co-elevation component of field (South positive)

B_ϕ = azimuthal component of field (East positive)

The IGRF field vector in the local tangent coordinates is then converted to the Geocentric Inertial coordinates in the following manner (Engelbrecht 1999);

$$\mathbf{B_{VEC}^I} = \begin{bmatrix} B_{ix} \\ B_{iy} \\ B_{iz} \end{bmatrix} = \begin{bmatrix} \cos\delta\cos\Omega & \sin\delta\cos\Omega & -\sin\Omega \\ \cos\delta\sin\Omega & \sin\delta\sin\Omega & -\cos\Omega \\ \sin\delta & -\cos\delta & 0 \end{bmatrix} \begin{bmatrix} B_r \\ B_\theta \\ B_\phi \end{bmatrix} \qquad \text{(C.11)}$$

where,

$[B_{ix} \ B_{iy} \ B_{iz}]^T$ = geomagnetic field vector in Inertial coordinates

δ = declination angle

Ω = right ascension angle

The declination angle δ and the RAAN angle Ω (Section 7.1.1) are calculated from the co-elevation angle, θ, and the East longitude from Greenwhich, ϕ, respectively.

$$\delta = 90° - \theta$$
$$\Omega = \phi + \Omega_G \qquad \text{(C.12)}$$

where,

Ω_G = RAAN of Greenwhich meridian

Once this has been done the next step is to convert the geomagnetic field vector from the inertial coordinates to the orbit coordinates using the transformation matrix [**T**] (Equation (A.8)) which is denoted in the vector form as,

$$\mathbf{B^O_{VEC}} = [\mathbf{T}]\,\mathbf{B^I_{VEC}} \tag{C.13}$$

where,

$$\mathbf{B^O_{VEC}} = [B_{ox} \quad B_{oy} \quad B_{oz}]^T = \text{geomagnetic field vector in orbit coordinates}$$

Finally the geomagnetic field vector in the orbit coordinates are converted into the body coordinates using the DCM matrix (Equation (2.4)). The vector representation is,

$$\mathbf{B^B_{VEC}} = [\mathbf{A(q)}]\,\mathbf{B^O_{VEC}} \tag{C.14}$$

where,

$$\mathbf{B^B_{VEC}} = [B_Z \quad B_Y \quad B_Z]^T = \text{geomagnetic field vector in body coordinates}$$

N.B: The geomagnetic field vector (**B**) discussed on Page 44 is an alternative notation used to represent $\mathbf{B^B_{VEC}}$.

Table C.1 10th order IGRF Gaussian coefficients for the EPOCH 2005-2010

| N	m	g (nT)	h (nT)	dg/dt (nT/yr)	dh/dt (nT/yr)	N	m	g (nT)	h (nT)	dg/dt (nT/yr)	dh/dt (nT/yr)
1	0	-29557	----	8.8	----	7	6	13	-64	-0.5	-0.3
1	1	-1672	5080	10.8	-21.3	7	7	1.0	-3.0	0.9	0.3
2	0	-3511	----	-15.0	----	8	0	1247	----	-0.2	----
2	1	5278	-4495	-6.9	-23.3	8	1	516	751	0.2	-0.2
2	2	1435	-448	-1.0	-14.0	8	2	-639	-1178	-0.2	0.2
3	0	3340	----	-0.3	----	8	3	-282	402	0.2	0.2
3	1	-7059	-614	-3.1	5.4	8	4	-481	-529	-0.2	0.4
3	2	2414	522	-0.9	-6.5	8	5	148	239	0.2	0.2
3	3	533	-415	-6.8	-2.0	8	6	65	53	0.5	-0.3
4	0	4024	----	-2.5	----	8	7	-29	-32	-0.7	0.5
4	1	4417	1557	2.8	2.0	8	8	-3.0	-0.1	0.5	0.4
4	2	828	-884	-7.1	1.8	9	0	532	----	0.0	----
4	3	-794	305	5.9	5.6	9	1	1249	-2561	0.0	0.0
4	4	74	-225	-3.2	0.0	9	2	391	1402	0.0	0.0
5	0	-1792	----	-2.6	----	9	3	-581	1054	0.0	0.0
5	1	3603	434	0.4	0.1	9	4	282	-378	0.0	0.0
5	2	1605	1382	-3.0	1.8	9	5	-364	-273	0.0	0.0
5	3	-643	-579	-1.2	2.0	9	6	-23	141	0.0	0.0
5	4	-373	-43	0.2	4.5	9	7	66	22	0.0	0.0
5	5	-10	73	-0.6	-1.0	9	8	-17	-20	0.0	0.0
6	0	1053	----	-0.8	----	9	9	-5.6	3.6	0.0	0.0
6	1	1316	-382	0.2	-0.4	10	0	-397	----	0.0	----
6	2	1145	817	-0.2	-1.9	10	1	-1533	584	0.0	0.0
6	3	-1505	635	2.1	-0.4	10	2	337	42	0.0	0.0
6	4	-82	-346	-2.1	-0.4	10	3	-413	727	0.0	0.0
6	5	34	0.0	-0.4	-0.2	10	4	-12	549	0.0	0.0
6	6	-58	34	1.3	0.9	10	5	222	-481	0.0	0.0
7	0	2140	----	-0.4	----	10	6	12	-41	0.0	0.0
7	1	-2639	-2178	0.0	0.8	10	7	42	-68	0.0	0.0
7	2	-41	-652	-0.2	0.4	10	8	32	-7.0	0.0	0.0
7	3	791	141	1.1	0.1	10	9	-0.3	-6.1	0.0	0.0
7	4	152	314	0.6	0.2	10	10	-1.3	-4.7	0.0	0.0
7	5	58	67	0.4	-0.9	---	---	----	----	----	----

APPENDIX D

Two Line Element Set

The two line element (TLE) set is a format which describes the Keplerian orbital elements of the satellite along with certain other parameters. The TLE is generated by the by NORAD using doppler techniques. NORAD updates the TLE's periodically.

The general representation of the TLE is as shown.

```
AAAAAAAAAAAAAAAAAAAAAAAA
1 NNNNNU NNNNNAAA NNNNN.NNNNNNNN +.NNNNNNNNN +NNNNN-N +NNNNN-N N NNNNN
2 NNNNN NNN.NNNN NNN.NNNN NNNNNNN NNN.NNNN NNN.NNNN NN.NNNNNNNNNNNNNN
```

A: Denotes an alphabet

N: Denotes a number

U: Indicates unclassified

+,.,-: Denotes a plus, decimal and minus sign respectively

Line 0 is a twenty four character name which is the standard followed for the NORAD satellite catalogue. Lines 1 and 2 are the standard two line orbital element set.
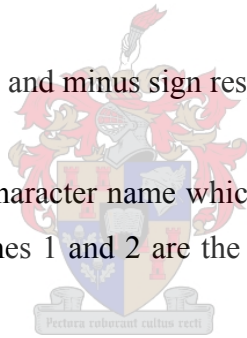
TLE Description

Discussing the TLE set with the help of an example is the easiest way to gain insight about the format.

```
ASTRA 1B
1 21139U 91015A   05188.08874751  .00000000  00000-0  00000-0 0  2733
2 21139   0.0228 270.5862 0003261 157.3962 268.5399  1.00273342 40913
```

The TLE of Astra 1B which is used in the study is shown here. It can be seen that each line contains 69 columns including the spaces in between adjacent numbers. A description of each column in each row is done in Table D.1 and Table D.2 with Astra 1B as the example.

Table D.1 Description of the first line in the TLE

Field	Column	Description	Value for Astra 1B
1.1	01	Line number	1
1.2	03-07	Satellite number	21139
1.3	08	Classification	U
1.4	10-11	International Designator (Last two digits of launch year)	91
1.5	12-14	International Designator (Launch number of the year)	015
1.6	15-17	International Designator (Piece of Launch)	A
1.7	19-20	Epoch Year (Last two digits of the year)	05
1.8	21-32	Epoch (Day and fractional part of the year)	188.08874751
1.9	34-43	First time derivative of mean motion/2	.00000000
1.10	45-52	Second time derivative of mean motion/6 (decimal point assumed)	00000-0
1.11	54-61	BStar drag term (decimal point assumed)	00000-0
1.12	63	Ephemeris type	0
1.13	65-68	Element number	273
1.14	69	Checksum (Modulo 10) (Letters, blanks, periods, plus signs = 0; minus signs = 1)	3

Fields 1.1 to 1.8 are self-explanatory. Fields 1.9 and 1.10 describes how the mean motion changes with respect to time. As expected for a GEO satellite these values are zero for Astra 1B. These terms are not important in the sense that they are not used in the orbit propagation model. The field 1.11 indicates the drag term involved for the satellite which is zero as expected. The representation in fields 1.10 and 1.11 requires some explanation. For example, the value -12345-6 corresponds to -0.12345×10^{-6}. Each of these two fields can be blank, corresponding to a value of zero. Field 1.12 is an internal parameter used by NORAD which is displayed as zero for public use. Field 1.13 denotes the number of element sets that have been generated so far for the body in consideration (in this case Astra 1B). Field 1.14 will be discussed later on.

Table D.2 Description of the second line in the TLE

Field	Column	Description	Value for Astra 1B
2.1	01	Line number	2
2.2	03-07	Satellite number	21139
2.3	09-16	Inclination	0.0228
2.4	18-25	RAAN	270.5862
2.5	27-33	Eccentricity (decimal point assumed)	0003261
2.6	35-42	Argument of Perigee	157.3962
2.7	44-51	Mean anomaly	268.5399
2.8	53-63	Mean motion	1.00273342
2.9	64-68	Revolution number at epoch	4091
2.10	69	Checksum (Modulo 10)	3

Fields 2.3 to 2.7 except for 2.5 is expressed in degrees. Field 2.8, which is the mean motion of the satellite, is expressed in revolution/day. Field 2.9 gives the number of revolutions done by the satellite with respect to the ascending node, since launch. Field 2.10 and 1.14 are the same. It is a robust error checking method where all the numbers are added along with minus signs which are assigned the value 1. The last digit of the sum happens to be the checksum.

The fields that are important and get used in the orbit propagator model are Fields 2.3 to 2.8 along with Fields 1.4 and 1.5. The rest of the fields are just academic from a propagation point of view. A more detailed description of the TLE set can be found on the webpage, http://celestrak.com/columns/v04n03/index.asp#FAQ01.

APPENDIX E

Moment of Inertia Calculations

Moment of inertia is an important parameter in a spacecraft. Moment of inertia's varies with time due to propellant consumption mainly. Here we will calculate inertias before and after the solar panels have been deployed.

E.1 Inertias with Non-Deployed Appendages

The mass of the satellite in orbit at the BOL is as mentioned in section 2.1.This is the mass inclusive of the appendages (solar panels and antenna, both non-deployed), hardware and propellant. The satellite in this state will just be a box as shown.
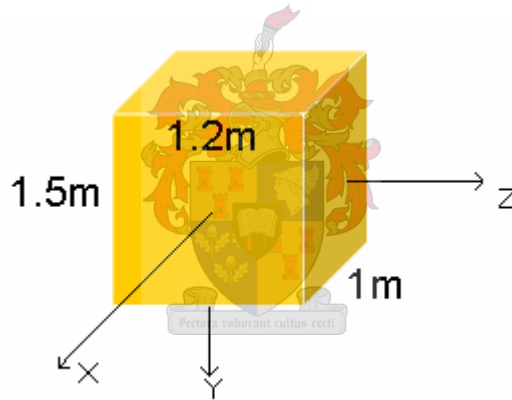

Fig E.1 Satellite with non-deployed appendages

$$I_{Xo} = \frac{m}{12}[y^2 + z^2] = \frac{500}{12}[1.5^2 + 1.2^2] = 153\,kgm^2 \qquad (E.1)$$

$$I_{Yo} = \frac{m}{12}[z^2 + x^2] = \frac{500}{12}[1.2^2 + 1.0^2] = 101\,kgm^2 \qquad (E.2)$$

$$I_{Zo} = \frac{m}{12}[x^2 + y^2] = \frac{500}{12}[1.0^2 + 1.5^2] = 135\,kgm^2 \qquad (E.3)$$

where *m* is the mass of the satellite.

E.2 Inertias with Deployed Appendages

Once the satellite has acquired references like the Sun and Earth, solar panels and antenna is deployed. The moment of inertia calculated along each axis is used in the control algorithms. The moment of inertia contributions of the satellite antenna can be ignored because of its low mass contributions. The configuration of the satellite is as shown below. The individual solar panel mass would be around 10kg.
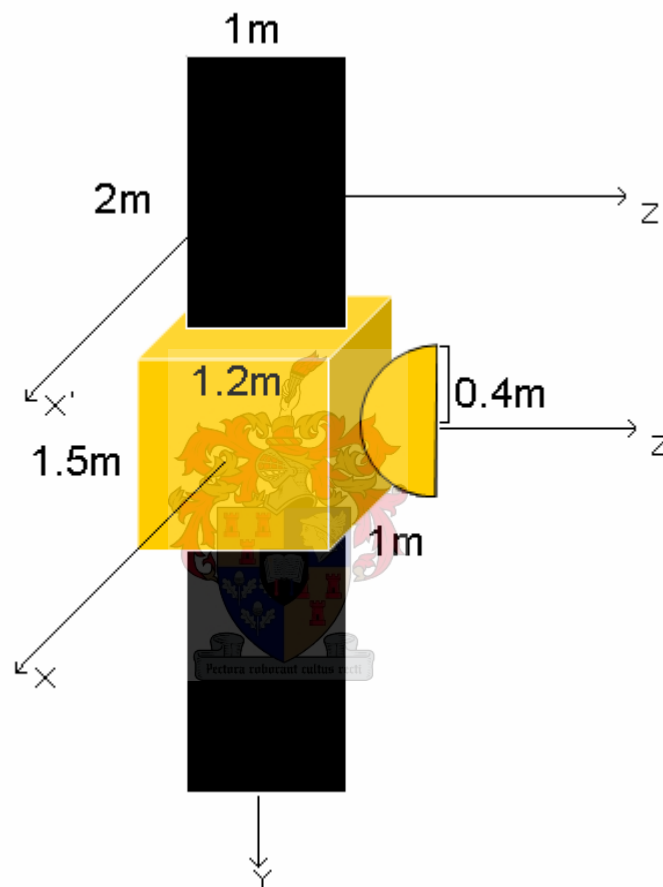

Fig E.2 Satellite with Deployed Appendages

       The parallel axis theorem can be used for calculating the moment of inertia along the X and Z axes.

$$I_{x'} = I_{z'} = \frac{m_p}{12}(panel\ length)^2 \qquad\qquad (E.4)$$

and,

$$I_{Y'} = \frac{m_p}{12}(panel\ width)^2 \qquad\qquad (E.5)$$

where m_p = mass of solar panels = 10kg

    $I_{x'} = I_{z'}$ is calculated to be 3.33 kgm^2 whereas $I_{Y'}$ is 0.833 kgm^2.

With these values the inertia of satellite due to the panels can calculated.

$$I_{XX'} = 2(I_{x'} + m_p d^2) \qquad\qquad (E.6)$$

$$I_{ZZ'} = 2(I_{z'} + m_p d^2) \qquad\qquad (E.7)$$

$$I_{YY'} = 2(I_{Y'}) \qquad\qquad (E.8)$$

where d = distance between centre of panel to centre of satellite = 2.75m

    $I_{XX'} = I_{ZZ'} = 160\,kgm^2$ whereas $I_{YY'}$ is $1.66\,kgm^2$

Now we are able to calculate the total moment of inertia's along each axis.

$$I_{XX} = I_{Xo} + I_{XX'} = 313\,kgm^2$$
$$I_{ZZ} = I_{Zo} + I_{ZZ'} = 295\,kgm^2 \qquad\qquad (E.9)$$
$$I_{YY} = I_{Yo} + I_{YY'} = 102.66\,kgm^2$$

APPENDIX F

Sensors
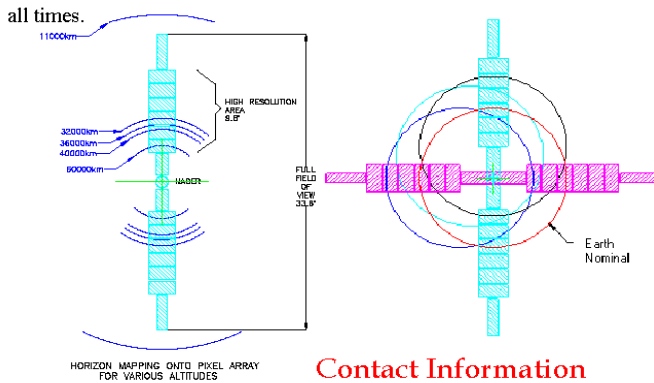
F.1 Earth Sensor

MiDES-G

SERVO CORPORATION OF AMERICA

Description:

The MiDES Earth sensor is designed to provide horizon position information in two mutually orthogonal axes (X and Y) which form a plane that is normal to nadir. This is accomplished utilizing one assembly that contains two optical heads that view the Earth and share common electronic signal processing circuitry and a common mechanical chopper.

The performance of the MiDES G is achieved through the use of a multi pixel detector array of 16 discrete pixels in each of the two hybrid detector assemblies. The radiant contrast needed to produce a voltage output from the pyroelectric detectors is achieved through the use of a chopper mechanism that causes the radiant energy falling on the detector to alternate between the energy emitted from the scene and from the chopper. The chopper temperature is much higher than the scene (space and Earth) thus producing a large output voltage at all times.

HORIZON MAPPING ONTO PIXEL ARRAY
FOR VARIOUS ALTITUDES

Specifications

- Accuracy: 0.025° (3σ)
- Supply Voltage: 28 (+7 -6) VDC
- Supply Power: <4 W
- Output: Digital (RS 422)
- Detector: Proprietary LTO
- Optical Pass Band: 14.6-15.8μ
- Operational Range: Circular 33 °

Environmental

- Random Vibration: 28 Grms
- Shock: 517Gs @ 10Khz
- Temperature: -40 to + 60°C
- Life: 15 years at GEO
- EMC: Mil-Std 462

Physical

- Mass: 1.5 KG
- Dimensions: 5.25 x 5.25 x 5.07 in.
- Mounting Surface: Flat (flange)

Electrical

- Hybridized Detector Assembly
- 16 bit rad hard microprocessor
- Opto-isolated digital interface
- Built in test
- Outputs actual direct angle data

Contact Information

Servo Corporation of America
123 Frost Street, Westbury, NY 11590, USA
Tel: 516 938 9700 Ext. 228   Email: dickb@servo.com
FAX: 516 938 9644 URL: www.servo.com

Servo Data Sheet M001-400

134

F.2 Fine Sun Sensor

DSS2 DIGITAL SUN SENSOR

The sensor can be used in a three-axis stabilized satellite to measure the attitude angle of the satellite with respect to the sun. There are various structures of the product available for different user requirements. The independent optical heads also can be provided for user's own assembly.

The principle of the sensor is that both coarse code and fine code are used in the sensor and that the coarse code is synchronized by fine code. The sensor is characteristic of large field of view, high accuracy and low power dissipation.

Up to now, this kind of products has been successfully used on flying mission for many times. All result indicates that such products provide high accuracy, reliability, and economy.

CHARACTERISTICS

FOV		+/−64 degree x +/−60 degree
Accuracy	(0~+/−32 degree)	0.05 degree
	(+/−32~+/−64 degree)	0.1 degree
Resolution		28″
Optic head mass		350g
Optic head size		86x50x30 mm
Operating temperature		−20 C ～ +50 C
Output		16bit digital
Power dissipation		0.5W
Life time (in GEO)		15 years

Astro Research Corporation
Yokohama Business Park East 12F
134 Godo-cho, Hodogaya
Yokohama, Kanagawa
JAPAN

For further information please contact:
sales@astro-r.co.jp
TEL: +81-(0)45-348-7431
FAX: +81-(0)45-348-7524
URL: http://www.astro-r.co.jp